USGS
science for a changing world

هيئة المساحة الجيولوجية السعودية
SAUDI GEOLOGICAL SURVEY

Mantle Origin and Crustal Differentiation of Basalts and Hawaiites of Northern Harrat Rahat, Kingdom of Saudi Arabia

Chapter I of

Active Volcanism on the Arabian Shield—Geology, Volcanology, and Geophysics of Northern Harrat Rahat and Vicinity, Kingdom of Saudi Arabia

U.S. Geological Survey Professional Paper 1862
Saudi Geological Survey Special Report SGS–SP–2021–1

U.S. Department of the Interior
U.S. Geological Survey

Cover. View to east from northeasternmost terminus of the late Pleistocene basalt of Southern Fingers; low, dark area in middle distance is the middle Pleistocene basalt of Upper Qa Hadawda (see Downs and others [2019] for unit descriptions). In far distance is the light-colored sabkha of Qā' Ḩaḍawḍā', and hills on the skyline are Neoproterozoic rocks of the Arabian Shield. U.S. Geological Survey photograph by Thomas Sisson, February 8, 2014. Background image shows northern Harrat Rahat lava flows, maars, and lava domes. U.S. Geological Survey photograph by Andrew Calvert, January 25, 2012.

Mantle Origin and Crustal Differentiation of Basalts and Hawaiites of Northern Harrat Rahat, Kingdom of Saudi Arabia

By Thomas W. Sisson, Drew T. Downs, Andrew T. Calvert, Hannah R. Dietterich, Gail A. Mahood, Vincent J.M. Salters, Mark E. Stelten, and Jamal Shawali

Chapter I of

Active Volcanism on the Arabian Shield—Geology, Volcanology, and Geophysics of Northern Harrat Rahat and Vicinity, Kingdom of Saudi Arabia

Edited by Thomas W. Sisson, Andrew T. Calvert, and Walter D. Mooney

U.S. Geological Survey Professional Paper 1862
Saudi Geological Survey Special Report SGS–SP–2021–1

U.S. Department of the Interior
U.S. Geological Survey

U.S. Geological Survey, Reston, Virginia: 2023

For more information on the USGS—the Federal source for science about the Earth, its natural and living resources, natural hazards, and the environment—visit https://www.usgs.gov or call 1–888–ASK–USGS.

For an overview of USGS information products, including maps, imagery, and publications, visit https://store.usgs.gov.

Any use of trade, firm, or product names is for descriptive purposes only and does not imply endorsement by the U.S. Government.

Although this information product, for the most part, is in the public domain, it also may contain copyrighted materials as noted in the text. Permission to reproduce copyrighted items must be secured from the copyright owner.

Suggested citation:
Sisson, T.W., Downs, D.T., Calvert, A.T., Dietterich, H.R., Mahood, G.A., Salters, V.J.M., Stelten, M.E., and Shawali, J., 2023, Mantle origin and crustal differentiation of basalts and hawaiites of northern Harrat Rahat, Kingdom of Saudi Arabia, chap. I *of* Sisson, T.W., Calvert, A.T., and Mooney, W.D., eds., Active volcanism on the Arabian Shield—Geology, volcanology, and geophysics of northern Harrat Rahat and vicinity, Kingdom of Saudi Arabia: U.S. Geological Survey Professional Paper 1862 [also released as Saudi Geological Survey Special Report SGS–SP–2021–1], 42 p., https://doi.org/10.3133/pp1862I.

ISSN 1044-9612 (print)
ISSN 2330-7102 (online)

هيئة المساحة الجيولوجية السعودية
SAUDI GEOLOGICAL SURVEY

Ministry of Industry and Mineral Resources
BANDAR BIN IBRAHIM BIN ABDULLAH AL-KHORAYEF, Minister and SGS Chairman

Saudi Geological Survey
Abdullah bin Mufter Al-Shamrani, Chief Executive Officer

Saudi Geological Survey, Jiddah, Kingdom of Saudi Arabia: 2023

Contents

Figures

Tables

Conversion Factors

International System of Units to U.S. customary units

Multiply	By	To obtain
	Length	
millimeter (mm)	0.03937	inch (in.)
meter (m)	3.281	foot (ft)
kilometer (km)	0.6214	mile (mi)
	Area	
square meter (m^2)	10.76	square foot (ft^2)
square centimeter (cm^2)	0.1550	square inch (ft^2)
square kilometer (km^2)	0.3861	square mile (mi^2)
	Volume	
liter (L)	33.81402	ounce, fluid (fl. oz)
liter (L)	0.2642	gallon (gal)
cubic meter (m^3)	264.2	gallon (gal)
liter (L)	61.02	cubic inch (in^3)
cubic meter (m^3)	35.31	cubic foot (ft^3)

Temperature in degrees Celsius (°C) may be converted to degrees Fahrenheit (°F) as follows:

$$°F = (1.8 \times °C) + 32.$$

Abbreviations

An	anorthite component, in mole percent
CIPW norm	rock chemical compositions (recast into weight percent) of rock-forming minerals, following method of Cross, Iddings, Pirsson, and Washington
D	partition-coefficient value, defined as weight concentration of element in a mineral or mineral assemblage, divided by its weight concentration in equilibrium-coexisting melt
DM	depleted mantle
FeO_t	$FeO+0.8998Fe_2O_3$
fO_2	oxygen fugacity
GPa	gigapascal
Hy	normative hypersthene
ICP-MS	inductively coupled plasma mass spectrometry
k.y.	thousand years
Ma	mega-annum, or million years ago
Mg#	Mg number (=100×Mg/[Mg+Fe^{2+}], molar)
MORB	midocean ridge basalt
MPa	megapascal
Ne	normative nepheline
ppm	parts per million, by weight
QFM	quartz-fayalite-magnetite
Qtz	normative quartz
REE	rare earth element
SGS	Saudi Geological Survey
TAS	total alkalis-silica
USGS	U.S. Geological Survey

Active Volcanism on the Arabian Shield
Edited by T.W. Sisson, A.T. Calvert, and W.D. Mooney
U.S. Geological Survey Professional Paper 1862
Saudi Geological Survey Special Report SGS–SP–2021–1

Chapter I

Mantle Origin and Crustal Differentiation of Basalts and Hawaiites of Northern Harrat Rahat, Kingdom of Saudi Arabia

By Thomas W. Sisson,[1] Drew T. Downs,[1] Andrew T. Calvert,[1] Hannah R. Dietterich,[1] Gail A. Mahood,[2] Vincent J.M. Salters,[3] Mark E. Stelten,[1] and Jamal Shawali[4]

Abstract

Quaternary volcanic rocks of northern Harrat Rahat, Kingdom of Saudi Arabia, are chiefly alkali basalts with subordinate transitional basalts, hawaiites, mugearites, benmoreites, and trachytes. Geochemical and isotopic results indicate that crystallization-differentiation, mixing, and cumulate reassimilation within the magmatic system produced most of its compositional diversity, with only minor involvement of Neoproterozoic crust. With increasing evolution, crystal assemblages that separated from and drove basalt-to-hawaiite differentiation passed from (1) dunitic or troctolitic to (2) olivine gabbroic to (3) titanomagnetite-bearing olivine gabbroic, with typical hawaiites representing about 20 weight percent residual liquids from an estimated primary alkali basaltic parent. Crystallization-differentiation simulations for midcrustal pressures yield the closest compositional match to the basalt-hawaiite suite, and stagnation in the midcrustal area (near 20 kilometers [km] depth) may result from density trapping beneath the lower density upper continental crust. Least differentiated alkali basalts have fractionation-adjusted major-oxide compositions that are consistent with separation from the deeper parts (60–70 km) of the spinel-lherzolite stability field at pressures that are close to the local lithosphere-asthenosphere boundary (60–80 km). Mantle potential temperature estimates are strongly sensitive to modeling approach, but potential temperatures (1,345–1,390 degrees Celsius [°C]) are not discernably greater than for midocean ridge basalts (MORB; 1,350–1,410 °C) if adherence to spinel-lherzolite melting relations is required. Inversion of the trace-element concentrations of the lesser fractionated basalts indicates a depleted mantle source, similar to MORB-source estimates, but one that is enriched in Sr and includes a greater relative proportion of melting in the garnet-peridotite stability field. These geochemical and thermal relations, as well as radiogenic isotopes, point to a dominantly depleted mantle asthenospheric source for Harrat Rahat basalts, admixed with subordinate materials either from the Afar mantle plume or an enriched MORB component in the ambient asthenosphere. The lithosphere-asthenosphere boundary is shallower beneath the belt of major volcanic fields on the Arabia Plate, and restoration of rifting across the Red Sea and Gulf of Aden places the south end of this belt adjacent to the northern part of the Afar region, suggesting a once-continuous structure, possibly an arch, a weakness, or a discontinuity along the base of the lithosphere. Magma generation can be ascribed to focused upwelling and decompression melting, perhaps driven by a magmatic-feedback mechanism whereby basaltic intrusions into the deep lithosphere solidify as eclogites, causing lithospheric foundering and further asthenospheric upwelling and decompression melting in a restricted region.

Introduction

Causes are enigmatic for Neogene and Quaternary Arabia Plate volcanism. Large, basalt-dominated volcanic fields, known in Arabic as harrats, are distributed in a broadly north-northwest-trending belt that spans at least 2,000 kilometers (km) from Yemen across the Kingdom of Saudi Arabia and on into Syria (Coleman and others, 1983; Brown and others, 1989; Camp and Roobol, 1992). The proximity of the harrats to, and their rough parallelism with, the Red Sea (fig. 1) raises the possibility that intraplate extension drives magmatism by thinning the lithosphere, leading to passive decompression melting in the shallow mantle. The largest harrats, however, lie east of the Red Sea coastal escarpment and the Ḥijāz-ʿAsīr highlands, where the Arabia Plate lacks more than minor evidence for recent or ongoing extension, such as horsts, grabens, offset alluvium and wadis, or disrupted sabkhas (playas). The amounts of plate extension, therefore, appear

[1]U.S. Geological Survey.

[2]Stanford University.

[3]Florida State University.

[4]Saudi Geological Survey.

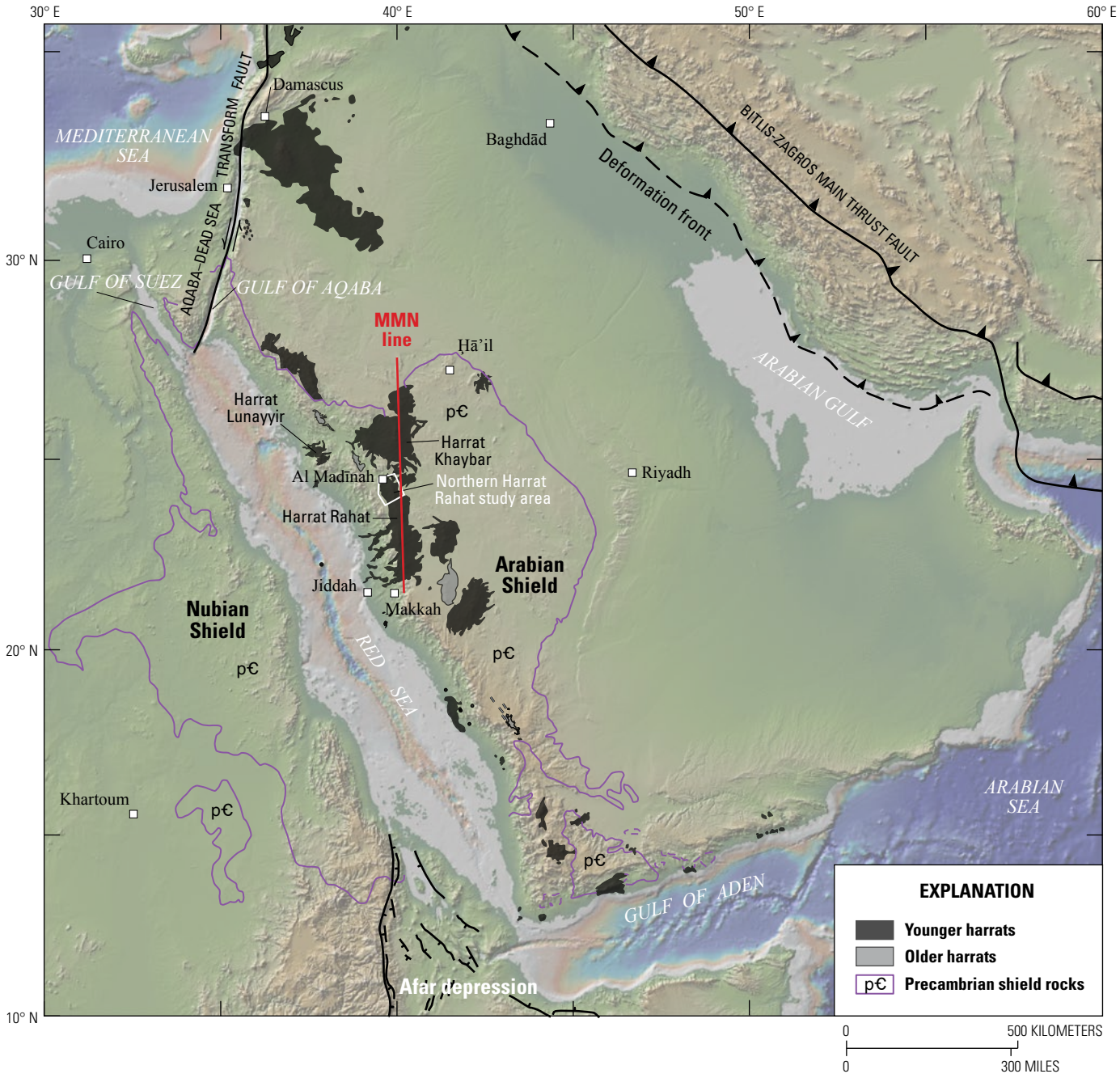

Figure 1. Colored shaded-relief map of Arabian Peninsula and vicinity, showing tectonic setting of Harrat Rahat and other subaerial volcanic fields that chiefly are younger than 13 mega-annums (Ma) (dark-gray shading), as well as older harrats (light-gray shading); omitted are Oligocene basaltic traps, Neogene to Quaternary volcanic rocks of Afar depression, and all submarine volcanic rocks. Purple lines show approximate limits of Precambrian exposures of Arabian and Nubian Shields. Thick black lines show faults: solid where location is accurate; dashed where location is approximate or concealed; paired black arrows show relative movement on strike-slip faults; sawteeth are on upper plate of thrust faults; tick marks are on downthrown block of normal faults. Red line shows Makkah-Madīnah-Nafud (MMN) volcanic line, which traces generally high-standing axis of largest active volcanic fields. Extents of Arabian and Nubian Shield rocks, plate-bounding structures, and faults modified from U.S. Geological Survey–Arabian American Oil Company (1963), Coleman and others (1983), Bosworth and others (2005), and Stern and Johnson (2010). Shaded-relief base map and shorelines generated with GeoMapApp (www.geomapapp.org) using global multiresolution topography and bathymetry (Ryan and others, 2009).

negligible in the region where subaerial volcanism is most abundant (Camp and Roobol, 1992). Magmatism might also be driven by a mantle plume undergoing decompression melting, possibly also encountering, heating, and partly melting fertile domains in the ambient upper mantle. Nevertheless, the major recognized plume of the region is centered beneath the Afar depression, and it is unclear why plume material would selectively fuel a belt of harrats on the Arabia Plate, some of which are located as far as 2,500 km from the plume center, but would not cause similar young volcanism on the Nubian Shield and in the northwestern Indian Ocean or would not supply abundant plume magmas or components to the Red Sea spreading system. Chemical and isotopic compositions of harrat volcanic rocks can be used to distinguish between mantle sources and melting processes and thereby improve understanding of their tectono-magmatic origins.

Few basalts from the Arabian harrats have sufficiently high MgO concentrations, Mg numbers (Mg# = 100×Mg/[Mg+Fe^{2+}], molar), and other chemical characteristics to be considered primary magmas that ascended directly from ultramafic upper mantle sources (Coleman and others, 1983). Instead, nearly all are somewhat evolved and are members of diverse, generally alkalic volcanic suites that in some harrats range to trachyte or peralkaline rhyolite (Camp and others, 1991). Crystallization-differentiation, partial remelting of recently antecedent mafic intrusions, and assimilation of old continental crust are mechanisms that may lead to this magmatic diversity. Of practical interest for monitoring volcanic unrest and for anticipating and mitigating potential hazards is to understand where the magmas lodge and differentiate in the crust or upper mantle, if there are preferential storage regions at all. The chemical compositions and phenocryst mineralogy of variably differentiated harrat basalts and of associated more evolved rocks can be interpreted to estimate the depths and processes whereby the mantle melts to produce basalts, as well as the depths of subsequent fractional crystallization and (or) melting that produce more evolved magmas, thereby providing information to improve the configurations of monitoring networks and the interpretations of monitoring signals.

To these ends, this report presents and interprets the geochemistry and petrology of basalts and hawaiites of northern Harrat Rahat, Kingdom of Saudi Arabia (fig. 2), adjacent to the city of Al Madīnah al Munawwarah (hereafter, Al Madīnah). This report is a product of the joint project by the U.S. Geological Survey (USGS) and the Saudi Geological Survey (SGS) to improve the understanding of, and to mitigate against, potential volcanic and seismic hazards to Al Madīnah by investigating volcanic geology, geochemistry, and geophysics. The whole of Harrat Rahat spans about 310 km from Al Madīnah in the north nearly to Makkah al Mukarramah in the south and is generally about 50 to 70 km wide, although some early, large-volume basalt flows descended westward as much as about 100 km to the Red Sea coastal plain. Overall, volcanic rocks of Harrat Rahat cover about 19,830 square kilometers (km^2) (Camp and Roobol, 1991b). The area studied in the USGS–SGS project encompasses the greatest concentration of young-appearing lava flows, cinder cones, lava domes, and tuffs of Harrat Rahat, and it extends from Al Madīnah south about 70 km to near latitude 24° N. where an oil and gas pipeline crosses a topographic low on the crest of the harrat. The volcanic field is about 50 km wide across the study area, so the project investigated roughly 3,340 km^2 of Quaternary volcanic deposits, equal to about 20 percent of the entire volcanic field. Results from other project components are summarized as chapters in this volume and in related publications in the scientific literature. This report builds on prior petrologic studies of Harrat Rahat by Moufti (1985), Camp and others (1987), Camp and Roobol (1989, 1992), Moufti and others (2012), and Murcia and others (2016), although interpretations and conclusions presented herein differ in some respects from those prior works.

This report relies mainly on X-ray fluorescence and inductively coupled plasma mass-spectrometric chemical analyses of Quaternary volcanic rocks of the study area (Downs, 2019) collected and analyzed in support of geologic mapping (Downs and others, 2019; Robinson and Downs, 2023) and the reconstruction of eruptive history (Downs and others, 2018, 2023; Stelten and others, 2018, 2020, 2023). Reliable eruption ages from greater Harrat Rahat are documented to be as old as 8.7 million years (Ma), and volcanism is estimated to have commenced perhaps around 10 Ma (Camp and Roobol, 1991b); however, geologic mapping and geochronology in the USGS–SGS study area did not reveal any exposed volcanic rocks from Harrat Rahat proper that are older than 1.2 Ma, and most of the lava flows, tuffs, and domes exposed on the surface near Al Madīnah erupted in the last 325 thousand years (k.y.) (Stelten and others, 2020, 2023). Thus, the geochemistry summarized and interpreted in this report is almost wholly informative of the middle to late Pleistocene and Holocene conditions and processes and not of the inception or long-term development of the magmatic system. This report also depends on high-precision radiogenic-isotope determinations for representative members of the volcanic suite provided by Salters and others (2023), as well as on a reconnaissance Sr-, Nd-, and Pb-isotopic dataset reported in Moufti and others (2012). Although volcanic rocks of northern Harrat Rahat range from alkali basalts to trachytes, this report concentrates on the basalts and hawaiites, their differentiation, and their mantle sources and melting processes. Detailed interpretations of the origins of the intermediate and evolved members of the suite (that is, mugearites, benmoreites, and trachytes) were not part of this study and are not presented in this volume.

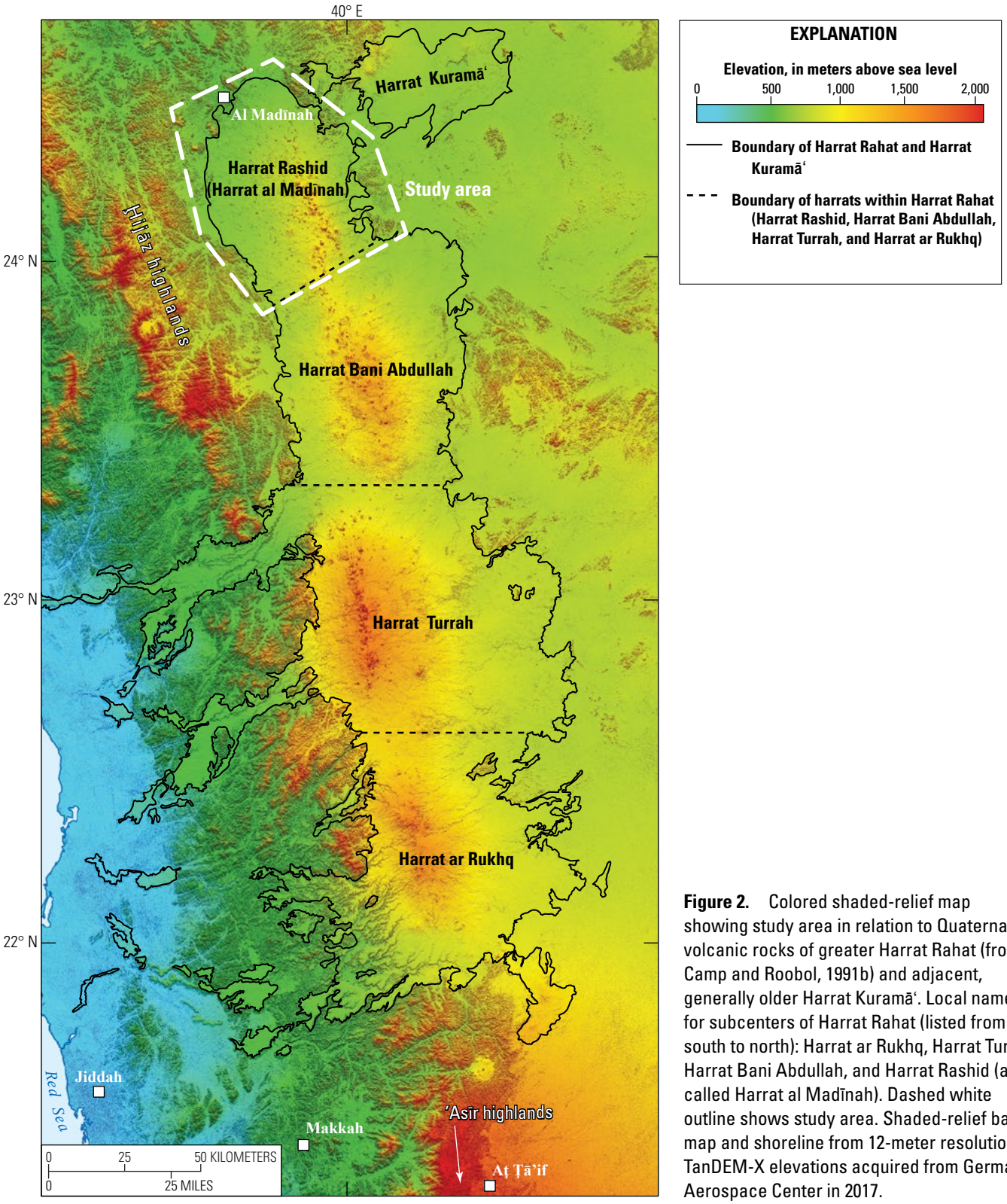

Figure 2. Colored shaded-relief map showing study area in relation to Quaternary volcanic rocks of greater Harrat Rahat (from Camp and Roobol, 1991b) and adjacent, generally older Harrat Kuramā‘. Local names for subcenters of Harrat Rahat (listed from south to north): Harrat ar Rukhq, Harrat Turrah, Harrat Bani Abdullah, and Harrat Rashid (also called Harrat al Madīnah). Dashed white outline shows study area. Shaded-relief base map and shoreline from 12-meter resolution TanDEM-X elevations acquired from German Aerospace Center in 2017.

Volcanic Suite of Northern Harrat Rahat

Overview of Volcanic Products and Nomenclature

Basaltic lava flows and their vent complexes dominate northern Harrat Rahat, making up at least 75 percent of the volume of products erupted over the last 325 k.y. The basaltic rocks are accompanied by subordinate hawaiites (lava flows), mugearites (lava flows), benmoreites (lava domes, flows, and pyroclastic deposits), and trachytes (lava domes and pyroclastic deposits) that are exposed in subequal amounts (Downs and others, 2019; Stelten and others, 2020, 2023; Robinson and Downs, 2023). Basaltic lava flows constitute an even greater proportion (about 90 percent) of the volume of the entire 310-km-long Harrat Rahat volcanic field (Camp and Roobol, 1991b). Nearly all analyzed basalts from northern Harrat Rahat have small amounts (as much as 7 weight percent) of nepheline (Ne) in their CIPW norms (Washington, 1917), as calculated with ferric and ferrous iron appropriate for their 1-bar liquidus temperatures at oxygen fugacity (fO_2) of the quartz-fayalite-magnetite (QFM) buffer (Kress and Carmichael, 1991; Ghiorso and Sack, 1995). Accordingly, they are classified as alkalic. Fewer than 5 percent of analyzed northern Harrat Rahat basalts have normative hypersthene (Hy), but only in trace amounts (<2 weight percent). These weakly Hy-normative basalts are mineralogically indistinguishable from the Ne-normative basalts, including lacking modal hypersthene or pigeonite, so such rocks are appropriately termed olivine transitional basalts (Camp and Roobol, 1991b), or herein, simply transitional basalts. Their traces of normative Hy are due to the CIPW norm's inability to account for the small hypersthene component of augite, as well as to its assignment of all Ti to ilmenite, thereby reducing Fe available to calculate olivine versus hypersthene, even though augite hosts much of the Ti in the basalts. The total alkalis-silica (TAS) division of Macdonald and Katsura (1964) accurately discriminates Ne- from Hy-normative northern Harrat Rahat basalts as alkaline and subalkaline, respectively (fig. 3), whereas the revised

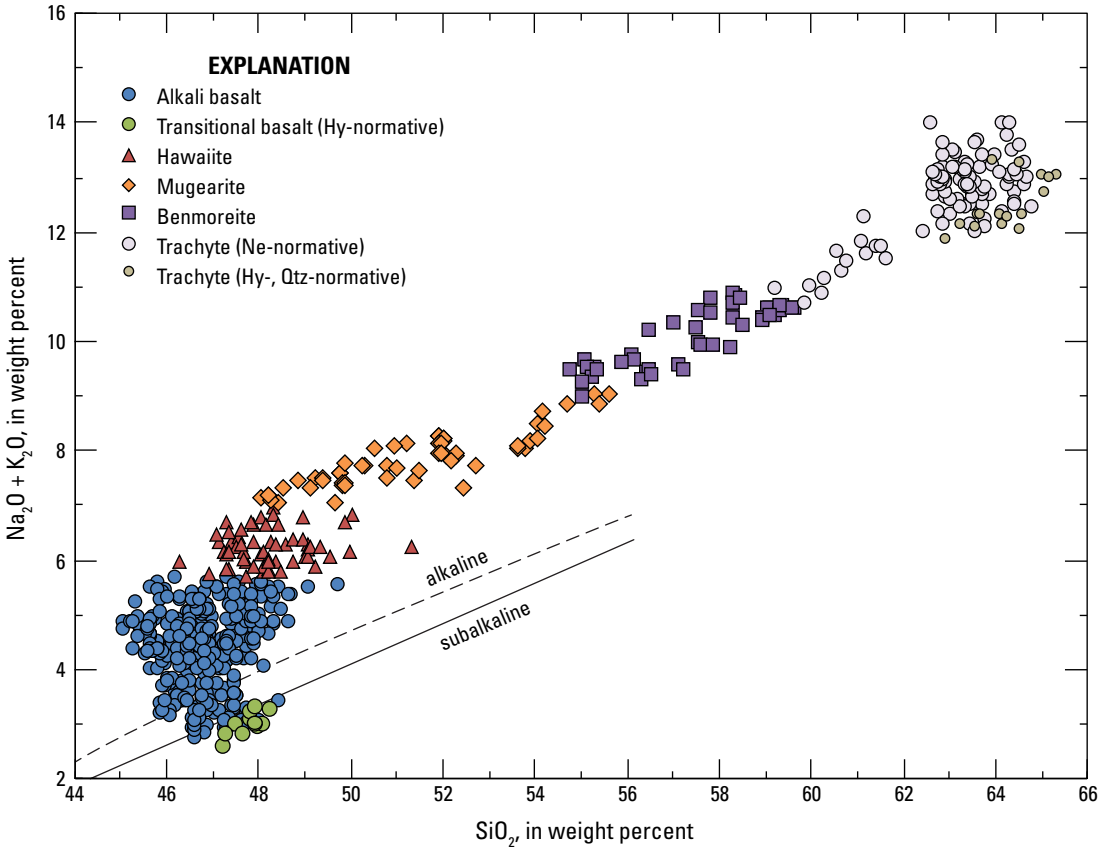

Figure 3. Plot of total alkali (Na_2O+K_2O) versus silica (SiO_2) concentrations of Quaternary volcanic rocks of northern Harrat Rahat. Rocks are distinguished by rock type (Cox and others, 1979) and CIPW-normative mineral assemblage; rock compositions are from Downs (2019). Diagonal lines show alkaline-subalkaline discriminants (solid line is from Macdonald and Katsura [1964]; dashed line is from Irvine and Baragar [1971]). Abbreviations: Hy, hypersthene; Ne, nepheline; Qtz, quartz.

TAS division of Irvine and Baragar (1971) would erroneously classify many of the Ne-normative basalts as subalkaline (owing to how Irvine and Baragar [1971] estimated the Fe_2O_3 concentrations of basalts). Previous publications on Harrat Rahat that employed the Irvine and Baragar (1971) division referred to some samples and eruptive units of northern Harrat Rahat as tholeiites, tholeiitic, or subalkaline (Camp and Roobol, 1991b; Downs and others, 2018, 2019), although none examined in the present study contain low-Ca pyroxene as phenocrysts or groundmass minerals nor contain appreciable normative hypersthene if calculated with petrologically appropriate ferric- and ferrous-iron concentrations.

Nomenclature employed herein for the more evolved rocks follows the TAS fields of Cox and others (1979). Application of the more widely used but slightly different TAS schema of Le Bas and others (1986) would break out small numbers of hawaiites and mugearites as basanites without accompanying distinctions in mineralogy or geochemical association, and so it is not employed herein. The Le Bas and others (1986) schema would also classify about 20 percent of the more alkali-rich basalts as hawaiites. Calculated again as liquids at QFM, nearly all (97–98 percent) of analyzed hawaiites, mugearites, and benmoreites from northern Harrat Rahat are Ne-normative. Trachytes are more diverse, with about 85 percent being Ne-normative, 10 percent having minor normative Hy, and 5 percent having normative quartz (Qtz) and Hy (fig. 3).

Secondary minerals that partly fill pore spaces are unavoidable in harrat volcanic rocks and potentially influence analyzed chemical compositions. Secondary minerals consist mainly of blades and filaments of gypsum, zeolites, and calcite in vesicles and vugs; clay and silica have been identified rarely. Fragile, white secondary minerals are present in pores and vugs, even in historical eruptive products, growing by the drying of pore waters introduced by occasional heavy rains. Field sampling for Ar geochronology and geochemistry targeted dense flow interiors, thereby minimizing secondary mineral abundances. Prior to chemical analysis, nearly all samples reported in Downs (2019) were crushed to less than 1-centimeter (cm) fragments and hand-picked in the laboratory to remove obvious secondary minerals and discolorations, followed by extended sonication in warm to hot deionized water to dissolve gypsum and zeolites. Crushed rocks were not, however, acid-treated prior to chemical analysis, and so some, undoubtedly, retained minor calcite. For this report, the basalt and hawaiite analyses of Downs (2019) have been screened to include only samples that have original major-oxide totals equal to or exceeding 99.0 weight percent to exclude samples that retained appreciable secondary minerals after cleaning or that were excessively hydrated. Two basalts that have acceptable totals were also excluded owing to prominent Ce anomalies >1 (eq. 1),

$$Ce_{CN} / \sqrt{La_{CN} \times Pr_{CN}}, \quad (1)$$

where the subscript *CN* signifies the element's concentration in a sample, divided by that element's concentration in chondritic meteorites (or "chondrite normalization"). Harrat Rahat rocks that have Ce anomalies >1 have additional chemical abnormalities that together potentially result from appreciable weathering or abundant secondary minerals. Mugearite, benmoreite, and trachyte compositions from Downs (2019) are included mainly for context, and their analyses were not similarly screened for low totals.

Basalt and Hawaiite Mineral Assemblages

Basalts of northern Harrat Rahat carry subhedral to skeletal phenocrysts of olivine (typically, 1–7 volume percent), some of which include small, reddish brown, translucent grains of Cr-Al-Mg-Fe spinel. Olivine is also widespread in the groundmass as small, equant grains that lack resorption or reaction against pyroxene, consistent with the alkalic character of the suite. Most plagioclase in northern Harrat Rahat basalts lies in the groundmass as well-formed, nonresorbed narrow laths, which have compositions of $An_{76–70}$ in the minor transitional basalts and $An_{72–60}$ in the abundant alkali basalts (An = 100×Ca/[Ca+Na+K], molar, in feldspars) (Camp and Roobol, 1991b). Sparse (typically, not more than 3 percent) plagioclase phenocrysts (Camp and others, 1987; Camp and Roobol, 1991b; Downs and others, 2018, 2019) are tabular and idiomorphic; some have spongy interiors or slightly embayed surfaces indicative of resorption events, and others are pristine. Distinct from these are equant (blocky), optically unzoned plagioclase crystals that have slightly scalloped or rounded surfaces; typically present only in trace amounts, they are abundant in some basalt and hawaiite lava flows where they can attain megacrystic sizes (rarely to 5 cm), and their compositions are restricted to $An_{60±3}$ (Camp and others, 1987; Camp and Roobol, 1991b). Calcic clinopyroxene is absent as a phenocryst in northern Harrat Rahat basalts but constitutes much of their groundmass; strongly pleochroic titanaugite ophitically encases groundmass plagioclase laths in the interiors of thick lava flows, accompanied by abundant granules of groundmass titanomagnetite and small groundmass olivine grains. Narrow blades of ilmenite are also present in the groundmass of basalts, but ilmenite is never present as phenocrysts or microphenocrysts. Camp and others (1987) and Camp and Roobol (1991b) reported calcic clinopyroxene (aluminous Cr-endiopside) in variably disaggregated olivine-clinopyroxene-spinel microxenoliths, although such ultramafic microxenoliths and xenocrysts are uncommon.

Hawaiites are mineralogically similar to the basalts, having sparse phenocrysts of olivine and plagioclase, except that titanomagnetite is commonly present as microphenocrysts and is conspicuously abundant in the groundmass. Tabular plagioclase phenocrysts in many hawaiites have irregular surfaces that have pronounced narrow embayment channels

and spongy interiors, indicative of resorption; some hawaiite flows contain the aforementioned homogeneous, slightly rounded plagioclase megacrysts. Groundmass plagioclase laths in hawaiites are generally $An_{50–45}$ (Camp and Roobol, 1991b). Microxenoliths of olivine gabbro and of polygranular plagioclase are present in a few hawaiite samples, but their mineral compositions have not been investigated.

The more evolved members of the volcanic suite are not the subject of this report, but mugearites are distinguished from the more mafic lavas by the presence of sparse olivine, which is typically yellowish brown in thin section owing to higher iron concentrations, as well as by conspicuous microphenocrysts of titanomagnetite; minor augite microphenocrysts; traces of blocky apatite microphenocrysts; and ubiquitous, fine apatite grains that touch, or are included in, olivine, titanomagnetite, and augite. Mugearites commonly exhibit prominent flow banding in thin section. Mugearite lava flows are readily distinguished in the field from flows of basalt or hawaiite by their greater thicknesses and breadths, by their shorter lengths, and by the abundant hornitos and broad, arcuate ogives that decorate their flow surfaces.

Major-Oxide Abundances and Variations

The alkali basalt to trachyte suite of northern Harrat Rahat is similar chemically to alkalic volcanic centers of many intraplate extensional localities such as the Tertiary British Hebrides (Thompson and others, 1972; Beckinsale and others, 1978), the East African and Afar rift systems (Barberi and others, 1975; Baker and others, 1977; Field and others, 2013), and elsewhere on the Arabia Plate (Cox and others, 1970), as well as parts of Hawai‘i (Macdonald and Katsura, 1964) and many other oceanic islands (Bohrson and Reid, 1997). Chemical variations are readily displayed on plots of whole-rock MgO concentration versus major oxides (fig. 4) and trace elements (fig. 5). Major-oxide compositions have been normalized to 100 weight percent, after calculation of ferric and ferrous iron as appropriate for QFM fO_2 at 1-bar liquidus temperatures, following the method of Ghiorso and Sack (1995).

Except for two basalt samples that have anomalously elevated MgO concentrations of 11.4 and 12.7 weight percent, the northern Harrat Rahat volcanic suite forms a continuum of MgO concentrations from 10.7 to less than 0.1 weight percent, corresponding to Mg# from 66.3 to zero. Basalts that have the greatest MgO concentrations have SiO_2 concentrations in a narrow range of about 47 to 48 weight percent. Silica concentrations remain below 50 weight percent until MgO concentration falls below 4 weight percent (Mg# near 40), then SiO_2 concentrations increase smoothly and continuously with further decreases in MgO concentration. In detail, basalt and hawaiite analyses define a downward-pointing triangular field on the MgO versus SiO_2 plot; the minimum SiO_2 concentrations fall with decreasing MgO concentration to a low of about 45 weight percent among basalts that have MgO concentrations of about 6.5 weight percent, and then they climb with further decreases of MgO concentration into the hawaiites. In contrast, concentrations of TiO_2, total iron (as FeO_t [$FeO_t = FeO+0.8998Fe_2O_3$]), and P_2O_5 define upward-peaked arrays plotted against MgO concentrations; the apices of those triangular fields are readily interpreted as marking titanomagnetite and apatite joining the fractionating crystal assemblage. Maximum TiO_2 concentrations are more than double those of the highest MgO basalts, forming a broad peak among basalts that have MgO concentrations of 7 to 5 weight percent; TiO_2 concentrations then decline sharply and narrowly from hawaiites to trachytes. Concentrations of FeO_t increase from the most magnesian basalts to a broad peak among basalts and hawaiites that have MgO concentrations of 6.75 to 3.6 weight percent, then FeO_t concentrations decrease through mugearites, benmoreites, and trachytes. The P_2O_5 pattern is more sharply peaked, with P_2O_5 concentrations increasing as much as tenfold from the most magnesian basalts through the hawaiites to a maximum at MgO concentration of about 3.7 weight percent, corresponding to the hawaiite-to-mugearite transition, then they decline sharply and regularly with further decreases in MgO concentrations across the more evolved members of the suite.

Concentrations of K_2O and Na_2O increase smoothly and continuously with decreasing MgO concentration (fig. 4), with K_2O defining an increasingly steep, concave-up trend at lower MgO concentrations. Upward concavity of K_2O versus MgO arrays, which is long familiar from basalt-dominated suites (Jameson and Clarke, 1970; Basaltic Volcanism Study Project, 1981), results from progressively decreasing MgO concentrations in their fractionating mineral assemblages. K_2O concentrations increase slightly more than fivefold from the northern Harrat Rahat basalts with the highest MgO concentrations to the hawaiites having the lowest MgO concentrations, whereas Na_2O concentrations increase linearly and only double across the same interval, owing to plagioclase in the fractionating assemblage. Basalts with MgO concentrations greater than about 8 weight percent (Mg# >60) have slightly scattered CaO concentrations that fail to define an obvious trend with MgO concentrations, but CaO concentrations decrease continuously and regularly in rocks at lower MgO concentrations. A few samples that have outlier (high) CaO concentrations have secondary calcite, which is apparent by optical petrography and electron microscopy.

Unlike the aforementioned major oxides that plot as smooth, continuous arrays, Al_2O_3 concentrations define complex trends plotted versus MgO concentration. In basalts, Al_2O_3 concentrations increase modestly with decreasing MgO concentration to a maximum among rocks that have 6 to 7 weight percent MgO, and then they decline into the

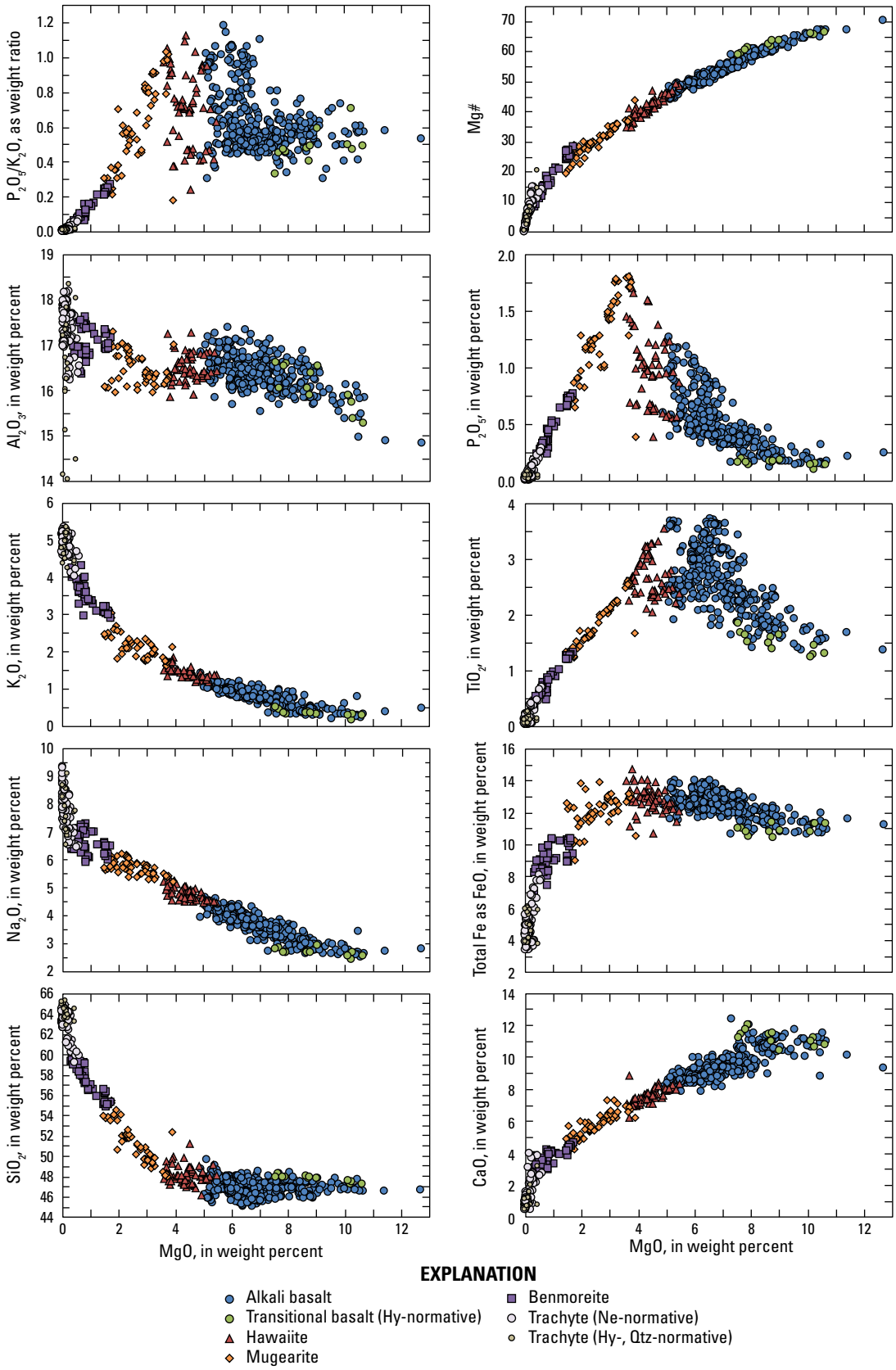

Figure 4. Plots of major oxide concentrations, concentration ratios, and Mg number (Mg#) versus MgO concentrations for Quaternary volcanic rocks of northern Harrat Rahat.

hawaiites to a local minimum near the hawaiite-to-mugearite boundary. Al_2O_3 concentrations then climb again from this local minimum through mugearites and benmoreites to trachytes. The most evolved rocks (MgO <1 weight percent) exhibit a wide range of Al_2O_3 concentrations. The highest values belong to some trachytes and benmoreites interpreted to have accumulated or assimilated alkali feldspar, as discussed subsequently. Al_2O_3 concentrations decline precipitously through the trachytes, coincident with alkali feldspar dominating their phenocryst assemblages, accompanied by minor sodic clinopyroxene and, in some cases, iron-rich olivine. Al_2O_3 concentrations reach their lowest values in the Qtz-normative and some of the Hy-normative trachytes.

Trace-Element Abundances and Variations

Concentrations of incompatible trace elements, such as La, Ba, and Zr, increase continuously and simply with decreasing MgO concentration from basalts through hawaiites into mugearites and benmoreites (fig. 5). Trachytes diverge to sharply lower concentrations of Ba and to higher concentrations of La and Zr from the overall trends versus MgO concentration. The pronounced decrease of Ba concentrations among the trachytes corresponds with their phenocryst assemblage that consists almost entirely of anorthoclase. Extensive fractionation of anorthoclase, in which Ba is compatible, results in a precipitous decline in Ba concentrations, as well as producing Eu anomaly values <1 (eq. 2),

$$Eu_{CN} / \sqrt{Sm_{CN} \times Gd_{CN}}, \quad (2)$$

where the subscript *CN* indicates normalization of that element's concentration in a sample to its concentration in chondritic meteorites; the denominator is commonly abbreviated as Eu^*_{CN} and represents the normalized Eu concentration expected by straight-line interpolation between Sm and Gd on a log-scale plot of normalized concentration versus atomic number. Some rocks at the benmoreite-to-trachyte transition have anomalously high concentrations of Ba (relative to the overall basalt-through-benmoreite trend), which, along with Eu anomaly values >1, are consistent with accumulated alkali feldspar or assimilated alkali feldspar-rich cumulates. In contrast, Eu anomalies are nearly constant and slightly greater than unity from high- to low-MgO basalts but diminish gradually from the lower MgO basalts through hawaiites and mugearites to benmoreites. The deviation among the trachytes to high concentrations of La, Zr, and other incompatible trace elements is consistent with a shift either to an MgO-poor, feldspar-rich, segregating mineral assemblage, if the trachytes formed by crystallization-differentiation, or to eutectic-like behavior, if the trachytes formed by partial remelting of antecedent alkali gabbroic intrusions. Strontium concentrations increase modestly among the basalts, attaining maximum values at 7 to 5 weight percent MgO, then they decline through the more evolved members of the suite, precipitously so once anorthoclase dominates the phenocryst assemblage. One benmoreite that has an outlier (high) Sr concentration (sample no. R15AC115) is a sample of bulk indurated tuff, and its anomalous Sr concentration is interpreted to be caused by abundant secondary calcite.

Concentration ratios of incompatible trace elements remain generally constant from basalts through hawaiites to mugearites and benmoreites, although the spread in ratio values diminishes from the most to least magnesian basalts and hawaiites (fig. 5). Near-constancy in average incompatible trace-element ratios with decreasing MgO concentration is consistent with crystallization-differentiation as a dominant process that leads to magmatic diversity, whereas mixing between chemically somewhat heterogeneous basalts during differentiation can account for the homogenization of incompatible trace-element ratios with decreasing MgO concentration. Unlike other incompatible-element components, P is anomalously enriched in some lower MgO basalts and hawaiites. For example, P_2O_5/K_2O weight ratios are between 0.3 and 0.8 for basalts that have MgO concentrations as low as 7 weight percent, but many lower MgO basalts and hawaiites have P_2O_5/K_2O values as great as 1.2 (fig. 4). Crystallization-differentiation of the typical phenocrysts of basalts cannot have produced this anomalous enrichment in P, and its origin is interpreted subsequently to be caused by assimilation of apatite-bearing cumulates, also from the Harrat Rahat magmatic system.

Mafic and intermediate-composition rocks of the northern Harrat Rahat volcanic suite have incompatible trace-element ratios that are similar in many respects to those of average midocean ridge basalts (MORB) (Gale and others, 2013), and the suite shows no trend in these ratios toward values typical of continental crust (Hacker and others, 2015).

Figure 4. Plots of major-oxide concentrations, concentration ratios, and Mg number (Mg#) versus MgO concentrations for Quaternary volcanic rocks of northern Harrat Rahat. Rocks are distinguished by rock type (Cox and others, 1979) and CIPW-normative mineral assemblage; rock compositions are from Downs (2019). Abbreviations: Hy, hypersthene; Mg#, Mg number (=100×Mg/[Mg+Fe^{2+}], molar); Ne, nepheline; Qtz, quartz.

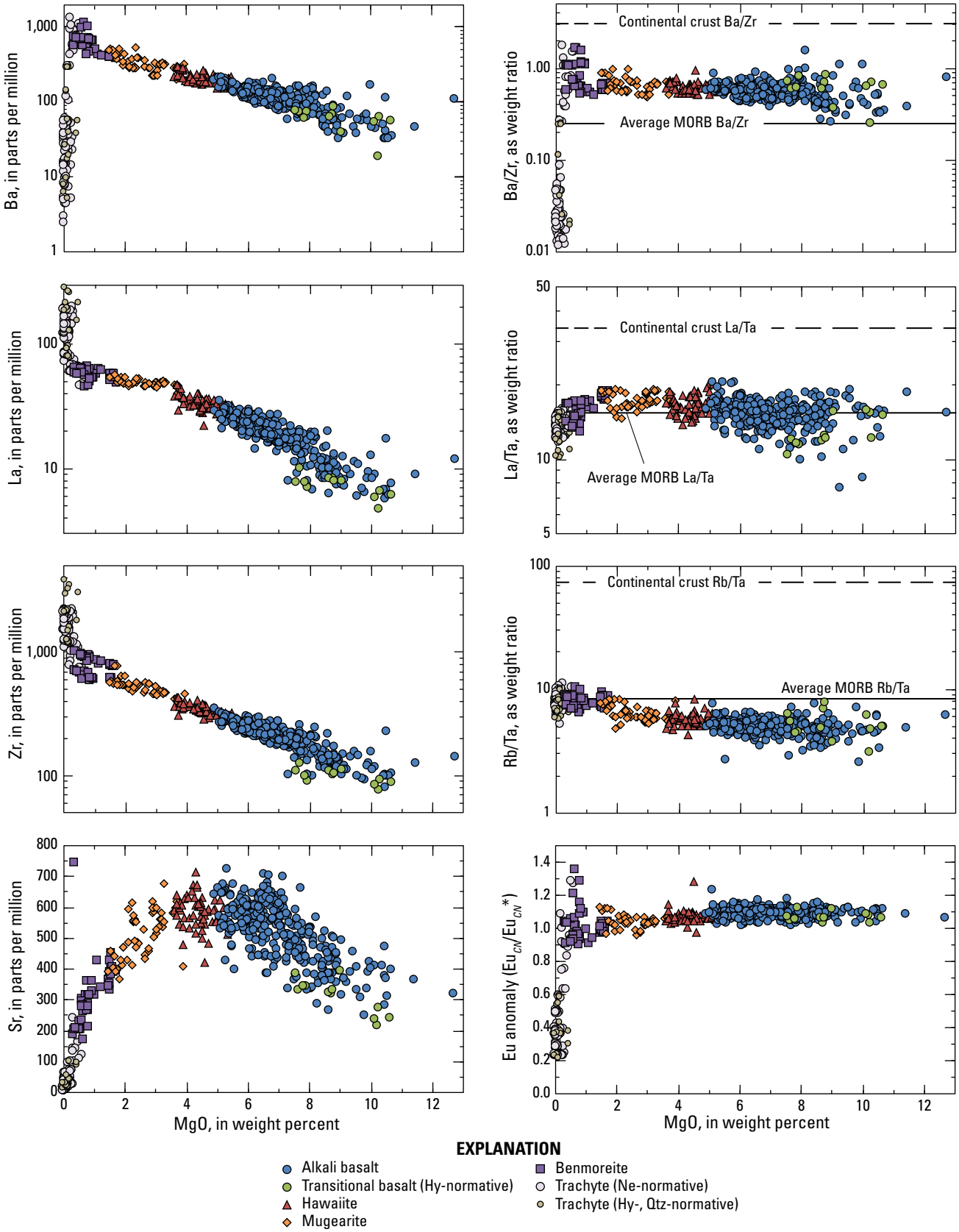
Ba, in parts per million
1,000
100
10
1
Ba/Zr, as weight ratio
Continental crust Ba/Zr
Average MORB Ba/Zr
1.00
0.10
0.01
La, in parts per million
100
10
La/Ta, as weight ratio
50
Continental crust La/Ta
Average MORB La/Ta
10
5
Zr, in parts per million
1,000
100
Rb/Ta, as weight ratio
100
Continental crust Rb/Ta
Average MORB Rb/Ta
10
1
Sr, in parts per million
800
700
600
500
400
300
200
100
0
Eu anomaly (Eu_{CN}/Eu_{CN}^*)
1.4
1.2
1.0
0.8
0.6
0.4
0.2
0.0
0
2
4
6
8
10
12
MgO, in weight percent
MgO, in weight percent
EXPLANATION
Alkali basalt
Transitional basalt (Hy-normative)
Hawaiite
Mugearite
Benmoreite
Trachyte (Ne-normative)
Trachyte (Hy-, Qtz-normative)

Table 1. Median major-oxide compositions, divided by Mg number, of Quaternary basalts and hawaiites of northern Harrat Rahat.

[Transitional basalts are weakly hypersthene normative; alkali basalts (AB) and hawaiites are nepheline normative. Concentrations normalized to 100 weight percent (wt. %). Median compositions exclude samples that have original analytical totals <99.0 wt. %, as well as two basalts that have anomalously high Ce concentrations relative to La and Pr; FeO and Fe_2O_3 calculated for melts at quartz-fayalite-magnetite oxygen fugacity. Original analyses by X-ray fluorescence, as reported in Downs (2019). Other abbreviations: Mg#, Mg number (=100×Mg/[Mg+Fe^{2+}], molar); n, number of samples in category]

Category	n	SiO_2	TiO_2	Al_2O_3	Fe_2O_3	FeO	MnO	MgO	CaO	Na_2O	K_2O	P_2O_5
Transitional basalts	13	47.8	1.52	16.0	1.82	9.38	0.18	8.80	11.2	2.66	0.32	0.16
AB, Mg# ≥64.0	18	46.8	1.57	15.8	1.82	9.42	0.17	10.30	11.0	2.67	0.31	0.17
AB, Mg# 63.9–60.0	41	46.9	1.90	16.2	1.90	9.78	0.18	8.66	10.8	2.92	0.40	0.22
AB, Mg# 59.9–55.0	75	46.9	2.27	16.3	2.02	10.3	0.19	7.65	9.66	3.42	0.71	0.36
AB, Mg# 54.9–50.0	127	46.5	2.88	16.4	2.15	10.9	0.20	6.63	9.10	3.75	0.83	0.47
AB, Mg# <50	94	46.8	2.99	16.5	2.20	11.0	0.21	5.81	8.60	4.13	0.99	0.74
Hawaiites	53	48.1	2.67	16.4	2.25	10.9	0.23	4.48	7.59	4.79	1.39	0.99

Trace-Element Aspects of Basalts and Hawaiites

Median major-oxide and trace-element compositions of basalts and hawaiites of northern Harrat Rahat, subdivided by Mg# values, are presented in tables 1 and 2. Figure 6 shows the median rare earth element (REE) concentrations normalized to chondrites (O'Neill, 2016) and as a selection of strongly to moderately incompatible elements normalized to average MORB (Gale and others, 2013). The basalts and hawaiites are enriched in the light REE, having small positive Eu anomalies (1.07±0.01), and their REE concentrations increase systematically with decreasing Mg#, more so for the strongly incompatible light REE (La by about 4.3 times) than for the less incompatible heavy REE (Yb by about 1.8 times). Median-REE concentrations for the small number of transitional basalts are indistinguishable from those of alkali basalts that have the highest Mg# (Mg# >64). On the MORB-normalized plot, elements are arranged from left to right in approximate order of decreasing incompatibility during low-degree partial melting of nominally anhydrous spinel-lherzolite. Notable features in the rocks that have the highest Mg# are small positive-concentration anomalies for Ba and K and a pronounced positive-concentration anomaly for Sr. As with the REE, the transitional basalts are similar to the highest Mg# alkali basalts; small differences for the more incompatible elements are possibly due to the small numbers of transitional-basalt analyses. The Ba and K positive-concentration anomalies persist in magnitude through the basalts into the hawaiites, whereas the Sr anomaly diminishes throughout the succession. A positive-concentration anomaly develops for P with decreasing Mg#, and Ti develops a small negative-concentration anomaly passing from the lower Mg# basalts to the median-concentration hawaiites.

Figure 5. Plots of trace-element concentrations, concentration ratios, and Eu anomalies versus MgO concentrations for Quaternary volcanic rocks of northern Harrat Rahat. Rocks are distinguished by rock type (Cox and others, 1979) and CIPW-normative mineral assemblage; rock compositions are from Downs (2019). Shown for reference are concentration ratios of selected incompatible trace elements (Ba/Zr, La/Ta, and Rb/Ta) in continental crust (dashed black lines; median ratio values from Hacker and others, 2015) and in average midocean ridge basalts (MORB) (solid black lines; from Gale and others, 2013). Other abbreviations: *CN* (as subscript), element concentration normalized to (divided by) its concentration in chondritic meteorites; Eu^*_{CN}, $\sqrt{Sm_{CN} \times Gd_{CN}}$; Hy, hypersthene; Ne, nepheline; Qtz, quartz.

Table 2. Median trace-element concentrations, divided by Mg number, of Quaternary basalts and hawaiites of northern Harrat Rahat.

[Transitional basalts are weakly hypersthene normative; alkali basalts and hawaiites are nepheline normative. Concentrations in parts per million by weight. Analyses of V, Ni, Cr, Zn, and Cu by X-ray fluorescence; all others, by inductively coupled plasma mass spectrometry, as reported in Downs (2019). Other abbreviation: Mg#, Mg number (=100×Mg/[Mg+Fe^{2+}], molar)]

Element	Transitional basalts	Alkali basalts					Hawaiites
		Mg# ≥64.0	Mg# 63.9–60.0	Mg# 59.9–55.0	Mg# 54.9–50.0	Mg# <50	
Cs	0.02	0.03	0.03	0.05	0.07	0.08	0.11
Rb	2.8	2.4	2.8	5.6	6.8	8.0	11.5
Ba	63	48	59	95	116	153	213
Sr	321	366	410	483	571	577	590
Y	21	20	21	25	28	33	40
Zr	100	105	128	183	214	259	342
Hf	2.49	2.51	3.00	4.13	4.72	5.56	7.16
Nb	8.0	7.0	8.6	16.4	19.4	22.5	30.9
Ta	0.61	0.50	0.62	1.12	1.36	1.54	2.03
Th	0.55	0.49	0.59	1.12	1.28	1.49	2.11
U	0.13	0.18	0.22	0.36	0.42	0.51	0.69
La	7.69	7.84	9.84	16.0	19.2	24.4	33.7
Ce	18.7	19.3	23.9	37.9	45.3	58.4	79.1
Pr	2.64	2.76	3.32	5.05	6.09	7.92	10.4
Nd	12.0	12.5	14.8	21.7	26.3	34.3	44.3
Sm	3.32	3.43	3.90	5.31	6.21	7.94	9.99
Eu	1.27	1.29	1.48	1.92	2.27	2.77	3.49
Gd	3.87	3.85	4.33	5.48	6.25	7.78	9.57
Tb	0.68	0.67	0.73	0.90	1.01	1.21	1.50
Dy	4.24	4.15	4.47	5.31	5.91	7.07	8.67
Ho	0.85	0.81	0.87	1.02	1.14	1.34	1.61
Er	2.26	2.12	2.25	2.63	2.91	3.32	4.10
Tm	0.31	0.29	0.31	0.36	0.39	0.45	0.57
Yb	1.89	1.76	1.84	2.15	2.35	2.68	3.36
Lu	0.29	0.26	0.28	0.33	0.36	0.41	0.51
Sc	32.8	31.1	29.4	26.6	24.7	22.8	19.9
V	259	253	263	251	260	226	159
Ni	179	251	159	128	81	55	22
Cr	335	430	280	198	109	54	2
Zn	81	80	84	89	92	100	112
Cu	110	109	98	77	59	52	40
Pb	0.76	0.77	0.89	1.38	1.60	1.92	2.57

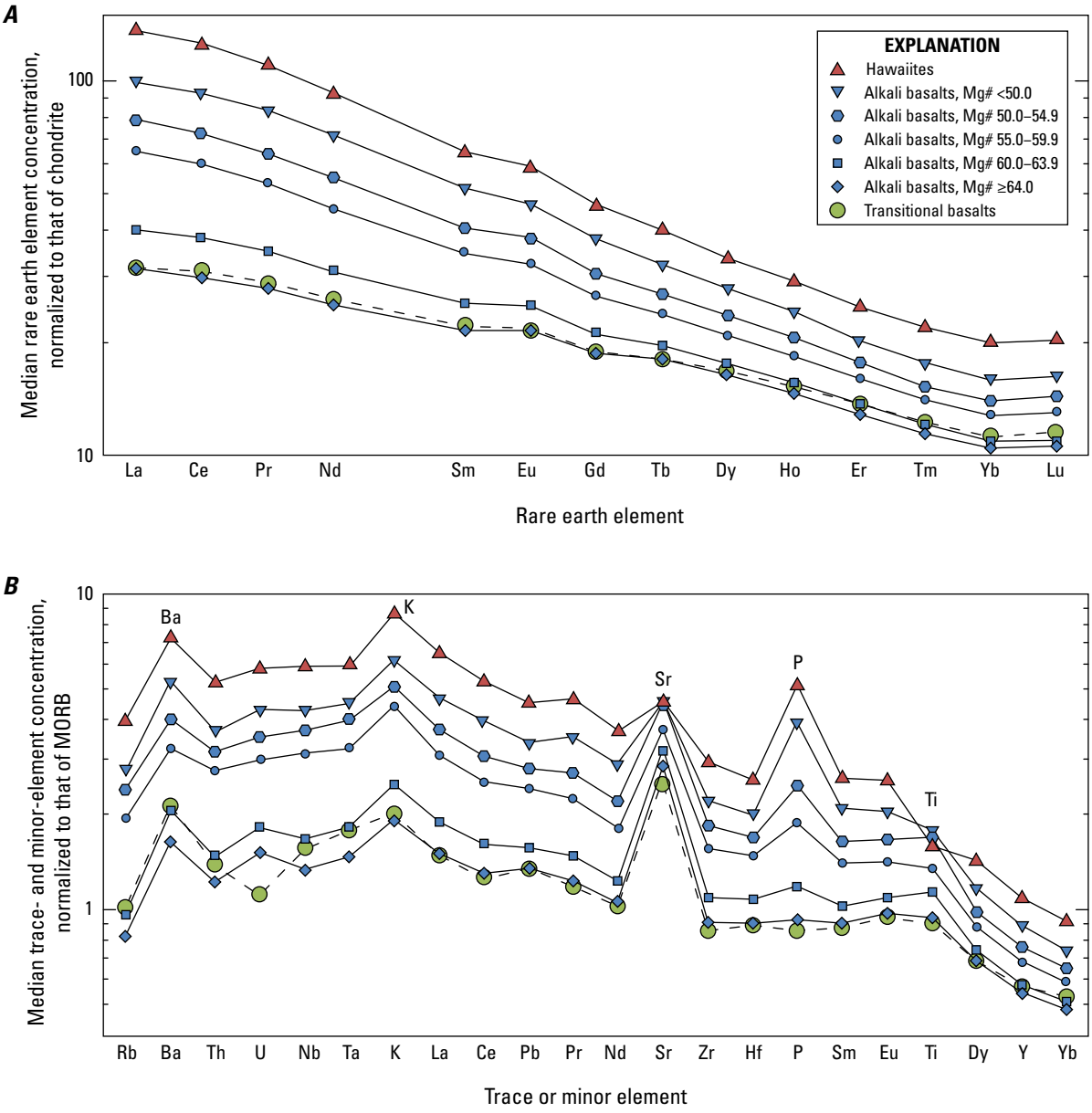

Figure 6. Plots of median concentrations of trace elements of Quaternary basalts and hawaiites of northern Harrat Rahat, normalized to (*A*) those of chondrites (O'Neill, 2016) and (*B*) those of average midocean ridge basalts (MORB) (Gale and others, 2013). Rocks are distinguished by rock type (Cox and others, 1979) and by Mg# (see table 2); rock compositions are from Downs (2019). In *B*, elements are ordered following left-to-right sequence of decreasing incompatibility, as estimated by Sun and McDonough (1989) for partial melting of upper mantle peridotite. Other abbreviation: Mg#, Mg number (=100×Mg/[Mg+Fe^{2+}], molar).

Radiogenic Isotopes

Salters and others (2023) inferred mantle source characteristics and crustal interaction for northern Harrat Rahat magmas on the basis of new, high-precision Sr, Nd, Pb, and Hf isotopic measurements for 70 acid-cleaned samples spanning from magnesian basalt to trachyte, as well as on fewer previously published measurements from Moufti and others (2012). Key findings are that the new high-precision Pb determinations demonstrate incorporation of crustal materials progressively across the basalt-to-trachyte spectrum but that total amounts of crust incorporated were quite small (as much as 5 weight percent, on the basis of simple mixing and assimilation-fractional crystallization models). Additionally, the materials assimilated from the Neoproterozoic crust had low long-term U/Pb and Th/Pb ratios, consistent with both the whole-rock Pb isotopic values of the Arabian–Nubian Shield's lower crust and the common Pb values of the western part of the Arabian Shield's upper crust. The mantle source for the basalts was similar isotopically to depleted mantle (DM) but was displaced modestly toward isotopic values ascribed to the Afar mantle plume and (or) enriched MORB. No narrow estimates can be made of the amount of Afar plume material in the harrat source because MORB are isotopically diverse, even those not associated with mantle plumes, and because no single set of Sr, Nd, Pb, and Hf isotopic values is accepted for the Afar plume itself. However, commonly proposed values allow for as much as 20 to 30 weight percent Afar plume combined with asthenospheric DM as the harrat's source. Isotopic values of the lithospheric upper mantle beneath the Arabian–Nubian Shield scatter widely around those of the narrower ranges of harrat basalts, and of basalts of the active Red Sea and Gulf of Aden spreading systems, and, if such subcontinental lithosphere contributes to harrat magmatism, either it does so in small quantities, or its isotopic diversity is greatly homogenized by the melting process. Trace-element variations of northern Harrat Rahat basalts are intermediate between those expected for melting in the garnet- and spinel-peridotite-stability fields, consistent with melting at depths that span that transition, and pyroxenite was not a dominant component in the source undergoing melting.

Petrogenetic Interpretations

Differentiation Stages of Basalts and Hawaiites

The influences of different minerals on basalt-to-hawaiite differentiation can be discerned in trace-element and major-oxide variation diagrams versus whole-rock MgO concentration (fig. 7). As expected from the ubiquitous olivine phenocrysts, Ni concentrations decrease smoothly with decreasing MgO concentration, consistent with olivine as a member of the fractionating mineral assemblage. Concentrations of Sc also decrease with decreasing MgO concentration, at least among rocks that have MgO concentrations less than about 10 weight percent, identifying calcic clinopyroxene as a member of the fractionating mineral assemblage despite its absence as a phenocryst in basalts and hawaiites. Some high-MgO samples plot off the main Sc versus MgO trend, consistent with an initial olivine-dominated differentiation stage or with olivine accumulation in some of the higher MgO rocks. Concentrations of V increase modestly with decreasing MgO concentration among rocks that have MgO concentrations greater than 6 to 7 weight percent, but they decrease markedly at lower MgO concentrations. This change in trend of V concentrations matches the peak in whole-rock TiO_2 concentrations (fig. 4) and is consistent with titanomagnetite having joined the fractionating mineral assemblage at 6 to 7 weight percent MgO in the basaltic liquids. The V field is also broadest at about 7 weight percent MgO, consistent with mixing between variably differentiated basalts. Early involvement of plagioclase during differentiation is identified by plots of Sr/Nd ratios and of Al_2O_3/K_2O ratios versus MgO concentration. The elements Sr and Nd have similar incompatibility in calcic clinopyroxene, as well as such strong incompatibility in olivine that Sr/Nd ratios of melt are not changed appreciably by growth and separation of those mafic minerals. Decreasing Sr/Nd values with decreasing MgO concentration, certainly among rocks that have MgO concentrations as much as 9 weight percent, and possibly as much as about 10.5 weight percent, identify plagioclase as a member of the fractionating mineral assemblage. Scatter in Sr/Nd ratio values at MgO concentrations greater than about 9 weight percent suggests an early olivine-dominated differentiation interval or some olivine accumulation. Crystallization of plagioclase is also shown by generally decreasing Al_2O_3/K_2O with decreasing MgO concentration, but as with Sc concentrations and Sr/Nd ratios, some of the higher MgO rocks plot below the main Al_2O_3/K_2O ratio trend at MgO concentrations greater than 9 weight percent, consistent with early olivine-dominated fractionation or selective accumulation.

Transitional basalts span only the more MgO-rich compositions observed at northern Harrat Rahat; hence, they do not show evidence of Fe-Ti oxide or apatite fractionation that are apparent in some alkalic members of the suite. Transitional basalts show trace-element characteristics that are consistent with a fractionating assemblage strongly dominated by olivine—that is, generally flat trends in plots of Sc concentrations, Sr/Nd ratios, and Al_2O_3/K_2O ratios versus MgO concentrations.

In summary, the geochemical relations of the basalts and hawaiites of northern Harrat Rahat identify olivine, plagioclase, calcic clinopyroxene, and titanomagnetite as the minerals whose growth and separation drove differentiation, as well as that this differentiation can be divided broadly into three successive stages. The earliest or least evolved stage, recorded by compositional variations among the highest MgO rocks, resulted dominantly from olivine fractionation. Although some olivine accumulation may also have taken place, accumulation of olivine into otherwise ordinary Harrat Rahat basaltic magmas is an inadequate explanation

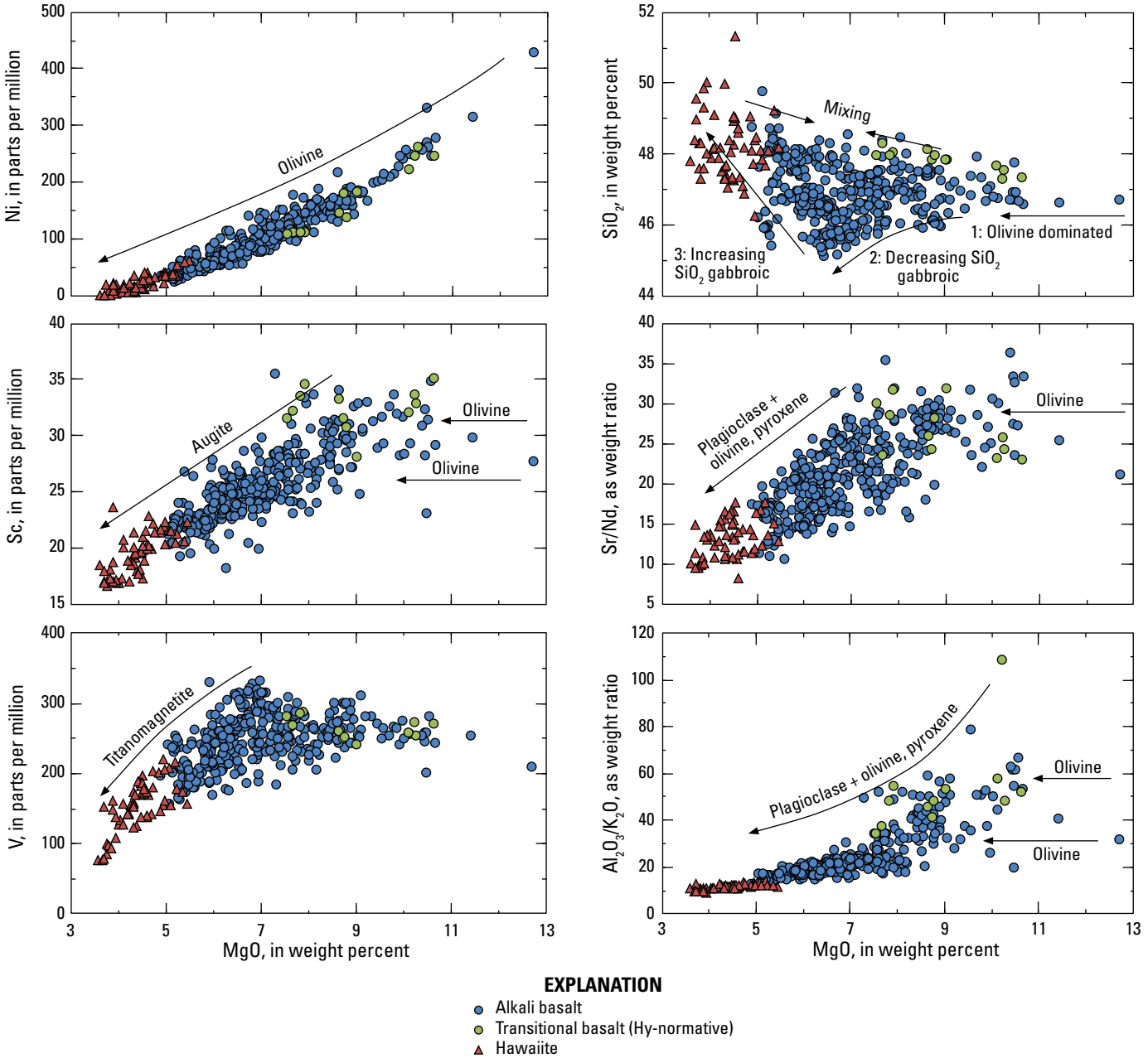

Figure 7. Plots of trace-element concentrations, major-oxide concentrations, and concentration ratios versus MgO concentrations for Quaternary basalts and hawaiites of northern Harrat Rahat. Arrows show how separating indicated minerals and mineral assemblages—and, in SiO_2 plot, also magma mixing—would affect magma compositions. Abbreviation: Hy, hypersthene.

for the high-MgO rocks because, as a group, they also have the most shallowly sloping REE patterns (fig. 6), which olivine accumulation alone would not produce. Olivine was joined by plagioclase and clinopyroxene once the MgO concentrations of basaltic melts fell below 9 to 10 weight percent. Separation of an olivine gabbroic mineral assemblage (olivine+plagioclase+calcic clinopyroxene) was divided into an earlier or less evolved interval free of titanomagnetite and a later, more evolved interval in which titanomagnetite had joined the crystallizing olivine gabbroic assemblage, with the transition between these intervals at 6 to 7 weight percent MgO in the basaltic melts. Variations of whole-rock SiO_2 versus MgO concentrations (fig. 7) are consistent with fractionation of the olivine gabbroic assemblage having first decreased the SiO_2 concentrations of melts, then increased melt SiO_2 concentrations, with the reversal having commenced about as titanomagnetite joined the fractionating olivine gabbroic assemblage. Most basalts of northern Harrat Rahat

plot in the interior of the triangular MgO versus SiO_2 field (fig. 7), consistent with common mixing between variably differentiated basaltic magmas. The geochemical evidence for calcic clinopyroxene as a member of the crystallizing assemblage contrasts with its absence as a phenocryst in the erupted basalts and hawaiites, but it may be reconciled if differentiation mainly took place deeper than the upper crust, as discussed subsequently.

Excess Phosphorous in Some Low-MgO Basalts and Hawaiites

Phosphorous is strongly excluded from olivine, plagioclase, pyroxene, and titanomagnetite, so its concentration in melts crystallizing those minerals should increase in proportion with other incompatible components. Phosphorous is, however, anomalously enriched in many of the more evolved basalts and hawaiites of northern Harrat Rahat, as illustrated by a plot of the P_2O_5/K_2O versus MgO concentration (fig. 4); similar patterns result referencing phosphorous to other highly incompatible components such as La, Ta, Zr, or Th (not illustrated). The magnitude of the excess can be large: the median P_2O_5/K_2O value is 0.56 for basalts that have Mg# of 60 or more (table 1), and none of these magnesian basalts has P_2O_5/K_2O values that exceed 0.8, whereas P_2O_5/K_2O values reach nearly 1.2 in some evolved basalts and hawaiites. This indicates that the most P-enriched rocks have at least 50 percent more P_2O_5 than would be consistent with their K_2O concentrations. Similar referencing to Zr indicates at least 70 relative percent excess P_2O_5 (not illustrated).

The preferred explanation for the excess-P_2O_5 rocks is that their magmas encountered apatite-bearing cumulates from which they dissolved apatite preferentially, as proposed by Bohrson and Reid (1995) for some similar excess-P_2O_5 alkali basalts from Isla Socorro, Mexico. Mugearites, benmoreites, and trachytes of northern Harrat Rahat define a trend of sharply and progressively declining P_2O_5 concentrations (fig. 4), consistent with production and separation of an apatite-bearing cumulus assemblage. Prior to the onset of alkali feldspar crystallization that commenced near the benmoreite-to-trachyte transition, this cumulus assemblage would have consisted of olivine, plagioclase, calcic clinopyroxene, titanomagnetite, and apatite. Basaltic magmas that assimilated such cumulates would already have been saturated with olivine, plagioclase, calcic clinopyroxene, and possibly titanomagnetite, so a principal effect of such assimilation would have been for the melts to consume cumulus apatite selectively. Segregation and ascent of the so-modified melts produced the excess-P_2O_5 volcanic rocks. Support for this interpretation is given by a plot of trace-element concentrations of basalts and hawaiites that have P_2O_5/K_2O values greater than 0.8 divided by the concentrations of similarly evolved basalts and hawaiites that have P_2O_5/K_2O values less than 0.8 (fig. 8). Concentration ratios of the REE define a gently dome-shaped pattern that shows the greatest enrichments in the middle REE, similar in shape to the apatite-to-melt partitioning of the REE (Watson and Green, 1981), as was also demonstrated by Bohrson and Reid (1995) for some Isla Socorro excess-P_2O_5 basalts. In contrast, net assimilation of feldspar, pyroxene, and titanomagnetite appears minor or lacking, judging from the small-to-absent relative enrichments of Sr, Ba, Sc, Ti, and V in the excess-P_2O_5 basalts and hawaiites. Incorporation of a late-stage, P_2O_5-rich, immiscible silicate liquid is also not supported on the basis of the lack of Fe enrichment (fig. 8), as is characteristic for P_2O_5-enriched immiscible liquids in tholeiitic systems (Roeder and Weiblen, 1970; Charlier and others, 2013). Selective assimilation of about 1 weight percent apatite would produce the average P_2O_5 enrichment of basalts and hawaiites that have P_2O_5/K_2O values greater than 0.8 from the average of their normal P_2O_5/K_2O counterparts.

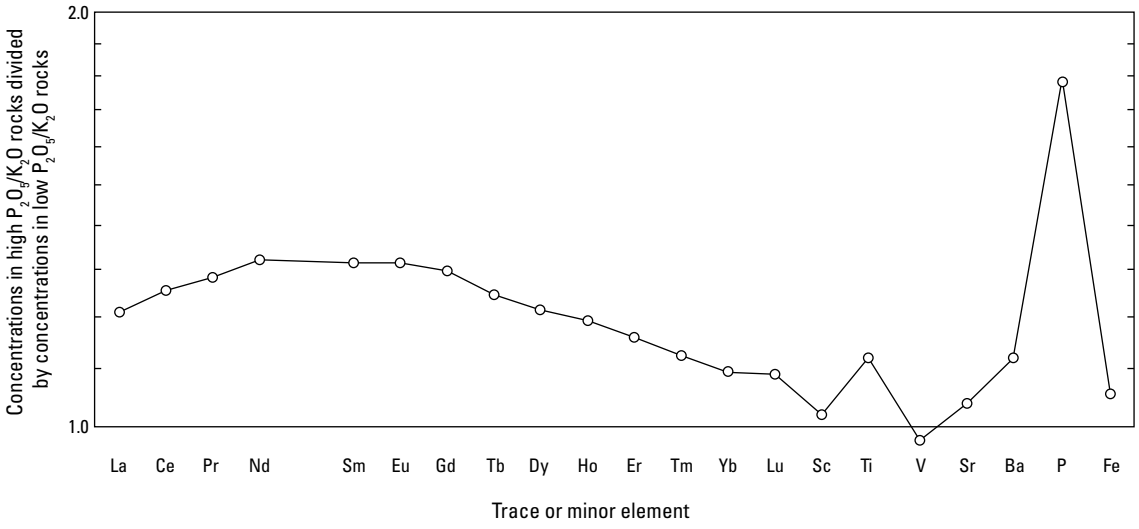

Figure 8. Plot of median trace- and minor-element concentrations in Quaternary basalts and hawaiites of northern Harrat Rahat that have P_2O_5/K_2O weight ratios greater than 0.8, divided by those elements' median concentrations in basalts and hawaiites that have P_2O_5/K_2O ratios less than 0.8, at same MgO concentration range.

Cumulate Compositions and Mineral Assemblages During Gabbroic Differentiation

Bulk compositions, mineral assemblages, and mineral proportions for basalt-to-hawaiite differentiation are informative of the likely depths of magma storage and differentiation beneath the volcanic field. Major-oxide compositions of gabbroic cumulates were estimated by first subdividing basalt and hawaiite analyses into the early (or less evolved) decreasing-silica, and subsequent (or more evolved) increasing-silica differentiation stages. Members of these stages can be separated roughly by whole-rock Na_2O+K_2O concentrations of either less than or greater than $19.38 - 0.3256 \times SiO_2$ (in weight percent), respectively. Excluded from consideration were rock compositions that have Mg# greater than 64 to exclude basalts on the initial olivine-dominated differentiation stage, as well as rocks that have P_2O_5/K_2O values greater than 0.8, to exclude evolved basalts and hawaiites that may have selectively assimilated apatite. Representative cumulate compositions were then estimated for the two gabbroic stages by drawing straight lines along the greatest densities of basalt and hawaiite compositions in plots of major oxides versus MgO and SiO_2 concentrations, requiring that the model cumulates have zero concentrations of K_2O and P_2O_5. Although subjective, this approach proved superior to wholly numerical methods such as least-squares regressions, which lack the benefit of a petrologist's eye to see trends and exclude outliers. The actual cumulates inarguably encompass greater and more continuous compositional diversity than these general estimates for the two gabbroic stages, but further subdivision comes at the cost of even greater subjectivity that was judged to be unwarranted.

As expected, the derived cumulates have gabbroic compositions (table 3), with the early decreasing-silica differentiation stage cumulate being magnesian and relatively silicic but poor in sodium and titanium and with the cumulate for the subsequent increasing-silica stage being poorer in silica but rich in iron and titanium. The potential mineralogy of these cumulates was estimated across a range of crustal and upper mantle pressures and near-solidus temperatures (fig. 9) using the thermodynamic programs Perple_X (Connolly, 2009) and pMELTS (Ghiorso and others, 2002). The MELTS thermodynamic calibration (Ghiorso and Sack, 1995) was also applied but failed to define a simple solidus for the model cumulates, instead predicting persistence to quite low temperatures of a SiO_2-poor, Fe-oxide-rich liquid; hence, those results are not presented. Cumulate assemblages would be ordinary olivine gabbros across most crustal depths, dominated by intermediate-composition plagioclase, followed by, in decreasing abundance, calcic clinopyroxene and olivine. Garnet is predicted as being stable in both cumulate compositions at pressures approaching and exceeding the base of the continental crust, where the predicted abundances of plagioclase and olivine diminish greatly and the predicted plagioclase becomes distinctly sodic owing to reactions that would create Al-spinel, garnet, and Ca-rich clinopyroxene components. Ilmenite saturation predicted by the Perple_X simulations is an artifact of employing pyroxene and melt solution models that lack titanium components (Jennings and Holland, 2015; Green and others, 2016). The predicted stability of minor orthopyroxene in Perple_X simulations across the shallow through middle crust may also result from this simplification because formation of ilmenite removes Fe from the silicate assemblage, shifting it to greater Mg# where the miscibility gap between augite and low-Ca pyroxene is broader (Lindsley, 1983). The following discussion concentrates on the pMELTS results because its mineral-solution models encompass more compositional components and because the Perple_X results are similar and supportive.

Table 4 and figure 10 present the proportions of minerals and the compositions of plagioclase and olivine along the solidus for model cumulates of the decreasing-silica and subsequent increasing-silica differentiation stages as predicted by pMELTS. The bulk cumulate for the initial decreasing-silica differentiation stage is calculated to be richer in olivine and augite and poorer in plagioclase than that for the subsequent increasing-silica stage. The latter cumulate would also be distinctly richer in a titaniferous spinel, and its plagioclase and olivine would be more albitic and fayalitic, respectively. Modal assemblages remain olivine gabbro (early cumulate) or titanomagnetite-olivine gabbro (later cumulate) for depths that span the shallow through middle crust, but plagioclase and olivine abundances would be diminished if the cumulates formed at pressures greater than about 700 or 800 megapascals (MPa), where the cumulates would consist of melagabbro and mela-Fe-Ti-oxide gabbro, and would

Table 3. Major-oxide compositions estimated for a representative parent magma for Quaternary basalts of northern Harrat Rahat, as well as for the bulk high- and low-SiO_2 gabbroic cumulates produced during magma differentiation from basalt through hawaiite.

[Concentrations in weight percent (wt. %). Representative parent magma is median alkali basalt that has Mg# (Mg number, $=100\times Mg/[Mg+Fe^{2+}]$) >64 (see table 1) but has Fe_2O_3/FeO ratio raised and minor H_2O added, then renormalized to 100 wt. %, as described in text]

	SiO_2	TiO_2	Al_2O_3	Fe_2O_3	FeO	MnO	MgO	CaO	Na_2O	K_2O	P_2O_5	H_2O
Representative parent magma	46.7	1.6	15.8	2.6	8.7	0.17	10.3	11.0	2.7	0.3	0.17	0.2
Bulk cumulate, decreasing-SiO_2 leg	47.5	1.0	14.5	1.5	8.0	0.15	12.5	13.0	2.0	0.0	0.0	0.0
Bulk cumulate, increasing-SiO_2 leg	44.0	4.0	16.5	2.0	12.0	0.17	8.5	10.0	3.0	0.0	0.0	0.0

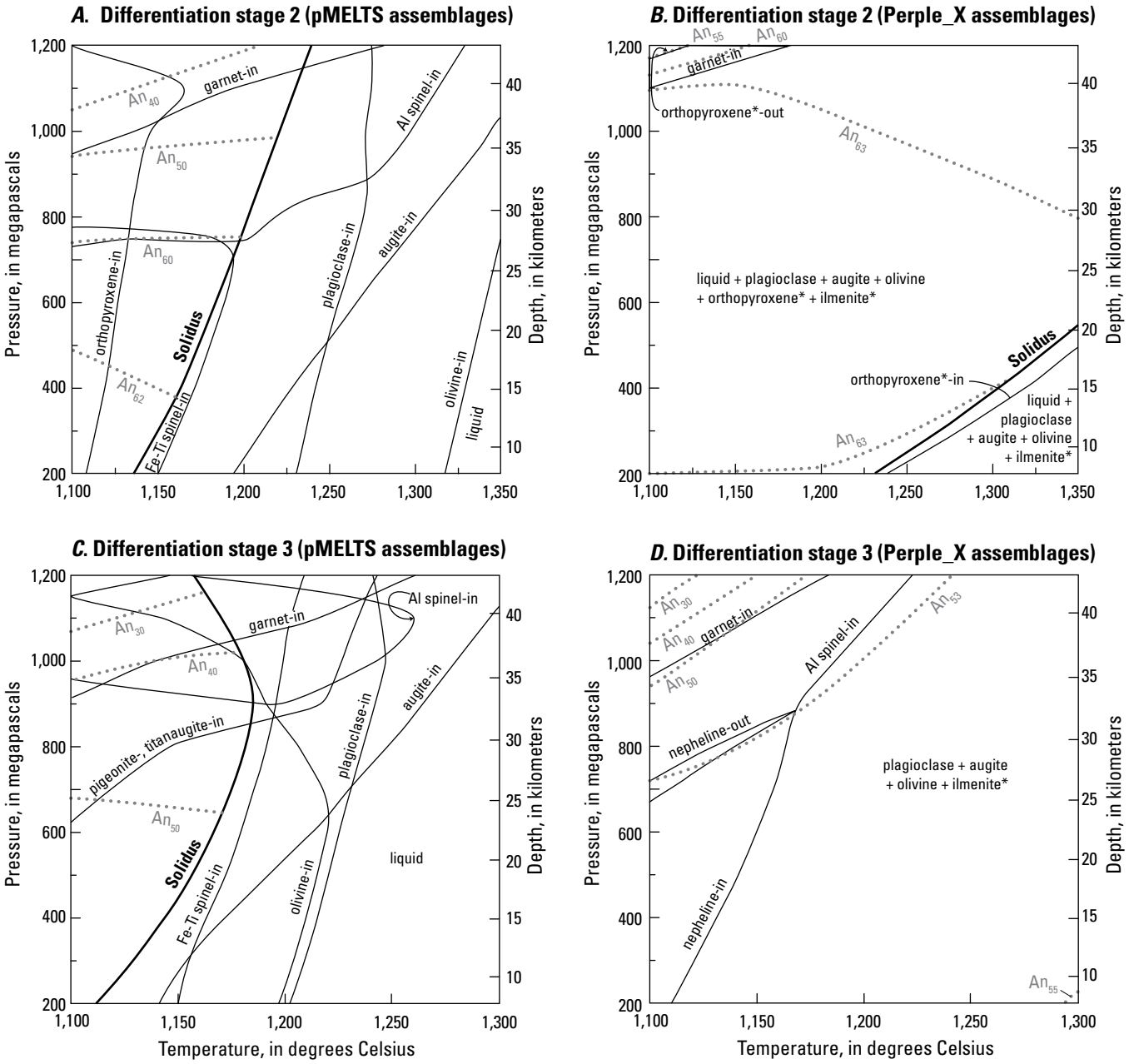

Figure 9. Diagrams showing pressure (and depth) versus temperature phase-stability limits calculated for bulk cumulate compositions (see table 3) for initial decreasing- and subsequent increasing-SiO_2 stages of gabbroic differentiation for Quaternary basalts and hawaiites of northern Harrat Rahat. Results are from thermodynamic models pMELTS (*A*, *C*; see also, table 4) (Ghiorso and others, 2002) and Perple_X (*B*, *D*) (Connolly, 2009). *A*, Differentiation stage 2, gabbro cumulate; pMELTS assemblages. *B*, Differentiation stage 2, gabbro cumulate; Perple_X assemblages. *C*, Differentiation stage 3, Fe-Ti-oxide gabbro cumulate; pMELTS assemblages. *D*, Differentiation stage 3, Fe-Ti-oxide gabbro cumulate; Perple_X assemblages. Heavy, solid black lines show solidi. Thin, solid black lines show stability curves of major mineral phases (asterisks [*] indicate that ilmenite and orthopyroxene have questionable true stability owing to Ti-free silicate-solution models); dotted lines show equilibrium plagioclase compositions in mole percent anorthite (An); "<*phase*>-in" labels or leaders are placed on mineral-stable sides of stability curves; "<*phase*>-out" labels or leaders indicate high-pressure-, low-temperature-stability limits of indicated minerals. Perple_X calculations use the thermodynamic dataset of Holland and Powell (2011); activity models for clinopyroxene and melt from Green and others (2016); for plagioclase and orthopyroxene, from Jennings and Holland (2015); for olivine, from Kawasaki (1998) and modified by Perple_X; for spinel, from White and others (2002) and modified by Perple_X; for garnet, from White and others (2014); for ilmenite, from Andersen and Lindsley (1998); and for ternary feldspar, from Fuhrman and Lindsley (1988). Excluded phases are metallic Fe and quartz. Equivalent depths in continental crust calculated using rock density-to-depth profile of Christensen and Mooney (1995).

Table 4. Solidus modes and feldspar and olivine compositions calculated for gabbroic cumulates of northern Harrat Rahat.

[Solidus modes, in weight percent; feldspar and olivine compositions, in mole percent. Modal proportions and mineral compositions calculated for gabbro cumulate compositions (see table 3) using pMELTS thermodynamic model (Ghiorso and others, 2002). Decreasing- and increasing-SiO_2 legs are cumulates for early decreasing-SiO_2 and subsequent increasing-SiO_2 basalt-differentiation stages, MnO free. Abbreviations: An, anorthite component in feldspar (=100×[Ca/Na+Ca+K], molar); Aug, augite; Fo, forsterite component in olivine (=100×[Mg/Mg+Fe+Ca], molar); Gnt, garnet; Oliv, olivine; *P*, pressure, in megapascals (MPa); Pig, pigeonite; Plag, plagioclase; Spin, either Al-spinel or Ti-magnetite (or both); *T*, temperature, in degrees Celsius (°C); Ti-aug, titanaugite; —, undefined (phase not present)]

SiO_2 leg	*P* (MPa)	*T* (°C)	Plag	An	Oliv	Fo	Aug	Ti-aug	Pig	Gnt	Spin
Decreasing	200	1,136	44.1	62	21.3	73	32.1	0	0	0	2.6
	300	1,150	43.3	62	21.0	73	33.4	0	0	0	2.3
	400	1,163	42.4	62	20.7	73	34.9	0	0	0	2.1
	600	1,185	39.7	61	19.6	73	38.4	0	0.8	0	1.5
	800	1,202	32.8	58	15.0	72	46.2	0	4.1	0	1.9
	1,000	1,220	21.0	49	5.2	70	68.3	0	0.7	0	4.8
	1,100	1,230	17.3	55	2.9	55	74.8	0	0	0	5.0
	1,200	1,239	13.7	53	1.9	67	75.7	0	0	4.8	3.8
Increasing	200	1,111	51.6	52	16.5	63	20.0	0	0	0	11.9
	300	1,129	51.1	51	16.2	63	20.8	0	0	0	11.9
	400	1,144	50.7	51	15.8	63	21.8	0	0	0	11.9
	500	1,157	49.7	51	15.4	63	23.0	0	0	0	11.9
	600	1,167	48.8	50	14.8	63	24.5	0	0	0	11.9
	800	1,182	44.6	48	12.8	63	29.5	0	0	0	12.0
	1,000	1,182	34.7	42	4.1	61	45.6	0	1.8	0	13.8
	1,200	1,157	20.9	28	0	—	45.7	5.1	0	19.1	9.2

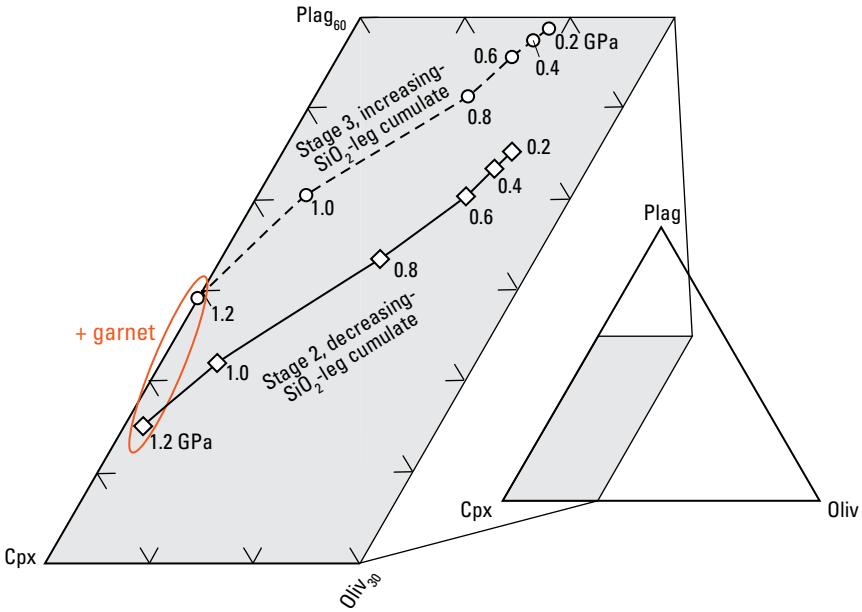

Figure 10. Part of plagioclase (Plag)–calcic clinopyroxene (Cpx)–olivine (Oliv) ternary diagram showing relative proportions, by mass percent, of those minerals calculated to be stable along solidus of bulk gabbroic-cumulate compositions for decreasing- and increasing-SiO_2 differentiation stages, at pressures (in gigapascals [GPa]) shown by diamonds and circles, for Quaternary basalts and hawaiites of northern Harrat Rahat. Mineral proportions are calculated with pMELTS (Ghiorso and others, 2002). Solid line, solutions at different pressures (diamonds) for differentiation stage 2, decreasing-SiO_2-leg bulk gabbro cumulate; dashed line, solutions at different pressures (circles) for differentiation stage 3, increasing-SiO_2-leg bulk gabbro cumulate. Orange ellipse shows pressures at which garnet would also be present.

approach the mineral proportions of garnet-plagioclase-bearing clinopyroxenites in the upper mantle (plutonic rock names from Streckeisen, 1976). Notably, plagioclase compositions near An_{60}, which match the compositions of rounded plagioclase megacrysts, are calculated for the early-stage cumulate at pressures equal to crustal depths shallower than about 27 km (fig. 9). This, as well as the aforementioned trace-element evidence for early plagioclase crystallization and the lack of trace-element evidence for garnet crystallization, all point toward storage and differentiation shallower than the crust-mantle interface—and probably shallower than the deepest one-third of the crust—to produce erupted northern Harrat Rahat magmas. Basaltic magmas may also lodge at greater depths, but if so, their differentiation products rarely reach the surface directly and unmodified.

Modeling of Magmatic Differentiation—Major-Oxide Results

Progressive crystallization-differentiation of basaltic magmas of northern Harrat Rahat was investigated with the MELTS and pMELTS thermodynamic calibrations of mineral-melt equilibria (Ghiorso and Sack, 1995; Ghiorso and others, 2002), using the median alkali basalt that has Mg# greater than 64 (table 1) as the parent magma composition. The H_2O concentration and relative proportions of Fe_2O_3 to FeO of this model parent were adjusted by trial and error to optimize correspondence between calculated liquid lines of descent and the natural basalt-to-hawaiite rock suite, yielding the adjusted parent magma composition in table 3. Those values of Fe_2O_3 and FeO would equate to an fO_2 of QFM+1 (in $\log_{10}$ units) at the 1-bar liquidus of the parent basalt composition. Only the pMELTS results are presented and discussed because the MELTS calibration is not suitable for pressures that exceed about 800 MPa; in addition, it predicts that, for the employed composition, olivine would appear only at substantially subliquidus temperatures at pressures exceeding about 500 MPa.

Modeled phase-stability results (fig. 11) are long familiar from—and are founded on—melting experiments on nominally dry basalts (Yoder and Tilley, 1962; Thompson, 1974, 1975). The basic features are that olivine defines the liquidus from near-surface to middle or lower crustal pressures, giving way to liquidus calcic clinopyroxene at greater pressures, and that plagioclase would crystallize following olivine at pressures through the shallow one-third to one-half of the crust. Titanomagnetite would crystallize following olivine, plagioclase, and calcic clinopyroxene, at pressures as much as about 750 MPa; however, at greater pressures, it would be replaced by an Al-rich spinel, and garnet would be stable at pressures near the base of the continental crust (>35 km deep; 1,000 MPa). Further details are that calcium-poor pyroxenes are stable at deep-crustal pressures; that at higher temperatures near 1,100 °C, pigeonite gives way to orthopyroxene; and that the SiO_2 concentration of the melt reaches a minimum near the onset of spinel crystallization.

Notable aspects of the modeled liquid lines of descent (fig. 12) are that early crystallization of olivine, alone, appreciably decreases the MgO concentration of the melt while increasing its SiO_2 concentration only modestly. The SiO_2 concentration of the melt falls sharply once calcic clinopyroxene joins the crystallizing assemblage, then it reverses once titanomagnetite or Al-rich spinel commence crystallizing. The reduction in melt-SiO_2 concentration is greatest for simulations of 600 to 700 MPa. Silica-reduction diminishes at lower pressures owing to a lesser extent of pyroxene crystallization prior to titanomagnetite saturation. It also diminishes at greater pressures owing to the combined effects of Al-rich spinel joining the near-liquidus crystallizing assemblage and the modeled clinopyroxene becoming Al-rich and Si-poor, owing to Tschermak's substitutions. The magnitude and MgO concentration of the SiO_2 "well" on the modeled liquid lines of descent and the trajectories of their CaO/Al_2O_3 values versus MgO concentrations most closely

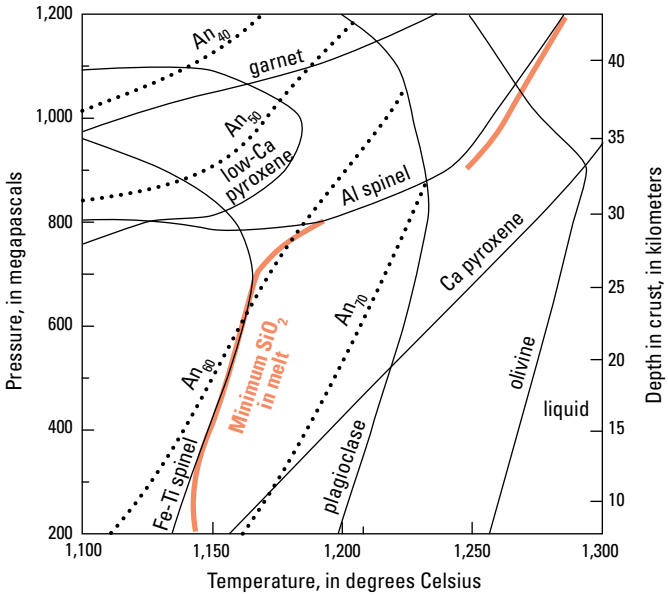

Figure 11. Diagram showing pressure (and depth) versus temperature phase-stability limits calculated using thermodynamic model pMELTS (Ghiorso and others, 2002) for median alkali basalt composition of northern Harrat Rahat. Median alkali basalt composition has Mg# greater than 64 (see table 1) but has Fe_2O_3/FeO raised (see table 3) so that modeled onset of titanomagnetite crystallization matches peak-TiO_2 versus MgO and SiO_2 concentration relations of basalt-to-hawaiite suite. Thick orange lines show pressure-temperature trace of minimum-SiO_2 concentrations for modeled liquid lines of descent. Solid black lines show stability curves of indicated mineral phases; dotted lines show equilibrium anorthite compositions of plagioclase (An), in mole percent. Equivalent depths in continental crust calculated using rock density-to-depth profile of Christensen and Mooney (1995).

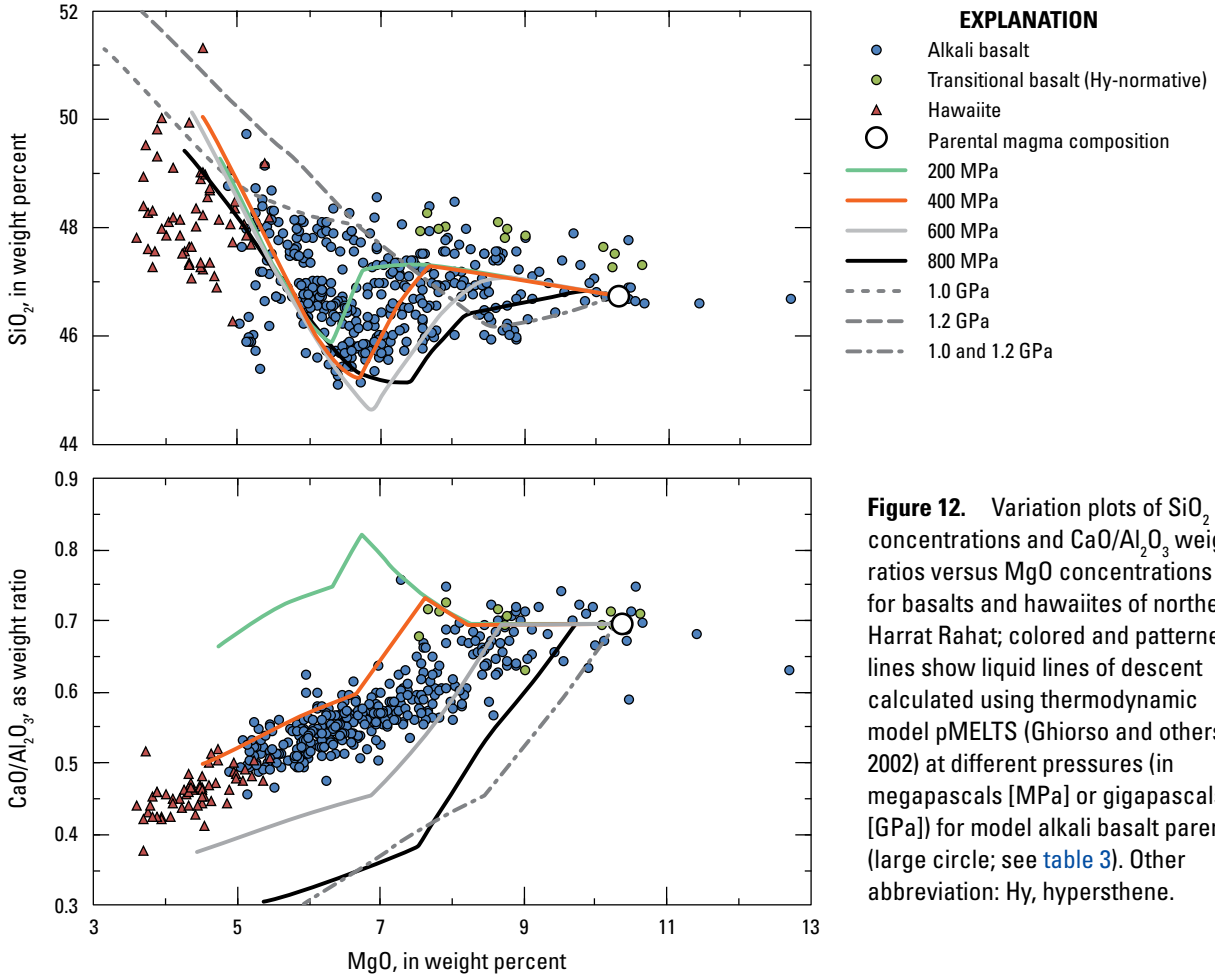

Figure 12. Variation plots of SiO_2 concentrations and CaO/Al_2O_3 weight ratios versus MgO concentrations for basalts and hawaiites of northern Harrat Rahat; colored and patterned lines show liquid lines of descent calculated using thermodynamic model pMELTS (Ghiorso and others, 2002) at different pressures (in megapascals [MPa] or gigapascals [GPa]) for model alkali basalt parent (large circle; see table 3). Other abbreviation: Hy, hypersthene.

match the natural basalt-through-hawaiite suite for simulations at pressures of 400 to 600 MPa (fig. 12), or at depths in the crust of about 15 to nearly 25 km (fig. 11). Differentiation dominantly in the deep crust is unsupported on the basis of both the lack of trace-element evidence that would indicate garnet crystallization and the absence of major-oxide evidence for crystallization of predominantly calcic clinopyroxene early during differentiation. Differentiation dominantly in the shallow crust is judged as being unlikely owing to the absence of trace-element and major-oxide evidence for extensive crystallization of troctolite (olivine+plagioclase), such as increasing CaO/Al_2O_3 values with decreasing MgO concentrations, as well as from the absence of appreciable surface geothermal features and upper crustal seismicity that would accompany sizeable shallow active intrusions. The basalt-through-hawaiite suite lacks the narrow compositional trends and segmented crystallization intervals of the isobaric simulations, but mixing between more and less evolved magmas produced over a range of midcrustal pressures may account for the smoothed compositional arrays and the infilling of the SiO_2 "well" in the natural suite. The simulations support the inference that newly injected primitive magmas first crystallized small amounts of dunite (olivine cumulate) or olivine-rich troctolite, giving way first to olivine gabbro crystallization that decreased SiO_2 in the melts, then to titanomagnetite-olivine gabbro crystallization that increased melt SiO_2 concentrations, leading to hawaiite; however, these stages are a generalized view of more complex crystallization sequences, and the details are partly blurred and obscured by mixing.

Differentiation chiefly in the midcrust may be due to ascending basaltic melts losing positive buoyancy in that depth region. Along its liquidus, the parent magma for the initial gabbroic differentiation interval (table 3) can be calculated through pMELTS to have a density of 2.83 grams per cubic centimeter (g/cm^3) near the base of the crust (40 km depth), declining to 2.78 g/cm^3 in the midcrust (20 km depth) and 2.75 g/cm^3 in the upper crust (3 km depth). The continental crust density-depth profile of Christensen and Mooney (1995) indicates that average crust deeper than 20 km is denser than

such a basaltic melt, whereas average crust shallower than 20 km has a density similar to, or less than, that of the basaltic melt. Dense magmas can ascend through less dense rocks if connected to sufficiently high-pressure regions at depth, but small batches of ascending magma would tend to slow or stall upon reaching their level of neutral buoyancy, passing from the lower to the upper crust, where they would then cool, crystallize, and differentiate. The continental crust is heterogeneous, but direct estimates of local crustal density that are based on gravity and shear velocity measurements give relations similar to the average continental density-depth curve. Lower crustal densities are estimated as 3.12 and 2.88 g/cm^3 immediately west and east of the volcanic field and 2.76 g/cm^3 beneath the field's axis; for the upper crust, estimates are 2.73 to 2.70 g/cm^3 (Langenheim and others, 2019, 2023). Therefore, basaltic melts would be neutrally to positively buoyant in the lower crust but neutrally buoyant to negatively buoyant relative to the upper crust, promoting midcrustal stagnation and differentiation. The transitions in seismic velocity and crustal density are relatively sharp, yielding a well-defined Conrad discontinuity near 20 km depth.

Magmatic Differentiation—Further Insights from Trace Elements

Bulk solid-to-melt partition coefficients, defined as a trace element's weight concentration in the mineral assemblage divided by its weight concentration in the melt, can be estimated for basalt-to-hawaiite differentiation at northern Harrat Rahat. Results support crystallization-differentiation of dominantly gabbroic assemblages, which are divisible into successive stages that initially lack, then include, titanomagnetite. Apparent partition-coefficient values for the bulk crystallizing assemblages (D_x) can be estimated from the equation for fractional (or Rayleigh) crystallization (eq. 3),

$$\frac{C_l}{C_o} = F^{D_x - 1}, \quad (3)$$

where

C_o is the trace element's concentration in the liquid at the start of a crystallization interval;

C_l is its concentration at the interval's end;

F is the mass fraction of liquid remaining (implicit is that F=1 at C_o, the start of the interval); and

D_x is the bulk solid-liquid partition coefficient of a specific trace element (x).

Apparent partition-coefficient values were derived using the fractional crystallization equation to match concentration trends of Harrat Rahat basalts and hawaiites on plots of Th versus other trace elements, having first assigned highly incompatible Th (Blundy and Wood, 2003) a D_{Th} value of 0.015 and then trial-and-error adjusting the D values for the other trace elements to reproduce the rock-compositional arrays. Derivations were performed separately for the MgO concentration intervals of 9.0 to 6.75 weight percent and 6.0 to 4.0 weight percent to represent the early decreasing- and subsequent increasing-SiO_2 differentiation stages, having excluded samples that have P_2O_5/K_2O values >0.8 to minimize the influence of selective assimilation of apatite. Raising or lowering the value assigned to D_{Th} has the effect of shifting the apparent bulk D values for the other trace elements either toward or away from, respectively, unity, the greatest influences being on the most incompatible and compatible elements.

Apparent partitioning values for the two differentiation intervals (table 5) are plotted in figure 13, elements being arranged, from left to right, in the general order of increase for calcic clinopyroxene+olivine assemblages. This sequence (Sun and McDonough, 1989) derives mainly from increasing primitive-mantle-normalized concentrations in MORB that reflect low to moderate extents of partial melting of lherzolite (olivine>orthopyroxene>calcic clinopyroxene≥plagioclase, spinel, or garnet). Both differentiation intervals show an overall increase, from left to right, in D values, and a D value of >1 for Sc, consistent with appreciable calcic clinopyroxene in the crystallizing assemblage. In the magnesian-differentiation interval, the D value for Sr is slightly high relative to adjacent values for Nd and Zr, consistent with early crystallization of plagioclase. The more evolved differentiation interval is distinguished by Sr, Ti, and V having become moderately to strongly compatible, consistent with a greater proportion of plagioclase or more sodic plagioclase (Blundy and Wood, 1991) having raised D_{Sr} values, as well as with titanomagnetite having joined the crystallizing assemblage, raising D_{Ti} and D_V values. Values for D_{Nb} and D_{Ta} are also greater in the evolved interval, consistent with those elements partitioning into titanomagnetite preferentially. Notable are (1) the absence of a positive partitioning anomaly for Eu in the magnesian-crystallization interval, and (2) the small size of the positive Eu anomaly in the subsequent evolved interval, despite major-oxide and trace-element evidence for the presence of plagioclase in the crystallizing assemblages. Small to absent positive Eu partitioning anomalies may be due to a high proportion of calcic clinopyroxene to plagioclase, such that the low D value of clinopyroxene for Eu^{2+} counterbalances its high D value in plagioclase (Philpotts, 1970), as well as possibly to the relatively high fO_2 that lowers D_{Eu} in plagioclase (Philpotts, 1970). A synthesis of experimental results by Dygert and others (2020) yielded $D_{Eu}/D_{Eu^{3+}}$ ratio estimates of 2.4 to 1.5 at 1,250 °C and 24 to 9.5 at 1,100 °C for An_{60} at fO_2 of QFM to QFM+2, showing that higher temperatures and higher oxidation states greatly reduce the preferential uptake of Eu in plagioclase.

Table 5. Apparent bulk trace-element partition-coefficient (*D*) values for gabbroic differentiation of Quaternary basalts through hawaiites of northern Harrat Rahat.

[MgO interval, in weight percent (wt. %), gives concentration range of rocks used to derive partition-coefficient values; Th - fixed is Th partition-coefficient value, which is fixed at 0.015 to derive other values]

Element	MgO intervals (wt. %)	
	9–6.75	6–4
Rb	<0.001	<0.001
K	0.09	0.10
Ba	0.04	0.03
Sr	0.50	1.05
Y	0.76	0.42
Ti	0.50	1.3
Th - fixed	0.015	0.015
U	0.03	0.01
Zr	0.50	0.30
Hf	0.55	0.35
Nb	0.02	0.06
Ta	0.05	0.12
La	0.14	0.10
Ce	0.20	0.12
Pr	0.30	0.20
Nd	0.35	0.23
Sm	0.45	0.25

Element	MgO intervals (wt. %)	
	9–6.75	6–4
Eu	0.52	0.40
Gd	0.60	0.35
Tb	0.66	0.35
Dy	0.72	0.35
Ho	0.76	0.43
Er	0.78	0.40
Tm	0.79	0.40
Yb	0.79	0.45
Lu	0.80	0.50
V	0.90	1.9
Sc	1.25	1.5
Cr	2.3	6
Ni	1.7	3
Cu	1.6	2
Pb	0.28	0.14
Zn	0.92	0.70
Ga	0.92	0.90

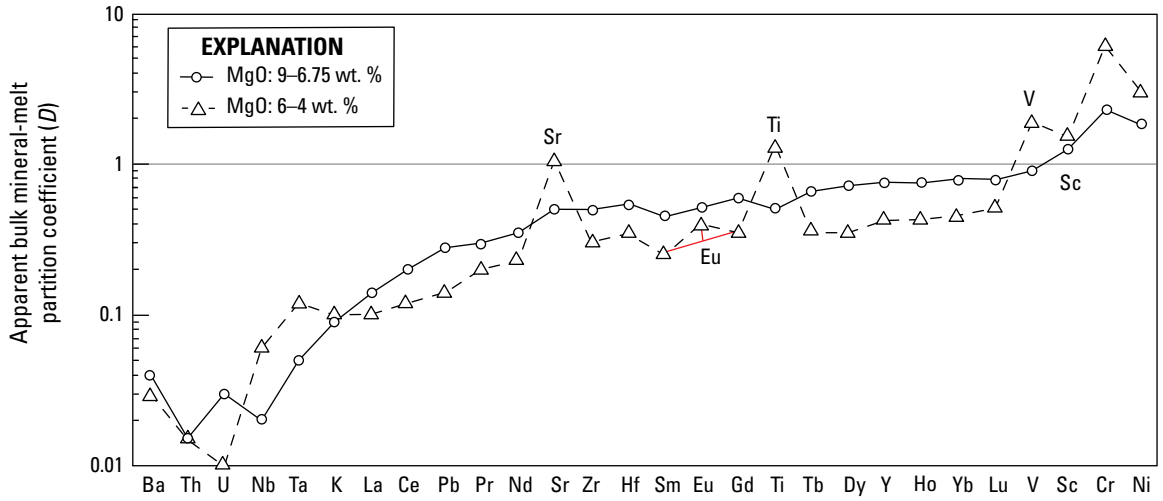

Figure 13. Plot of apparent bulk mineral-melt partition coefficients (*D*) for decreasing- and increasing-SiO_2 stages of gabbroic differentiation (see table 5) estimated for northern Harrat Rahat basalts and hawaiites that have MgO concentrations between 9 and 6.75 weight percent and between 6 and 4 weight percent, respectively. Solid red lines show the positive Eu partitioning anomaly relative to Sm and Gd. Horizontal line at *D* = 1 divides incompatible from compatible elements.

Mantle-Source Depths, Temperatures, and Mineral Assemblages Interpreted from Major-Oxide Compositions

Processes driving northern Harrat Rahat magmatism can be inferred, in part, from estimates of the conditions in the mantle source undergoing melting. Source temperatures calculated as appreciably hotter than ambient asthenosphere could signal contributions from a plume upwelling from deeper parts of the mantle, whereas temperatures similar to those of ambient asthenosphere could indicate decompression melting of the asthenosphere that either is driven by lithospheric thinning or perhaps is due to localized upwelling during ordinary, thermally driven convection.

Melting depths, phase assemblages, and temperatures can be evaluated with recent experimental studies that parameterize the compositions of melts in equilibrium with plagioclase-, spinel-, and garnet-lherzolites (Till and others, 2012; Grove and others, 2013). Figure 14 shows least fractionated (Mg# >64) alkali and transitional basalts from northern Harrat Rahat (Downs, 2019), recast into mineral components (Grove, 1993) and projected from the olivine component into the plagioclase–Ca-clinopyroxene–quartz pseudoternary and from the plagioclase component into the olivine–Ca-clinopyroxene–quartz pseudoternary. Also shown are melt compositions predicted to be in equilibrium with plagioclase-, spinel-, and garnet-lherzolites, calculated with compositional characteristics appropriate for northern Harrat Rahat and distinguished by their pressures of equilibration (Till and others, 2012; Grove and others, 2013). Propagated one-standard-deviation uncertainty limits for spinel-lherzolite partial melts are plotted as dashed lines subparallel to the spinel-lherzolite melting array. Uncertainty windows for plagioclase- and garnet-lherzolite melts are similarly parallel to their respective arrays but are omitted for clarity.

In both projections, the least fractionated alkali basalts overlap the compositions of spinel-lherzolite partial melts broadly in the range of 1.6 to 2.0 gigapascals (GPa), but they define fields displaced from those primary liquids in directions consistent with having fractionated small amounts of olivine, plagioclase, or both. Part of the field of least fractionated alkali basalts plots on the olivine- and plagioclase-enriched sides of the spinel-lherzolite melt array, consistent with modest olivine and plagioclase accumulation in some samples. Transitional basalts of northern Harrat Rahat have greater quartz components, consistent with having segregated shallower in the spinel-peridotite field and then having undergone similar olivine or olivine+plagioclase fractionation. The median alkali basalt with Mg# >64 (table 1; see also, fig. 14) can be brought into coincidence with the array of spinel-peridotite partial melts by addition of 7 weight percent plagioclase ($An_{65.6}$) present as early phenocrysts in northern Harrat Rahat basalts (Camp and others, 1987) and 7 to 8 weight percent equilibrium-composition olivine, incrementally calculated and added. This possible parental-magma composition (model 1, in table 6; see also, fig. 14) is similar to spinel-lherzolite melts that segregated from their sources at pressures of about 1.8 to 2.0 GPa. Application of the experimentally calibrated model of Till and others (2012) to this reconstructed parental-magma composition yields temperatures at those pressures of 1,380 to 1,405 °C.

A possible shortcoming of this parental-magma estimate is that reverse fractionation of 7 to 8 weight percent olivine, with or without plagioclase, commencing with the median least fractionated alkali basalt composition (table 1) and with Fe^{3+}/total Fe ratio initially specified to be appropriate for QFM (0.15 molar), predicts a relatively iron rich olivine (Mg#, 88.7–89.0) in the mantle source upon melt segregation. Reverse fractionations of about 20 weight percent olivine (model 2, in table 6) would be required to attain olivine that has Mg# of 90, as is sought by other approaches for estimating parental-magma compositions (Herzberg and Asimow, 2008, 2015; Lee and others, 2009). This disparity is reduced by increasing the Fe^{3+}/total Fe ratio of the melt composition at the beginning of reverse fractionation or by decreasing the Mg# of the target olivine, or both. Wilshire and others (1988) reported

Figure 14. Parts of ternary diagrams showing range of compositions of least fractionated alkali basalts (dark-gray shading) and transitional basalts (pink shading) of northern Harrat Rahat compared with calculated compositions of partial melts of plagioclase-, spinel-, and garnet-lherzolites (Till and others, 2012; Grove and others, 2013), at upper mantle pressures (in gigapascals [GPa]) shown by squares, circles, and cross-ticks. Rock and melt compositions are recast into equal-oxygen mineral components (following method of Grove, 1993) and are projected (*A*) from olivine (Oliv) component, into part of plagioclase (Plag)–calcic clinopyroxene (Cpx)–quartz (Qtz) ternary diagram, and (*B*) from plagioclase component, into part of calcic clinopyroxene–olivine–quartz ternary diagram; proportions of projected components given in normalized percent. Red diamond shows composition of median alkali basalt (MAB) that has Mg# greater than 64 (see table 1); blue, yellow, and green triangles show effects on that composition of reversing small to moderate extents of crystal fractionation of olivine and also of olivine+plagioclase (see table 6). Dashed lines on either side of spinel-lherzolite partial-melting curve in both projections show propagated 1-sigma (σ) uncertainties. Other abbreviations: Mg#, Mg number (=100×Mg/[Mg+Fe^{2+}], molar) ; %, percent.

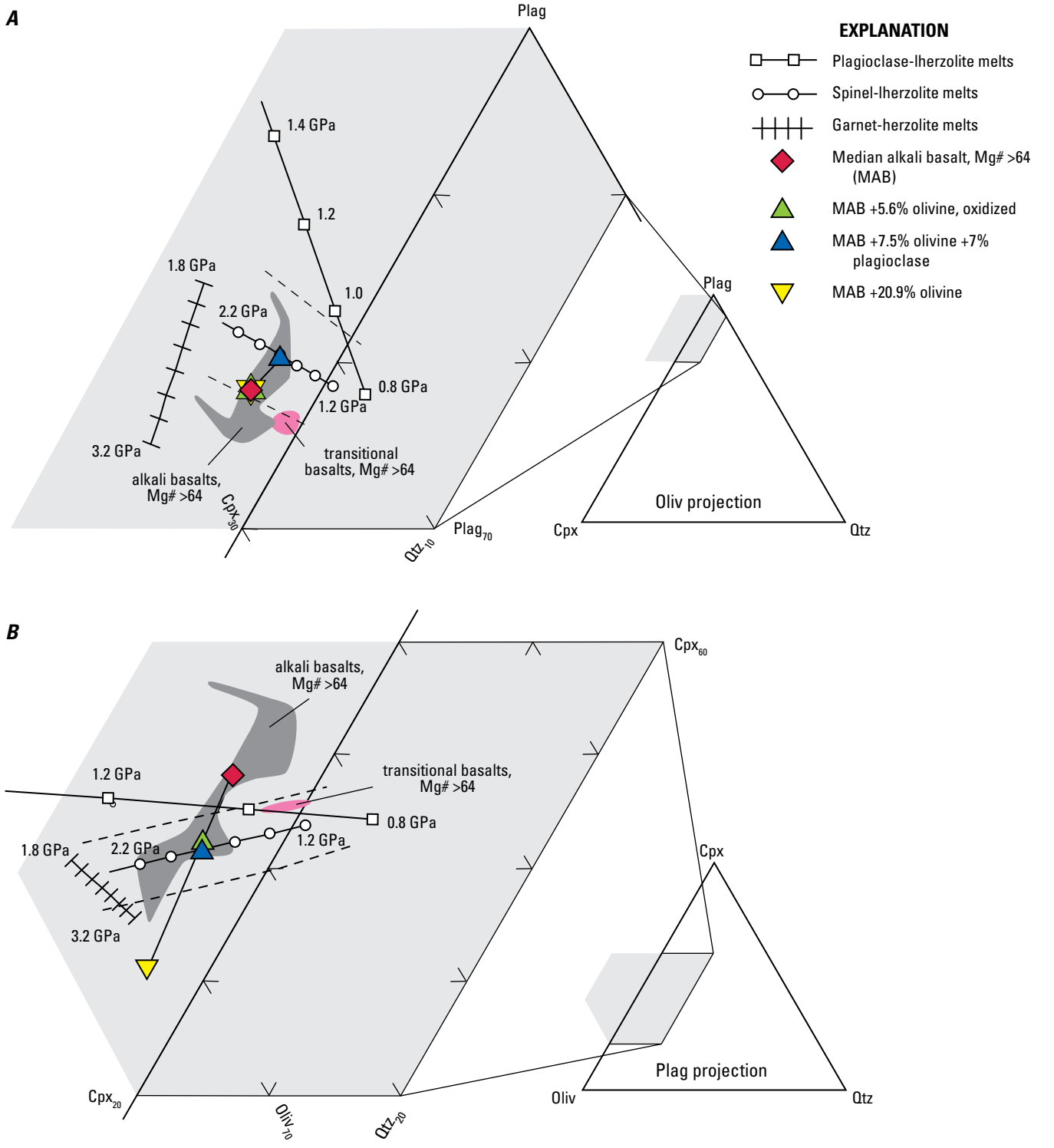
A
Plag
1.4 GPa
1.2
1.0
0.8 GPa
1.2 GPa
2.2 GPa
1.8 GPa
3.2 GPa
alkali basalts, Mg# >64
transitional basalts, Mg# >64
Cpx30
Qtz10
Plag70
Plag
Oliv projection
Cpx
Qtz
EXPLANATION
Plagioclase-lherzolite melts
Spinel-lherzolite melts
Garnet-herzolite melts
Median alkali basalt, Mg# >64 (MAB)
MAB +5.6% olivine, oxidized
MAB +7.5% olivine +7% plagioclase
MAB +20.9% olivine
B
Cpx60
alkali basalts, Mg# >64
transitional basalts, Mg# >64
1.2 GPa
0.8 GPa
1.8 GPa
2.2 GPa
1.2 GPa
3.2 GPa
Cpx
Plag projection
Cpx20
Oliv70
Qtz20
Oliv
Qtz

Table 6. Potential primary-magma compositions and source conditions for Quaternary basalts of northern Harrat Rahat.

[Compositions in weight percent (wt. %). Models 1 and 3 are from spinel-lherzolite melting relations of Till and others (2012); model 2 is simple olivine addition to Fo_{90} (from Lee and others, 2009), where forsterite (Fo) is mole percent forsterite specified for source olivine; +plag% and +oliv% are mass percentages of plagioclase (plag) and olivine (oliv) added to reach parent magma composition. Other abbreviations: *P*, pressure, in gigapascals (GPa); *T*, temperature, in degrees Celsius (°C)]

Model	SiO_2	TiO_2	Al_2O_3	Fe_2O_3	FeO	MnO	MgO	CaO	Na_2O	K_2O	P_2O_5	*T* (°C)	*P* (GPa)	Fo	+plag%	+oliv%
1	46.7	1.36	15.6	1.57	9.00	0.17	12.3	10.4	2.56	0.28	0.15	1,380–1,405	1.8–2.0	88.9	7	7.5
2	45.7	1.30	13.1	0.51	10.8	0.14	16.8	9.10	2.21	0.26	0.14	1,500	2.8	90.0	0	20.9
3	46.4	1.49	14.9	2.47	8.88	0.16	12.3	10.4	2.53	0.29	0.16	1,360	1.7	88.9	0	5.6

that in the widespread, refractory, Cr-diopside-suite peridotite xenoliths erupted across western North America, olivine has an average Mg# of 88.9. By employing this as the target olivine composition, and commencing reverse fractionation at the higher Fe^{3+}/total Fe ratio value (QFM+1; 0.21 molar) (estimated from modeling basalt to hawaiite crystallization-differentiation; see table 3), only 5 to 6 weight percent reverse fractionation is required to achieve olivine that has Mg# of 88.9; the resulting estimated parent melt corresponds closely with the spinel-lherzolite partial melting array (see fig. 14).

Another disparity to address is that the geochemistry of the northern Harrat Rahat basalt-to-hawaiite suite indicates that primitive magmas underwent an early stage of differentiation dominated by olivine and subordinate or no accompanying plagioclase, whereas the closest match to lherzolite-saturated primary liquids involves addition of both olivine and plagioclase. However, the uncertainty envelopes for compositions of spinel-lherzolite partial melts are sufficiently broad (fig. 14) that little preference can be assigned to early crystallization of olivine+plagioclase versus solely of olivine to account for the earliest stages of fractionation of northern Harrat Rahat magmas.

In combination, consistent results are obtained that the parental magmas of northern Harrat Rahat segregated from lherzolite sources in the middle to lower parts of the spinel-peridotite facies (at pressures of 1.6 to 2.0 GPa, but mostly 1.8 to 2.0 GPa, and at temperatures from the high 1,300s to the lowest 1,400s °C), with parents of transitional basalts having segregated at shallower depths than did parents of alkali basalts. The least fractionated magmas to reach the surface were products of roughly 5 to 10 weight percent of olivine-dominated crystallization-differentiation. For a 40-km-thick continental crust that has a typical average density of 2.78 g/cm^3 (Christensen and Mooney, 1995) and a mantle density of 3.31 g/cm^3, segregation pressures of 1.8 to 2.0 GPa correspond to depths of 62 to 68 km, which is similar to the 65 to 85 km depth of the lithosphere-asthenosphere boundary, identified by seismic methods (Yao and others, 2017), beneath the axis of the largest volcanic fields in western Saudi Arabia. Agreement of these depth estimates supports the interpretation that parental magmas segregated where upwelling peridotite impinged on the base of the lithosphere. It is worth noting that Duncan and Al-Amri (2013) inferred similar mantle-segregation depths for the more alkaline mafic lavas of Harrat Lunayyir (located near the Red Sea, 220 km northwest of northern Harrat Rahat; see fig. 1 for location), but they inferred depths of only 15 to 40 km (0.5–1.2 GPa) for Harrat Rahat magmas, which would place their mantle segregation in the middle and lower crust. The Duncan and Al-Amri (2013) estimates were predicated on a trace element-enriched source composition similar to that of the Iceland mantle plume, whereas the following discussion indicates that the Arabian harrats derived from sources more similar to ordinary depleted upper mantle asthenosphere.

Potential Temperature of the Mantle Source of Harrat Rahat

The asthenospheric mantle sources for oceanic spreading-ridge basalts (MORB) are commonly inferred to have mantle potential temperatures[5] in the range of 1,350 to 1,410 °C (Sarafian and others, 2017). Projecting along an isentropic adiabat for (metastable) melt-free peridotite (about –0.5 °C per kilometer of ascent; Turcotte and Schubert, 2002) gives asthenosphere temperatures of 1,380 to 1,440 °C at 1.8 to 2.0 GPa, similar to the values derived for the source of northern Harrat Rahat alkali basalts (models 1 and 3, in table 6). Partial melting would have reduced the temperature of the northern Harrat Rahat source, owing to the latent heat of fusion of crystals, but this effect is small for small degrees of melting. Using an approximate heat capacity for solids and melt of 1.25 joules per gram per degree kelvin (J/g·K) and a latent heat of fusion of 600 joules per gram (J/g) (from pMELTS simulations of low-degree melting of depleted peridotite and similar to values in Ganguly [2005] and references therein) yields cooling of roughly 5 °C per 1 weight percent decompression melting, valid at low melt fractions. Trace-element considerations (see subsequent section) indicate that about 3 weight percent melting yielded the parental magmas to common northern Harrat Rahat alkali

[5]Mantle potential temperature is the theoretical temperature of a mantle domain if decompressed to the Earth's surface pressure by adiabatic isentropic ascent without having partially melted (McKenzie and Bickle, 1988).

basalts, so reversing the thermal effect of melting would raise estimated source temperatures by only about 15 °C to 1,375 to 1,420 °C from the model 1 and 3 values (table 6). Projecting to the surface along a melt-free isentropic adiabat from about 1.8 to 2.0 GPa then gives mantle potential temperatures for northern Harrat Rahat of between 1,345 and 1,390 °C. The narrow range of estimated potential temperatures does not incorporate uncertainties in its derivation, but it can be concluded that evidence is lacking that northern Harrat Rahat magmas originated from sources appreciably hotter than those that yield MORB beneath developed spreading ridges. This interpretation is contingent, however, on the northern Harrat Rahat melts having separated from peridotite sources that have olivine slightly poorer in Mg, or as melts that have slightly higher Fe^{3+}/total Fe ratios, than are commonly posited for MORB melting.

Mantle-Source Trace-Element Abundances and Solid-Melt Partitioning

The causes and conditions of magmatism in northern Harrat Rahat and, by association, regionally across the Arabia Plate are illuminated by estimates of the trace-element composition and mineral-melt partitioning behavior of the mantle source undergoing melting. Source trace-element concentrations and bulk partition coefficients during partial melting were estimated using the approach of Minster and Allègre (1978), which entails regressing arrays of the inverse concentrations of trace elements of a cogenetic magmatic suite against the inverse concentrations of a highly incompatible trace element. The equation for batch partial melting is such that the slopes and intercepts of such arrays can be used to estimate the trace-element concentrations and bulk solid/liquid partition coefficients of the source, so long as one trace element's concentration in the source is specified. Actual melting is likely to have been dynamic and near-fractional (Salters and others, 2023), but Hart and others (1997) showed that inaccuracies are small for incompatible trace elements applying the Minster and Allègre (1978) batch-melting approximation to accumulated fractional melts.

Strictly, the inversion method applies to suites of primitive melt compositions, so derived values are more accurate if subsequent effects of crystallization-differentiation are reversed. Prior to applying the Minster and Allègre (1978) method, the effects of gabbroic crystallization-differentiation were reversed using the fractional (Rayleigh) crystallization equation (eq. 3; see above), solving for the prefractionation concentrations of a trace element (C_o), where C_l is its measured concentration in a sample, D_x is the bulk solid-liquid partition coefficient deduced for the crustal-level, higher MgO gabbroic crystallization interval (table 5), and F is the mass fraction of differentiated residual melt that the sample represents. Mass fractions of residual melt (F values) were estimated by assuming an initial Mg# of 65 and treating the Mg# as though it were a trace element that has a D value of 1.17, which, using the fractional-crystallization equation (eq. 3) and D values of table 5, yields trends that closely match the sample suite on plots of trace-element concentrations versus Mg#. Other approaches were also explored for estimating F values, such as adding the estimated early gabbroic cumulate (table 3) to arrive at a common initial MgO concentration, but those methods proved to be inferior, as shown by correlations between apparent F values and adjusted trace-element concentrations. Excluded from consideration were rocks that have MgO concentrations <6.8 weight percent and P_2O_5/K_2O values >0.8 to avoid the need for large or multiple reverse-fractionation steps and to exclude compositions affected by apatite accumulation or assimilation. Incompatible trace-element concentrations of basalts so adjusted to Mg# of 65 were then reduced uniformly by a further 10 percent to reverse the potential effects of the early olivine-dominated fractionation stage. Harrat Rahat basalt compositions with Mg# greater than 65 mostly fall on olivine or olivine+plagioclase control lines, and the trace-element concentrations of such high-MgO samples were not adjusted for gabbroic differentiation. A total of 188 so-adjusted mafic rock compositions were employed to estimate the mantle source composition and melting characteristics for northern Harrat Rahat.

Source compositions and bulk partition coefficients during mantle-level partial melting were then derived using the Minster and Allègre (1978) approach as the uncertainty-weighted average of results, using 1/La, 1/Ta, and 1/Th as the reference inverse highly incompatible trace elements and fixing the concentration of Dy in the source to that estimated for the average depleted-mantle source for MORB (0.505 parts per million by weight [ppm]; Workman and Hart, 2005). Regressions were performed using the method of York (1969), assigning uncertainties to ordinate and abscissa values as 2.5 percent of the concentration of the particular element plus 10 percent of the lowest concentration for that element in the suite. For some trace elements, the Minster and Allègre (1978) approach can derive physically impossible, slightly negative D values. This shortcoming was addressed by increasing the model D value for the reference highly incompatible trace element from zero by increments of 0.0005 until the D values for all other elements became positive. Resulting slope and intercept values and uncertainties were propagated through to concentrations and D values; reported results (table 7; fig. 15) are the uncertainty-weighted averages and standard deviations of the 1/La, 1/Ta, and 1/Th models. Regression correlations were weak for certain heavy REE (Tm, Yb, Lu) and for Sr; for Tm, Yb, and Lu, this is probably because melting spans the garnet to spinel stability fields, leading to appreciably changing D values for the heavy REE; for Sr, it is possibly because variable amounts of plagioclase crystallize at different depths in the crust, introducing scatter in reverse-fractionated Sr concentrations. Accordingly, source concentration values for Tm, Yb, and Lu were assigned those for average DM (Workman and Hart, 2005), and D values were then calculated

Table 7. Mantle source and average primitive-magma trace-element concentrations (*C*) and bulk partition-coefficient (*D*) values derived for basalts of northern Harrat Rahat and for basalts of the Gulf of Aden.

[C_{MS} and D_{MS} are weighted average solutions for concentrations (C), in parts per million (ppm), and solid-melt partition-coefficient (D) values, respectively, of mantle source that melted to produce basalts of northern Harrat Rahat, derived following method of Minster and Allègre (1978) after reversing crustal differentiation; +/– is weighted standard deviation of solutions regressing versus 1/Th, 1/Ta, and 1/La ratios; r is average correlation coefficient for regressions; C_{PM} is concentration in average Harrat Rahat parent magma derived by reversing crustal differentiation; C_{AD6} and C_{AD10} are possible Gulf of Aden mantle source compositions, assuming averages of 6 and 10 weight percent partial melting, respectively. Other abbreviation: ND, not determined]

Element	Northern Harrat Rahat						Gulf of Aden	
	C_{MS} (ppm)	+/–	D_{MS}	+/–	r	C_{PM} (ppm)	C_{AD6} (ppm)	C_{AD10} (ppm)
Rb	0.045	0.002	0.0007	0.0003	0.80	1.9	0.17	0.28
Ba	0.85	0.04	0.0008	0.0003	0.73	37.0	2.4	4.0
Th	0.010	0.001	0.0030	0.0004	0.91	0.39	0.03	0.05
U	0.0030	0.0002	0.0016	0.0005	0.78	0.13	0.009	0.014
Nb	0.15	0.01	0.0033	0.0004	0.91	5.70	0.56	0.91
Ta	0.011	0.001	0.0036	0.0005	0.86	0.41	0.036	0.057
K	66	5	0.0070	0.0008	0.91	2,200	73	121
La	0.21	0.02	0.010	0.001	0.85	6.38	0.41	0.65
Ce	0.58	0.04	0.014	0.002	0.87	15.9	1.13	1.68
Pb	0.017	0.001	0.0047	0.0008	0.66	0.62	0.03	0.05
Pr	0.097	0.006	0.019	0.002	0.82	2.35	0.17	0.24
Nd	0.51	0.03	0.025	0.002	0.80	10.8	0.80	1.15
Sr	[1]17.9	ND	[2]0.031	ND	<0.45	290	8.7	12.8
Sm	0.18	0.01	0.039	0.002	0.77	2.93	0.28	0.38
Eu	0.090	0.002	0.057	0.001	0.72	1.14	0.10	0.14
Gd	0.303	0.005	0.065	0.001	0.69	3.45	0.38	0.51
Zr	4.6	0.2	0.017	0.002	0.80	100	6.8	9.8
Hf	0.131	0.006	0.026	0.002	0.81	2.38	0.19	0.27
Tb	0.064	0.001	0.086	0.001	0.64	0.59	0.08	0.10
Dy	[2]0.505	ND	0.108	0.004	0.56	3.72	0.54	0.69
Ho	0.113	0.001	0.130	0.001	0.49	0.74	0.12	0.15
Er	0.312	0.005	0.140	0.002	0.45	1.93	0.38	0.47
Tm	[2]0.055	ND	[1]0.18	ND	<0.45	0.27	ND	ND
Yb	[2]0.365	ND	[1]0.20	ND	<0.45	1.59	0.40	0.48
Lu	[2]0.058	ND	[1]0.21	ND	<0.45	0.24	0.06	0.07

[1]Values are derived from assumed C_{MS} or D_{MS} values, as in text, and so uncertainties are not presented.

[2]Values are assumed, as in text.

from the average fractionation-corrected primitive-magma composition of northern Harrat Rahat (table 7) at the average 3.1 weight percent degree of partial melting (discussed following). For Sr, the D value was set to the geometric mean of the D values for Nd and Sm, on the basis of the similar mantle incompatibility of those elements. The Sr concentration of the source was then calculated from the average primitive Harrat Rahat basalt at the average extent of melting.

The conspicuous and important result of these calculations (fig. 15) is that the mantle source for basalts of northern Harrat Rahat is inferred to have had trace-element abundances that are closely similar to those of the average depleted-mantle source for MORB (Salters and Stracke, 2004; Workman and Hart, 2005), differing chiefly in a positive-concentration anomaly for Sr (discussed following). The simplest interpretation of this is that volcanism originated by melting predominantly of depleted

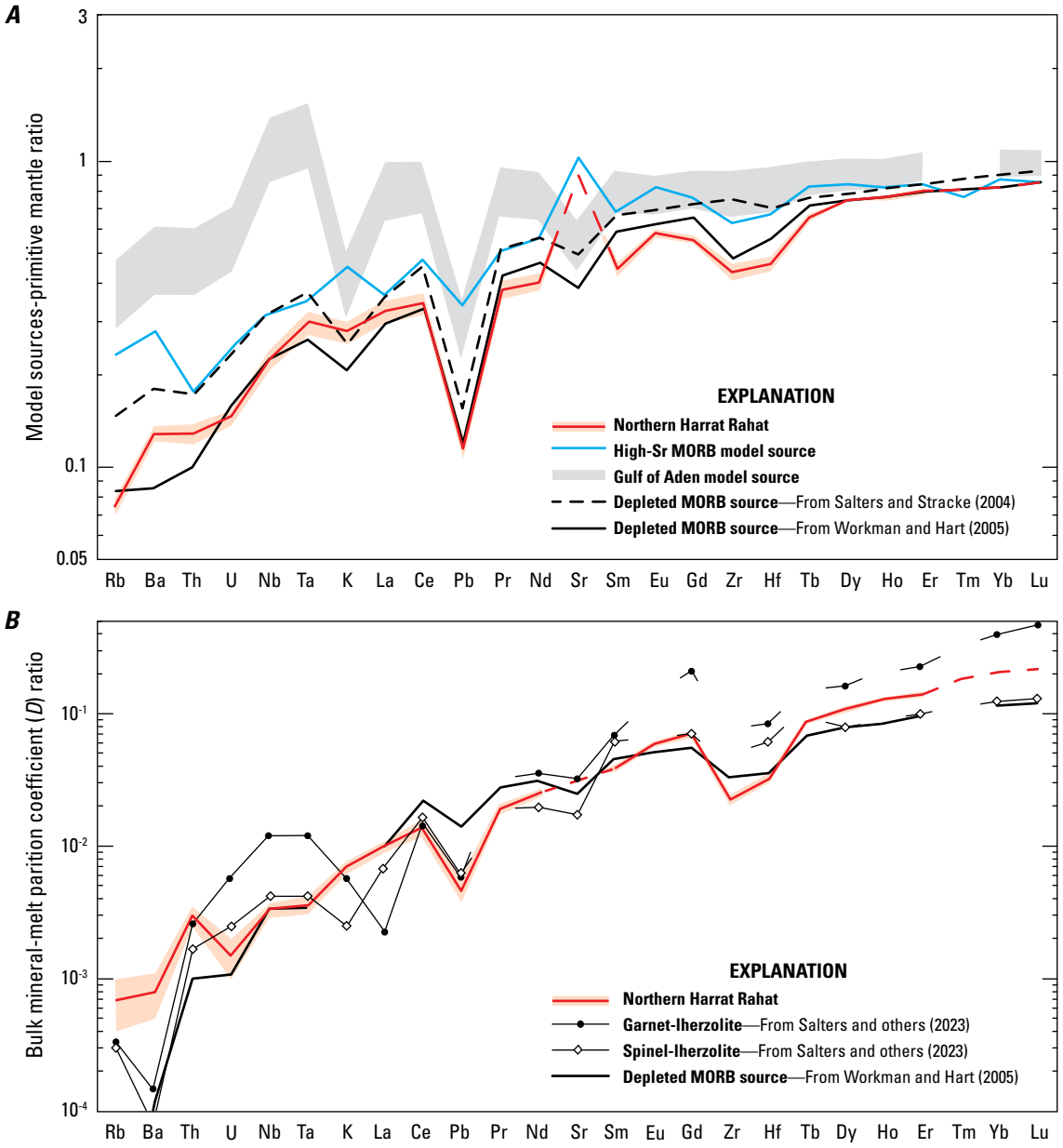

Figure 15. Plots showing (*A*) mantle-source trace-element concentrations (*B*) and bulk mineral-melt partition coefficients derived for basalts of northern Harrat Rahat. Solid red line shows values estimated using method of Minster and Allègre (1978), and orange shading shows 1-sigma (σ) uncertainties (see table 7); dashed red line shows where estimated using other methods (as discussed in text). Gray-shaded field in *A* shows range of solutions for mantle source for Gulf of Aden oceanic spreading-ridge basalts influenced by Afar mantle plume, assuming 6 to 10 percent partial melting (gap in shading shows that Er and Tm concentrations are not available). Other colored and patterned lines show concentrations and partition-coefficient estimates for global midocean ridge basalts (MORB)–source depleted mantle (from Salters and Stracke, 2004; Workman and Hart, 2005), those having selected high-Sr/Nd ratios, and estimated partition coefficients (*D*) at onset of garnet- and spinel-lherzolite partial melting used in partial-melting calculations of Salters and others (2023); gaps in lines connecting *D* values show that Salters and others (2023) did not present *D* values for all plotted elements. Concentrations are normalized to primitive silicate mantle values from Sun and McDonough (1989).

asthenosphere with, at most, minor enrichments in exotic components, rather than mainly of a deep-sourced mantle plume or of subcontinental lithospheric upper mantle, the compositions of which can be expected to differ from MORB-source mantle. Radiogenic-isotope values of basalts of northern Harrat Rahat are shifted modestly from those of average MORB (Moufti and others, 2012; Salters and others, 2023), consistent with a predominantly, although not exclusively, ordinary-MORB source.

The derived bulk solid-melt partition coefficients (fig. 15) are also closely similar to those inferred for the depleted MORB source, differing in that the source for northern Harrat Rahat has apparent D values that are moderately higher for the most incompatible elements (Rb, Ba) and for certain heavy REE (Tm, Yb, Lu), the latter being intermediate between values determined independently (Salters and others, 2023) for melting in the spinel- and garnet-peridotite stability fields.[6] MORB are widely accepted as having amalgamated melts from the garnet- and spinel-peridotite stability fields (Salters and Hart, 1989), and the greater D values for certain heavy REE (Tm, Yb, Lu) for northern Harrat Rahat are evidence for a greater relative proportion of melt originating from the garnet-peridotite facies owing to the melting column having arrested at roughly 65 km upon encountering the base of the continental lithosphere.

Degrees of Melting

Approximate degrees of melting can be estimated for basalts of northern Harrat Rahat using the trace-element concentrations and D values derived for their mantle source (table 7). Melt-fraction estimates are solutions for F of the batch partial melting equation (eq. 4),

$$\frac{C_l}{C_o^s} = \frac{1}{D_x(1-F)+F}, \tag{4}$$

where

C_o^s is the concentration for element x in the fully solid source (s) at the onset of melting;

C_l is that element's concentration, as calculated by reverse-fractionation for each basalt used to arrive at the mantle source composition;

D_x is the bulk solid-liquid partition coefficient for element x in the source at the onset of melting; and

F is the mass fraction of melting to produce a melt with concentration C_l of element x.

[6]Note that an unexpected and presently unexplained result is that the ratio of D values for Th versus U is >1, whereas that ratio value is understood to be ≤1 during melting of garnet- and spinel-peridotites (Lundstrom, 2003; Bourdon and Sims, 2003).

By analogy with MORB, the actual melting process is likely to have been fractional, with erupted magmas representing pooled mixtures of differing degrees of fusion; however, the equations for batch melting and pooled fractional melting yield closely similar values for average melt fraction (Shaw 1970, 1979). Estimates for F were derived for each reverse-fractionated basalt for Rb, K, Ba, La, Ta, Th, and U. Each element yields a moderately different estimate of melt fraction for each sample; figure 16 summarizes the averages derived from those elements for all samples. The average degree of melting for northern Harrat Rahat basalts is estimated as 3.1 weight percent, with alkali basalts spanning from 1.3 to 5.6 weight percent and transitional basalts from 2.6 to 5.3 weight percent. Most compositions, however, fall in the narrow range of 2 to 4 weight percent partial melting. For comparison, some recent estimates for the average degree of melting to yield MORB are 6 weight percent (Workman and Hart, 2005) or 8 to 10 weight percent (Salters and Stacke, 2004), roughly 2 to 3 times greater than the predominant extents of melting estimated for northern Harrat Rahat, consistent with the harrat's melting column having arrested at greater depth upon encountering the base of the continental lithosphere. Duncan and Al-Amri (2013) inferred higher degrees of melting (10 to 15 weight percent) for Harrat Rahat magmas, but, as with depths, their approach relied on an Iceland plume source trace-element composition that is inconsistent with the results of this study.

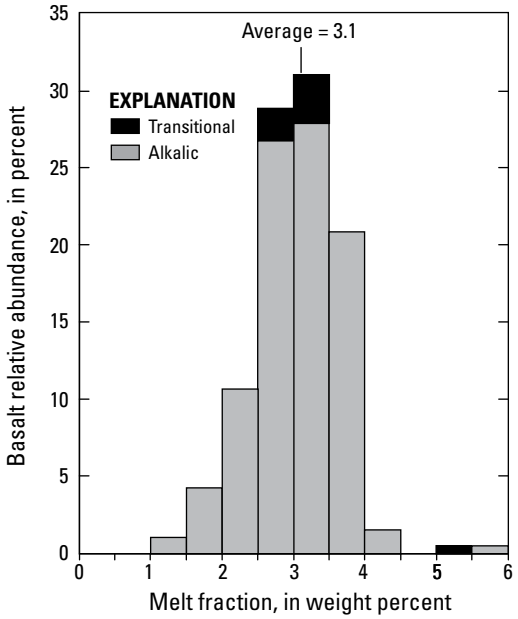

Figure 16. Histogram of degrees of batch partial melting calculated to produce alkali and transitional basalts of northern Harrat Rahat, reverse-fractionated to primitive compositions.

Exotic Components in Northern Harrat Rahat's Mantle Source

The major mantle plume of the Africa-Arabia region impinged on the base of the lithosphere below what is now the Afar depression leading to (1) modest uplift and exhumation in the Late Cretaceous or Paleocene, then (2) flood-basaltic volcanism in the early Oligocene, and subsequently (3) diminishing volcanism, continued uplift, and extensive rifting (see, for example, Gass, 1970; Coleman, 1993; Sembroni and others, 2016). Plume material spread in uncertain amounts and to uncertain distances beneath northern African and possibly Arabian lithosphere (Ebinger and Sleep, 1988). Basalts of the northern East African Rift and the Afar depression would, therefore, be expected to carry a clear plume chemical and isotopic imprint, but detailed studies infer that most basalts of that region had complex sources, interpreted as combinations of asthenospheric upper mantle, mantle lithosphere, and possibly multiple plume components (Rodgers and others, 2000; Furman and others, 2006). Simpler, owing to the absence of subcontinental lithospheric upper mantle, are oceanic spreading-ridge basalts (MORB) of the Gulf of Aden (fig. 1) that have been interpreted on geochemical and isotopic grounds as deriving from depleted asthenosphere mixed with material from the Afar plume (Rooney and others, 2012; Kelley and others, 2013).

For purposes of comparison, simple estimates were made of the trace-element concentrations of the Afar-plume-influenced source for submarine basalts of the Gulf of Aden spreading system and its on-land extension to the Asal Rift of the Afar depression. Model source concentrations were derived from median concentrations of moderately and strongly incompatible elements of those basalts (Kelley and others, 2013), reduced by 20 percent to reverse the probable effects of subsequent crystallization-differentiation. Then, source concentrations were calculated assuming 6 and 10 weight percent batch partial melting, using the *D* values of Workman and Hart (2005) that are appropriate for peridotite melting to shallow depths beneath oceanic spreading ridges. The estimated Afar-plume-influenced mantle source differs from those of northern Harrat Rahat and of depleted MORB (table 7; fig. 15) in its roughly three- to sixfold higher concentrations of Rb, Ba, Th, U, Nb, and Ta (but not K), as well as in its lack of depletion in the light REE. Similar to the average MORB source, but unlike the model source for northern Harrat Rahat, is the lack of a positive concentration anomaly for Sr. Because Gulf of Aden magmas derive from depleted asthenosphere admixed with Afar-plume materials (Rooney and others, 2012; Kelley and others, 2013), the dissimilarity of their source to that of northern Harrat Rahat is evidence against Afar-plume-type material being the dominant source fueling the harrat. Isotopic results allow for, but do not require, as much as 20 to 30 weight percent of a model Afar plume in the otherwise DM source for northern Harrat Rahat, although an enriched-MORB component can also account for the isotopic values of the harrat (Salters and others, 2023).

The prominent compositional difference between the northern Harrat Rahat mantle source and the source for average MORB is the former's distinct enrichment in Sr (fig. 15), also seen directly in the MORB-normalized summary plot of northern Harrat Rahat basalt compositions (fig. 6). This Sr enrichment is absent in the inferred plume-influenced source for Gulf of Aden basalts, leaving the possibilities either that it derives from the lithosphere, or from some other plume or plume component, or that it is simply within the spectrum of asthenospheric compositions whose melts aggregate to arrive at common MORB compositions. Figure 17 plots Sr/Ba versus Sr/Nd ratios for northern Harrat Rahat basalts and hawaiites, normalized to the average MORB source (median of values from Salters and Stracke, 2004; Workman and Hart, 2005). Also shown are fields defined by similarly normalized MORB and oceanic spreading-ridge gabbro compositions downloaded from the global compilation of the EarthChem-PetDB database (www.earthchem.org, accessed November 13, 2019, screened for spreading_center/igneous), xenoliths from the lower crust of the Arabia Plate (McGuire and Stern, 1993; Nasir, 1995), and mafic lavas from Harrat Lunayyir (Duncan and Al-Amri, 2013). For purposes of clarity, the fields of MORB and spreading-ridge gabbros have been subdivided into common and outlier regions, qualitatively on the basis of densely spaced versus sparse and scattered plotted compositions. The elements Nd and Sr have similar incompatibility during spinel-lherzolite partial melting, whereas Ba is much more incompatible than Sr; therefore, Sr/Nd ratio remains nearly constant during partial melting, reflecting source composition, whereas Sr/Ba ratio increases with degree of partial melting or with more depleted source compositions. Both ratios can then decline in melts undergoing gabbroic or troctolitic crystallization-differentiation and can rise in cogenetic cumulates. Figure 17 shows that, although northern Harrat Rahat basalts have higher Sr/Nd ratios than do the average MORB, their trace-element characteristics are within the range of basalts erupted along oceanic spreading ridges, albeit at the upper limit of Sr/Nd ratios of common MORB compositions. Hawaiites plot at lower Sr/Ba and Sr/Nd ratios, consistent with derivation from the basalts by gabbroic differentiation. Similarity between northern Harrat Rahat basalts and Sr-enriched MORB is reinforced by an estimate of a possible mantle source composition for Sr-enriched MORB (fig. 15; table 7), which was derived as was done for Gulf of Aden spreading-ridge basalts but was based on the median composition of MORB that have Sr/Nd ratios two to three times that of the average MORB source (from the EarthChem-PetDB database, www.earthchem.org, accessed November 13, 2019, screened for spreading_center/igneous). The harrat and Sr-rich MORB model source compositions are similar in most

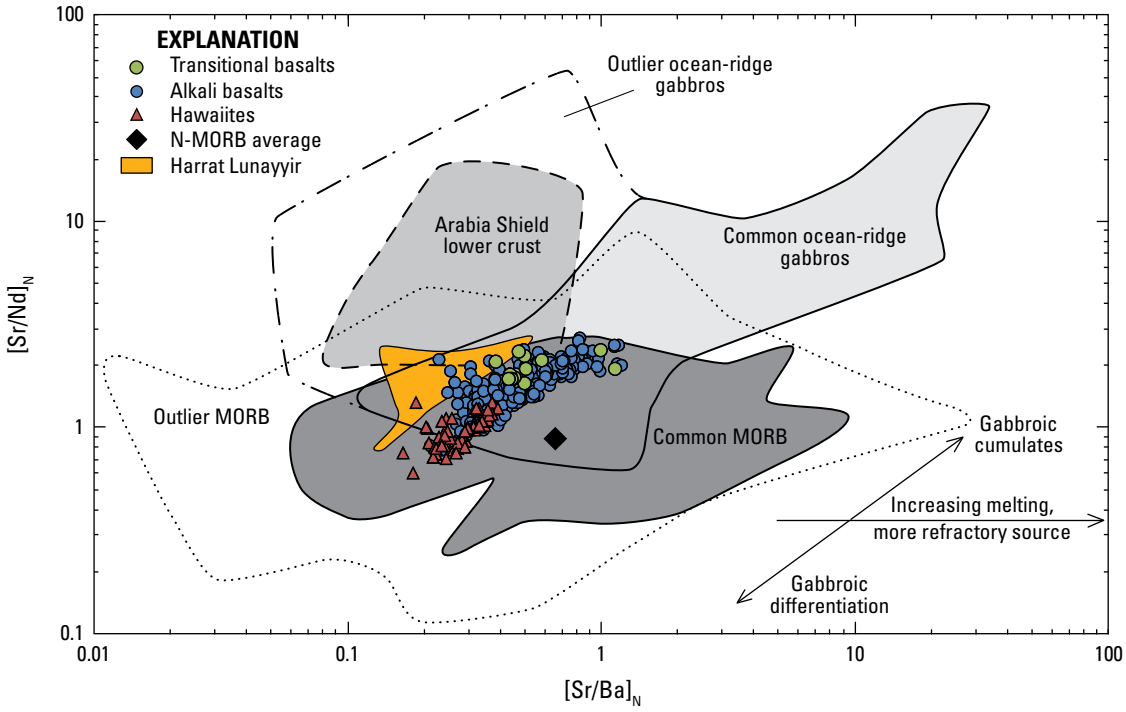

Figure 17. Plot of Sr/Ba versus Sr/Nd ratios for basalts and hawaiites of northern Harrat Rahat, compared with those of midocean ridge basalts (MORB), which are subdivided into common MORB (darkest gray shading) and outlier MORB (dotted outline) fields; N subscript indicates that concentrations in ratios are normalized to median of estimated values for MORB-source depleted mantle (in parts per million: Ba, 0.8815; Nd, 0.647; Sr, 8.7325), from Salters and Stracke (2004) and Workman and Hart (2005). Also shown are fields for common (lightest gray shading) and outlier (dash-dot outline) oceanic spreading-ridge gabbros; for granulite-facies arc-cumulate gabbros (medium-gray shading, dashed outline) from lower crust of Arabia Plate (McGuire and Stern, 1993; Nasir, 1995); and for mafic volcanic rocks of Harrat Lunayyir (orange shading), located west-northwest of northern Harrat Rahat (see fig. 1 for location) (Duncan and Al-Amri, 2013). Black diamond shows average normal MORB (N-MORB) values from Gale and others (2013). Horizontal arrow shows effect of greater degrees of partial melting or more melt-depleted (refractory) sources; diagonal arrows show effects of gabbroic differentiation on melt (lower $[Sr/Nd]_N$ and $[Sr/Ba]_N$ values) and cumulates (higher $[Sr/Nd]_N$ and $[Sr/Ba]_N$ values).

respects, indicating that the source of the harrat is mainly depleted mantle that is enriched in Sr, either by processes similar to those that preferentially enrich the mantle sources of some MORB or by encounters of partial melts of depleted asthenosphere with materials that lead to Sr enrichment.

Possible causes for high Sr/Nd ratios relative to average MORB and its mantle source include (1) the direct assimilation of plagioclase-rich materials such as cumulates of the oceanic or deep continental crust, (2) the introduction of such originally plagioclase-enriched materials into the mantle source, as in the form of Al-rich eclogites, (3) the presence in the mantle source of peridotites that are enriched in plagioclase through low-pressure processes such as by crystallization of plagioclase from percolating melts or by shallow low-degree melting, leaving residual plagioclase, and (4) the incorporation of products of convergent-margin magmatism. Basalts of the Arabian harrats ascended through lithosphere created and assembled mainly by Neoproterozoic convergent-margin magmatism and arc collisions (Gass, 1981; Stern and Johnson, 2010), and this Precambrian arc magmatism and continent formation would have influenced the composition of the shallow mantle. Convergent-margin basalts are characteristically enriched in Sr relative to the REE, but most are more strongly enriched in Ba, and usually also in Rb and K (Pearce, 1982). As a result, mafic arc magmas typically have high Sr/Nd ratios but moderate to low Sr/Ba ratios, and this characteristic carries through to the gabbroic granulite xenoliths from the lower crust of the Arabia Plate, which have been interpreted as metacumulates from Neoproterozoic arc magmatism (McGuire and Stern, 1993; Nasir, 1995). Arc cumulate xenoliths from the lower crust of the Arabia Plate have higher Sr/Nd ratios than, but about the same Sr/Ba ratios as, Arabian harrat basalts and hawaiites. Some mafic lava compositions from Harrats Rahat and

Lunayyir deviate from the main trends of Sr/Ba versus Sr/Nd ratios of their suites toward those of the field of these xenoliths (fig. 17), possibly owing to assimilation of such cumulates in the lower crust; however, most lava compositions do not, and if cumulate gabbroic components caused Sr enrichment of the harrat suites, Ba-poor gabbros that are similar in composition to those of the oceanic crust have more suitable compositions than do those created from subduction magmas.[7]

It is presently not possible to give preference among the processes that could have enriched basalts of Harrats Rahat and Lunayyir in a component similar to cumulate oceanic gabbros. The roughly two- to threefold lower degrees of melting to produce Harrat Rahat basalts compared with those of average MORB, as well as the probably even lower degrees of melting beneath Harrat Lunayyir, indicate that harrat magmas would derive in greater proportions from fertile domains that may be present in their mantle sources. During Neoproterozoic arc collisions and slab-breakoff events, plagioclase-rich parts of subducting oceanic crust may have been retained preferentially in the shallow mantle, owing to their low densities, prior to conversion to eclogite. Alternatively, sizeable domains of oceanic-type gabbros may be present in the lower crust of the Arabia Plate but have not been recognized in xenolith studies. Currently, the most robust interpretations for the Sr enrichments of Arabian harrat basalts are the mixing of such domains into depleted asthenosphere, followed by partial melting, or their assimilation at mantle-lithosphere or lower crustal depths by melts of depleted asthenosphere.

Tectono-Magmatic Synthesis

A series of geophysical studies, most recently by Chang and others (2011) and Yao and others (2017), showed that the largest Arabian harrats overlie a north-south-trending belt of substantially reduced shear velocity in the upper mantle. Velocity reductions are sufficiently strong and shallow to place the base of the lithosphere about 60 to 90 km deep beneath the crest of the regionally uplifted Arabian Shield (see fig. 1). In contrast, lithosphere of the geologically related but amagmatic and tectonically inactive Nubian Shield (fig. 1) is 120 to 180 km thick (Artemieva and Mooney, 2001), so the Arabian lithosphere has lost about one-half to two-thirds of its thickness beneath the area of continental basaltic volcanism. This velocity anomaly is also steep-sided, effectively forming a channel incised through the lower lithosphere. As expected, the southern Red Sea and Gulf of Aden spreading systems are also underlain by low shear velocities at moderate depths, but the central and northern parts of the Red Sea (from 20° N. to the Gulf of Aqaba; see fig. 1) are not (Chang and others, 2011; Yao and others, 2017). The central and northern parts of the Red Sea also lack a recognized magnetic-anomaly structure and a morphologically well-developed and continuously exposed volcanic spreading ridge. Volcanoes are exposed in the axial deeps, and submarine salt glaciers (namakiers) conceal them elsewhere (Augustin and others, 2014), but Quaternary volcanic rocks are exposed across greater areas on the shield than in the central and northern parts of the Red Sea. These observations raise the possibility that magma production is similarly vigorous or greater beneath the shield than beneath the central and northern Red Sea, despite negligible extension of the shield.

Figure 18 shows the outlines and vent axes of Neogene to Quaternary harrats on the Arabia Plate, as well as outlines of the low-shear-velocity anomaly at depths of 150 km and 85 to 105 km (Chang and others, 2011; Yao and others, 2017), translated and rotated along with the Arabia Plate and the Somalian and Sinai blocks, to close the Red Sea, Gulf of Aden, Gulf of Suez, and Gulf of Aqaba. This fixed-Africa reconstruction approximates the configuration of the northeastern part of the Africa-Arabia Plate prior to the opening of the Red Sea at about 23 to 22 Ma (Bosworth and others, 2005; Bosworth, 2015; Reilinger and others, 2015). Reversing the plate displacements places the south end of the sub-Arabian shear-velocity anomaly against the northwest end of the Afar region, at the north end of the East African Rift system, supporting the idea that a common deep-lithospheric structure may have formerly connected them and eventually led to the rift and seismic anomaly. The Red Sea opened with a more north-northwestern orientation, emplacing a swarm of basaltic dikes that flank and parallel the Red Sea, as well as effusing basalts as far away as Cairo (Bosworth, 2015), northern Jordan, and southwestern Syria (Ilani and others, 2001). The proto-East African Rift may, therefore, have ended by branching at its northern terminus, with one branch now forming the Red Sea, another forming the Gulf of Aden, and one (middle) branch marked by the present belt of major harrats and the underlying shear-velocity anomaly across the western Arabia Plate. The minor extensional faulting of the Arabian Shield, as well as the absence of recognized extensional faulting of the capping Phanerozoic-platform sedimentary section, indicate that this middle branch was a deep-lithospheric or sublithospheric feature, rather than a passive rift that developed in response to plate thinning.

Using heat-flow and seismic-velocity models, respectively, Artemieva and Mooney (2001) and Priestly and McKenzie (2006) presented evidence for substantial relief on the base of Precambrian lithosphere even in areas currently unaffected by tectonism and magmatism. Cratons that have Archean crust are generally thickest owing to their long stability and protracted cooling, whereas the base of the lithosphere in Proterozoic regions can be as much as 100 km shallower. Two mechanisms to localize magmatism along zones of thin

[7]Tang and others (2017) showed through high-precision measurements that primitive MORB glasses enriched in Sr relative to REE are also enriched in Eu. Tang and others (2017) proposed a dynamic melting model wherein fast diffusion in pyroxenes of Sr and Eu^{2+}, relative to the trivalent REE, enriches melts preferentially in Sr and Eu. It is unclear why melting and melt extraction would be faster under the Arabia Plate than under the Red Sea and Gulf of Aden spreading systems, whose basalts lack high Sr/Nd ratios; assessment of the dynamic melting model awaits diffusion results on other incompatible elements that would be similarly fractionated.

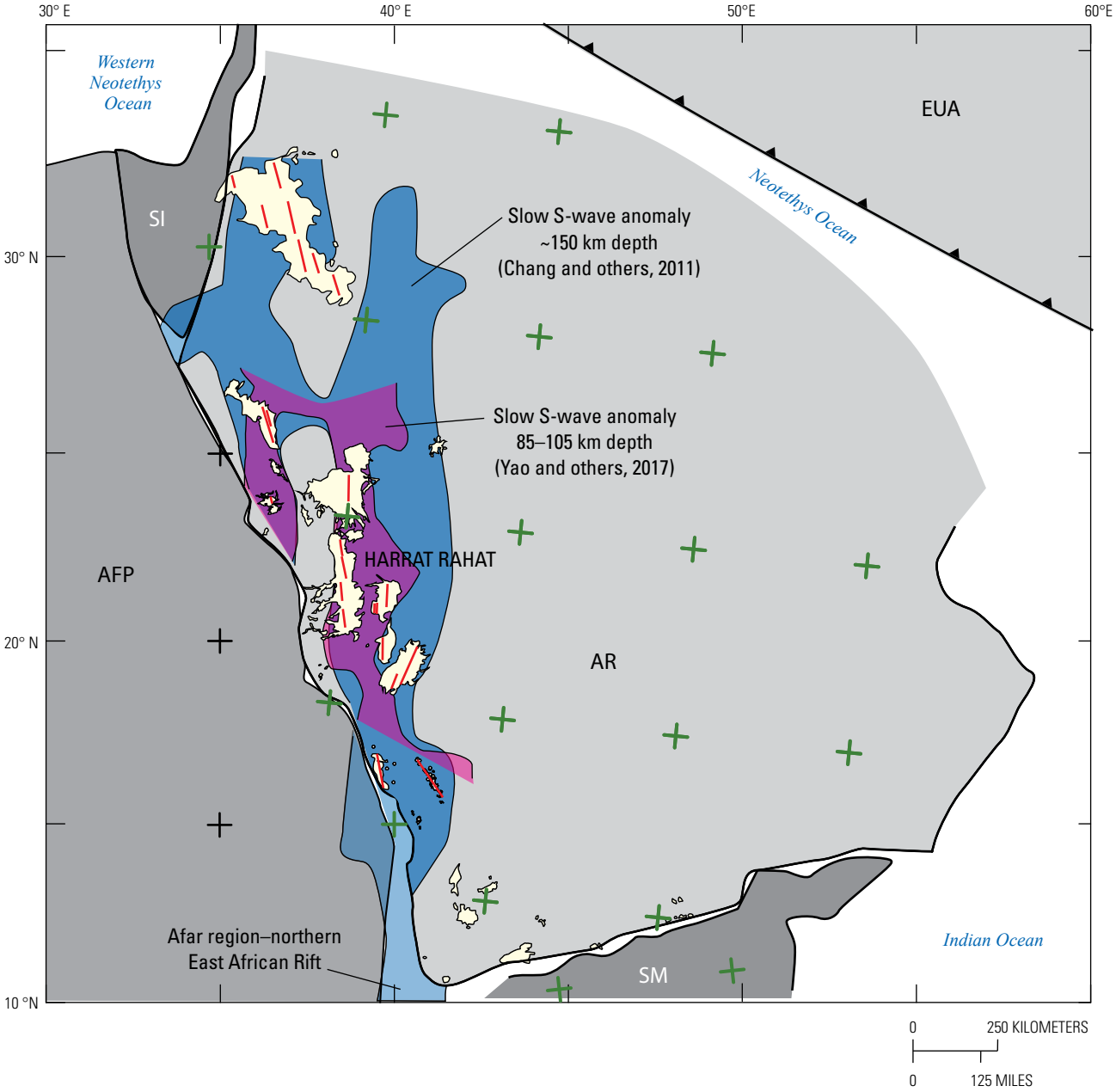

Figure 18. Schematic map showing tectonic reconstruction of part of northeastern Africa, Arabia, and Eurasia that shows Red Sea and Gulfs of Aden, Suez, and Aqaba (see fig. 1 for locations) closed by holding Africa Plate (AFP) fixed and translating and rotating Arabia Plate (AR) and Somali (SM) and Sinai (SI) blocks to match opposing shorelines; also shown are schematic locations of Eurasia Plate (EUA) and its subduction zone (barbed line; barbs on upper plate), as well as flanking ocean basins; note that northeast edge of Arabia Plate has been consumed by subduction beneath Eurasia Plate, and so its shape and extent are unknown. Translated and rotated within Arabia Plate are its present-day harrats (yellow shading) and their vent alignments (red lines), along with approximate areas of reduced upper mantle shear-velocity (S-wave) anomalies: blue shading shows area of low shear velocity, about 150 kilometers (km) deep, that is at least 150 meters/second slower than average (Chang and others, 2011); reddish-purple shading shows area of low shear velocity, 85 to 105 km deep, that is 4.15 km/second slower (Yao and others, 2017). Black plus symbols, black ticks (just inside map neatline), and latitude and longitude values (outside neatline) represent present-day (nonrotated) geographic locations, in 5° increments (Mercator projection), referenced to a fixed Africa Plate; green plus symbols represent geographic locations that are rotated, referenced to rotated lithospheric blocks.

lithosphere are (1) the capture and flow of hot mantle plume materials along such sublithospheric arches owing to thermal buoyancy (Ebinger and Sleep, 1988; Thompson and Gibson, 1991; Sleep, 2002, 2006) and (2) a magmatic feedback-and-focusing mechanism (Elkins-Tanton, 2005) wherein basaltic melts produced by decompression melting of upwelling asthenosphere or plume solidify as eclogite in the deep mantle lithosphere, increasing the density of the injected region (and softening it thermally) and promoting foundering of the eclogite-enriched part of the lithosphere. Asthenosphere then upwells into the area being vacated, leading to further decompression melting and emplacement of eclogite into overlying deep lithosphere, foundering of thereby densified lithosphere, and so on. In the case of the pre-rifted Africa-Arabia Plate, these processes may have acted in concert with the arrival and spreading of the Afar plume, displacing asthenosphere up and along arched channelways in the base of the Proterozoic lithosphere, creating magmas that intruded and eclogite-enriched the roofs of the arches, resulting in roof foundering and further upwelling and partial melting of asthenosphere (fig. 19). Numerical models indicate that such a process of magmatic densification and foundering may be more effective in thinning the lithosphere than is thermomechanical erosion by flowing hot plume (Elkins-Tanton, 2005).

Sparse high-accuracy radiometric dating (Coleman and others, 1983; Camp and Roobol, 1991a) documented some basaltic volcanism along the harrat belt before opening of the Red Sea but after the voluminous plume-driven trap volcanism in Ethiopia, Somalia, and Yemen about 31 Ma (Rooney, 2017).

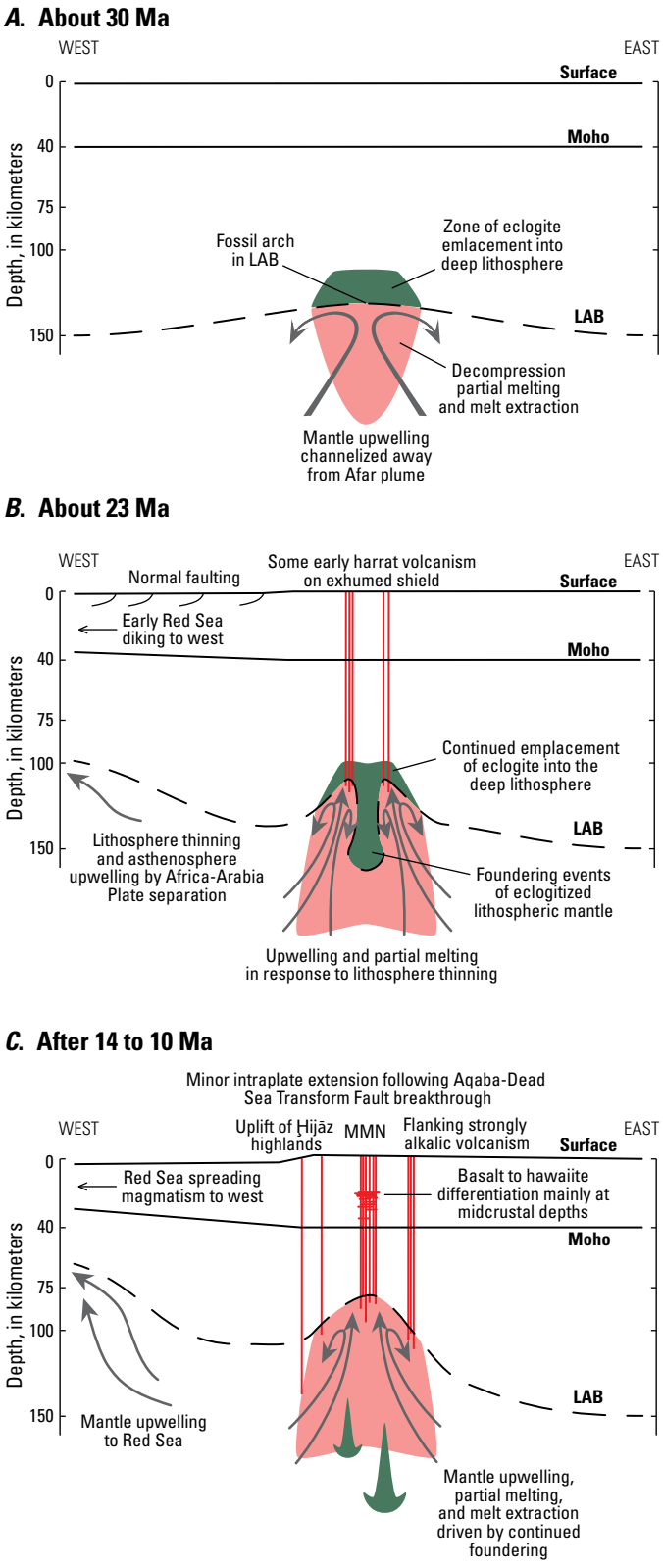

Figure 19. Schematic cross sections across western Arabian Shield, showing tectono-magmatic stages of mantle upwelling that was channelized into possible preexisting fossil arch in base of lithosphere (LAB, lithosphere-asthenosphere boundary), leading to focused partial melting (pale red shading), emplacement of eclogites (green shading), deep lithosphere foundering, and consequent further localized asthenospheric upwelling, melting, and harrat volcanism. Large, thick, gray arrows show approximate directions of mantle upwelling. Other abbreviations: MMN, Makkah-Madīnah-Nafud volcanic line (axis of voluminous active harrats); Moho, Mohorovičić discontinuity (base of continental crust). *A*, Intact Africa-Arabia Plate at about 30 Ma; sublithospheric mantle flow is driven away from Afar plume. *B*, Early (about 23 Ma) extension of Africa-Arabia Plate, leading to Red Sea opening (to left of section) and early harrat volcanism. *C*, Arabia Plate after 14 to 10 Ma, after breakthrough of Aqaba-Dead Sea Transform Fault, uplift of Ḥijāz highlands, strongly alkalic volcanism flanking MMN line, and full development of seafloor spreading in Gulf of Aden.

Red Sea rift magmatism commenced at about 23 to 22 Ma (Bosworth and others, 2005; Bosworth, 2015; Reilinger and others, 2015) and extended as far away as northern Jordan or Syria (Ilani and others, 2001). A lull in harrat volcanism apparently occurred until about 14 to 13 Ma, after which many harrats erupted widely, extending into historical times (Camp and Roobol, 1991a). This resumption near 13 Ma corresponded with (1) uplift and exhumation of Ḥijāz-ʻAsīr highlands along the east flank of the Red Sea (Bohannon and others, 1989), (2) rupture and onset of motion of the Aqaba-Dead Sea Transform Fault (Reilinger and others, 2015), and (3) full opening of the Gulf of Aden and its oceanic spreading system (Bosworth and others, 2005). These changes were so widespread and diverse that they were unlikely to have been triggered by delamination of lithosphere localized beneath the belt of largest harrats. Instead, it may be that, by about 13 Ma, the lithosphere of the majority of the Arabia Plate had become sufficiently thinned and weakened that the plate failed along its margins and incipiently in its interior (Calvert and Sisson, 2023), facilitating the ascent of magma through the lithosphere and resulting in resumed voluminous harrat volcanism.

Concluding Summary

Basaltic magmas of northern Harrat Rahat mainly formed by low-degree (2–4 weight percent) decompression melting of depleted asthenosphere that contained modest admixed exotic material, possibly from the Afar plume. A distinct compositional characteristic is the presence of a component similar to spreading-ridge cumulate gabbros, either in the source or encountered by magmas in transit to the surface. Asthenospheric upwelling is localized beneath the harrat belt in a channelway incised in the base of the subcontinental mantle lithosphere, with continued upwelling and melting possibly focused and driven by foundering of overlying lithosphere that had densified and softened slightly earlier by magmatic intrusions that solidified as eclogite. Parental magmas of northern Harrat Rahat segregated from their upwelling sources in the deeper parts of the spinel-peridotite facies, close to the present lithosphere-asthenosphere boundary, but substantial proportions of melting took place even deeper in the garnet-peridotite stability field (Salters and others, 2023). The mantle source had potential temperatures similar to those that produce oceanic spreading-ridge basalts. Its depleted-source character and its low potential temperature are evidence against a deeply sourced mantle plume as the dominant cause of Quaternary harrat magmatism.

Upon segregating, magmas ascended into the crust and underwent modest amounts of olivine-dominated crystallization-differentiation, followed by extensive gabbroic differentiation, separable into an early stage that reduced melt-SiO_2 concentrations, followed by an increasing SiO_2 stage once titanomagnetite joined the crystallizing assemblage, with the transition between these at MgO concentrations of 6 to 7 weight percent in the melt. Most basalts, however, are mixtures of variably differentiated magmas, and some basalts and hawaiites assimilated evolved gabbroic cumulates from the alkalic harrat system, leading to preferential enrichment in apatite components. Extents of solidification, referenced to an inferred primary-magma composition, are no more than 10 weight percent, for the olivine-dominated differentiation interval; from less than 10 to 35 weight percent, for the decreasing-SiO_2 gabbroic interval; and a total of about 80 weight percent, to produce typical hawaiites. Gabbroic differentiation at midcrustal depths gives the closest correspondence between rock compositions and modeled liquid lines of descent and is broadly consistent with the mineral assemblages predicted by thermodynamic modeling of cumulates. Magmas, undoubtedly, also intruded and stalled at greater crustal depths, but any differentiates formed there appear not to have reached the surface without further differentiating or mixing at midcrustal depths. The Arabian Shield has a well-developed Conrad discontinuity, with higher seismic velocities at depths greater than 20 km, and basaltic magmas may arrest at midcrustal depths, owing to density trapping beneath the low-density upper crust.

Petrology, geology, and geophysics do not indicate the presence of sizeable magma bodies in the upper crust beneath the volcanic field. Despite evidence for differentiation in the crust and indications of complex mixing between magmas and between magmas and prior cumulates, isotopic and geochemical results (Salters and others, 2023) allow for only small degrees of interaction with rocks of the Precambrian continental crust.

Acknowledgments

This work was enabled by the financial and logistical support of the Saudi Geological Survey (SGS), under the leadership of Dr. Zohair A. Nawab, President (retired), with direct logistical oversight by Dr. Hani Zahran, (former) Director of the National Centre for Earthquakes and Volcanoes. In addition to the authors of this report, geologic mapping and sampling were performed by Tim Orr, Dave Sherrod, Duane Champion, Joel Robinson, and Juliet Ryan-Davis, all of the U.S. Geological Survey (USGS). Conspicuous field support was provided by Khalid Hassan, Fawaz Muquyyim, Mahmod Ashur, Turki Hablil, and Peter Dimaala (pilot) (all SGS). Constructive reviews by Michelle Coombs and Charlie Bacon, as well as editorial comments by Mike Clynne (all USGS), improved the presentation and scientific interpretations. We thank Taryn Lindquist for her skilled edit of the paper.

References Cited

Andersen, D.J., and Lindsley, D.H., 1998, Internally consistent solution models for Fe–Mg–Mn–Ti oxides—Fe–Ti oxides: American Mineralogist, v. 73, p. 714–726.

Artemieva, I.M., and Mooney, W.D., 2001, Thermal thickness and evolution of Precambrian lithosphere—A global study: Journal of Geophysical Research, v. 106, p. 16,387–16,414.

Augustin, N., Devey, C.W., van der Zwan, F.M., Feldens, P., Tominaga, M., Bantan, R.A., and Kwasnitschka, T., 2014, The rifting to spreading transition in the Red Sea: Earth and Planetary Science Letters, v. 395, p. 217–230.

Baker, B.H., Goles, G.G., Leeman, W.P., and Lindstrom, M.M., 1977, Geochemistry and petrogenesis of a basalt-benmoreite-trachyte suite from the southern part of the Gregory Rift, Kenya: Contributions to Mineralogy and Petrology, v. 64, p. 303–332.

Barberi, F., Ferrara, G., Santacroce, R., Treuil, M., and Varet, J., 1975, A transitional basalt-pantellerite sequence of fractional crystallization, the Boina Centre (Afar Rift, Ethiopia): Journal of Petrology, v. 16, p. 22–56.

Basaltic Volcanism Study Project, 1981, Basaltic Volcanism on the Terrestrial Planets: Oxford, United Kingdom, Pergamon Press, Inc., 1,286 p.

Beckinsale, R.D., Pankhurst, R.J., Skelhorn, R.R., and Walsh, J.N., 1978, Geochemistry and petrogenesis of the early Tertiary lava pile of the Isle of Mull, Scotland: Contributions to Mineralogy and Petrology, v. 66, p. 415–427.

Blundy, J.D., and Wood, B.J., 1991, Crystal chemical controls on the partitioning of Sr and Ba between plagioclase, silicate melts, and hydrothermal solutions: Geochimica et Cosmochimica Acta, v. 55, p. 193–209.

Blundy, J.D., and Wood, B.J., 2003, Mineral-melt partitioning of uranium, thorium, and their daughters, *in* Bourdon, B., Henderson, G.M., Lundstrom, C.C., and Turner, S.P., eds., Uranium-series geochemistry: Reviews in Mineralogy, v. 52, p. 59–123.

Bohannon, R.G., Naeser, D.L., Schmidt, D.L., and Zimmermann, R.A., 1989, The timing of uplift, volcanism, and rifting peripheral to the Red Sea—A case for passive rifting?: Journal of Geophysical Research, v. 94, p. 1683–1701.

Bohrson, W.A., and Reid, M.R., 1995, Petrogenesis of alkaline basalts from Socorro Island, Mexico—Trace element evidence for contamination of ocean island basalt in the shallow ocean crust: Journal of Geophysical Research, v. 100, p. 24,555–24,576.

Bohrson, W.A., and Reid, M.R., 1997, Genesis of silicic peralkaline volcanic rocks in an ocean island setting by crustal melting and open-system processes—Socorro Island, Mexico: Journal of Petrology, v. 38, p. 1137–1166.

Bosworth, W., 2015, Geological evolution of the Red Sea—Historical background, review, and synthesis, *in* Rasul, N.M.A., and Stewart, I.C.F., eds., The Red Sea: Berlin, Springer-Verlag, p. 45–78.

Bosworth, W., Huchon, P., and McClay, K., 2005, The Red Sea and Gulf of Aden basins: Journal of African Earth Science, v. 43, p. 334–378.

Bourdon, B., and Sims, K.W.W., 2003, U-series constraints on intraplate basaltic magmatism, *in* Bourdon, B., Henderson, G.M., Lundstrom, C.C., and Turner, S.P., eds., Uranium-series geochemistry: Reviews in Mineralogy, v. 52, p. 215–254.

Brown, G.F., Schmidt, D.L., and Huffman, A.C., Jr., 1989, Geology of the Arabian Peninsula—Shield area of western Saudi Arabia: U.S. Geological Survey Professional Paper 560–A, 188 p.

Calvert, A.T., and Sisson, T.W., 2023, Cenozoic tectonics of the western Arabia Plate related to harrat magmatism near Al Madīnah, Kingdom of Saudi Arabia, chap. B *of* Sisson, T.W., Calvert, A.T., and Mooney, W.D., eds., Active volcanism on the Arabian Shield—Geology, volcanology, and geophysics of northern Harrat Rahat and vicinity, Kingdom of Saudi Arabia: U.S. Geological Survey Professional Paper 1862 [also released as Saudi Geological Survey Special Report SGS–SP–2021–1], 28 p., https://doi.org/10.3133/pp1862B.

Camp, V.E., Hooper, P.R., Roobol, J.M., and White, D.L., 1987, The Madinah eruption, Saudi Arabia—Magma mixing and simultaneous extrusion of three basaltic chemical types: Bulletin of Volcanology, v. 49, p. 489–508.

Camp, V.E., and Roobol, M.J., 1989, The Arabian continental alkali basalt province—Part I. Evolution of Harrat Rahat, Kingdom of Saudi Arabia: Geological Society of America Bulletin, v. 101, p. 71–95.

Camp, V.E., and Roobol, M.J., 1991a, Comment on "Topographic and volcanic asymmetry around the Red Sea—Constraints on rift models" by T.H. Dixon, E.R. Ivins, and J.F. Brenda: Tectonics, v. 10, p. 649–652.

Camp, V.E., and Roobol, M.J., 1991b, Geologic map of the Cenozoic Harrat Rahat lava field, Kingdom of Saudi Arabia: Saudi Arabian Ministry of Petroleum and Mineral Resources Geoscience Map GM–123, scale 1:250,000, 37 p.

Camp, V.E., and Roobol, M.J., 1992, Upwelling asthenosphere beneath western Arabia and its regional implications: Journal of Geophysical Research, v. 97, p. 15,255–15,271.

Camp, V.E., Roobol, M.J., and Hooper, P.R., 1991, The Arabian continental alkali basalt province—Part II. Evolution of Harrats Khaybar, Ithnayn, and Kura, Kingdom of Saudi Arabia: Geological Society of America Bulletin, v. 103, p. 363–391.

Chang, S.-J., Merino, M., Van der Lee, S., Stein, S., and Stein, C.A., 2011, Mantle flow beneath Arabia offset from opening of the Red Sea: Geophysical Research Letters, v. 38, 5 p., https://doi.org/10.1029/2010GL045852.

Charlier, B., Namur, O., and Grove, T.L., 2013, Compositional and kinetic controls on liquid immiscibility in ferrobasalt-rhyolite volcanic and plutonic series: Geochimica et Cosmochimica Acta, v. 113, p. 79–93.

Christensen, N.I., and Mooney, W.D., 1995, Seismic velocity structure and composition of the continental crust—A global view: Journal of Geophysical Research, v. 100, p. 9761–9788.

Coleman, R.G., 1993, Geologic evolution of the Red Sea: Oxford Monographs on Geology and Geophysics, v. 34, 86 p.

Coleman, R.G., Gregory, R.T., and Brown, G.F., 1983, Cenozoic volcanic rocks of Saudi Arabia: U.S. Geological Survey Open-File Report 83–788, 82 p.

Connolly, J.A.D., 2009, The geodynamic equation of state—What and how: Geochemistry Geophysics Geosystems, v. 10, 19 p., https://doi.org/10.1029/2009GC002540.

Cox, K.G., Bell, J.D., and Pankhurst, R.J., 1979, The Interpretation of Igneous Rocks: London, George Allen & Unwin, 450 p.

Cox, K.G., Gass, I.G., and Mallick, D.I.J., 1970, The peralkaline volcanic suite of Aden and Little Aden, South Arabia: Journal of Petrology, v. 11, p. 433–461.

Downs, D.T., 2019, Major- and trace-element chemical analyses of rocks from the northern Harrat Rahat volcanic field and surrounding area, Kingdom of Saudi Arabia: U.S. Geological Survey data release, https://doi.org/10.5066/P91HL91C.

Downs, D.T., Robinson, J.E., Stelten, M.E., Champion, D.E., Dietterich, H.R., Sisson, T.W., Zahran, H., Hassan, K., and Shawali, J., 2019, Geologic map of the northern Harrat Rahat volcanic field, Kingdom of Saudi Arabia: U.S. Geological Survey Scientific Investigations Map 3428 [also released as Saudi Geological Survey Special Report SGS–SP–2019–2], 65 p., 4 sheets, scales 1:75,000, 1:25,000, https://doi.org/10.3133/sim3428.

Downs, D.T., Stelten, M.E., Champion, D.E., Dietterich, H.R., Hassan, K., and Shawali, J., 2023, Eruptive history within the vicinity of Al Madīnah in northern Harrat Rahat, Kingdom of Saudi Arabia, chap. C *of* Sisson, T.W., Calvert, A.T., and Mooney, W.D., eds., Active volcanism on the Arabian Shield—Geology, volcanology, and geophysics of northern Harrat Rahat and vicinity, Kingdom of Saudi Arabia: U.S. Geological Survey Professional Paper 1862 [also released as Saudi Geological Survey Special Report SGS–SP–2021–1], 41 p., https://doi.org/10.3133/pp1862C.

Downs, D.T., Stelten, M.E., Champion, D.E., Dietterich, H.R., Nawab, Z., Zahran, H., Hassan, K., and Shawali, J., 2018, Volcanic history of the northernmost part of the Harrat Rahat volcanic field, Saudi Arabia: Geosphere, v. 14, p. 1253–1282.

Duncan, R.A., and Al-Amri, A.M., 2013, Timing and composition of volcanic activity at Harrat Lunayyir, western Saudi Arabia: Journal of Volcanology and Geothermal Research, v. 260, p. 103–116.

Dygert, N., Draper, D.S., Rapp, J.F., Lapen, T.J., Fagan, A.L., and Neal, C.R., 2020, Experimental determinations of trace element partitioning between plagioclase, pigeonite, olivine, and lunar basaltic melts and an fO_2 dependent model for plagioclase-melt Eu partitioning: Geochimica et Cosmochimica Acta, v. 279, p. 258–280, https://doi.org/10.1016/j.gca.2020.03.037.

Ebinger, C.J., and Sleep, N.H., 1988, Cenozoic magmatism throughout east Africa resulting from a single plume: Nature, v. 395, p. 788–791.

Elkins-Tanton, L.T., 2005, Continental magmatism caused by lithospheric delamination, *in* Foulger, G.R., Natland, J.H., Presnall, D.C., and Anderson, D.L., eds., Plates, plumes, and paradigms: Geological Society of America Special Paper 388, p. 449–461.

Field, J., Blundy, J., Calvert, A., and Yirgu, G., 2013, Magmatic history of Dabbahu, a composite volcano in the Afar Rift, Ethiopia: Geological Society of America Bulletin, v. 125, p. 128–147.

Fuhrman, M., and Lindsley, D.L., 1988, Ternary-feldspar modeling and thermometry: American Mineralogist, v. 73, p. 201–215.

Furman, T., Bryce, J., Rooney, T., Hanan, B., Yirgu, G., and Ayalew, D., 2006, Heads and tails—30 million years of the Afar plume, *in* Yirgu, G., Ebinger, C.J., and Maguire, P.H.K, eds., The Afar Volcanic Province within the East African Rift System: Geological Society of London Special Publication 259, p. 95–119.

Gale, A., Dalton, C.A., Langmuir, C.H., Su, Y., and Schilling, J.-G., 2013, The mean composition of ocean ridge basalts: Geochemistry Geophysics Geosystems, v. 14, p. 489–518.

Ganguly, J., 2005, Adiabatic decompression and melting mantle rocks—An irreversible thermodynamic analysis: Geophysical Research Letters, v. 32, 4 p.

Gass, I.G., 1970, Tectonic and magmatic evolution of the Afro-Arabian dome, *in* Clifford, T.E., and Gass, I.G., eds., African Magmatism and Tectonics: Edinburgh, Oliver and Boyd, p. 285–300.

Gass, I.G., 1981, Chapter 15 Pan-African (upper Proterozoic) plate tectonics of the Arabian-Nubian shield, *in* Kroner, A., ed., Developments in Precambrian Geology: Amsterdam, Elsevier, v. 4, p. 387–405.

Ghiorso, M.S., Hirschmann, M.M., Reiners, P.W., and Kress, V.C., 2002, The pMELTS—A revision of MELTS for improved calculation of phase relations and major element partitioning related to partial melting of the mantle to 3 GPa: Geochemistry Geophysics Geosystems, v. 3, 35 p., https://doi.org/10.1029/2001GC000217.

Ghiorso, M.S., and Sack, R.O., 1995, Chemical mass transfer in magmatic processes IV—A revised and internally consistent thermodynamic model for the interpolation and extrapolation of solid-liquid equilibria in magmatic systems at elevated temperatures and pressures: Contributions to Mineralogy and Petrology, v. 119, p. 197–212.

Green, E.C.R., White, R.W., Diener, J.F.A., Powell, R., Holland, T.J.B., and Palin, R.M., 2016, Activity-composition relations for the calculation of partial melting of metabasic rocks: Journal of Metamorphic Geology, v. 34, p. 845–869.

Grove, T.L., 1993, Corrections to expressions for calculating mineral components in "Origin of the calc-alkaline series lavas at medicine lake volcano by fractionation, assimilation and mixing" and "Experimental petrology of normal MORB near the Kane Fracture Zone: 22°-25°N, mid-Atlantic ridge": Contributions to Mineralogy and Petrology, v. 114, p. 422–424.

Grove, T.L., Holbig, E.S., Barr, J.A., Till, C.B., and Krawczynski, M.J., 2013, Melts of garnet lherzolite—Experiments, models and comparison to melts of pyroxenite and carbonated lherzolite: Contributions to Mineralogy and Petrology, v. 166, p. 887–910.

Hacker, B.R., Kelemen, P.B., and Behn, M.D., 2015, Continental lower crust: Annual Reviews of Earth and Planetary Sciences, v. 43, p. 167–205.

Hart, S.R., Blusztajn, J., LeMasurier, W.E., and Rex, D.C., 1997, Hobbs Coast Cenozoic volcanism—Implications for the West Antarctic rift system: Chemical Geology, v. 139, p. 223–248.

Herzberg, C., and Asimow, P.D., 2008, Petrology of some oceanic island basalts—PRIMELT2.XLS software for primary magma calculation: Geochemistry Geophysics Geosystems, v. 9, 25 p., https://doi.org/10.1029/2008GC002057.

Herzberg, C., and Asimow, P.D., 2015, PRIMELT3 MEGA. XLSM software for primary magma calculation—Peridotite primary magma MgO contents from the liquidus to the solidus: Geochemistry Geophysics Geosystems, v. 16, p. 563–578, https://doi.org/10.1002/214GC005631.

Holland, T.J.B., and Powell, R., 2011, An improved and extended internally consistent thermodynamic dataset for phases of petrological interest, involving a new equation of state for solids: Journal of Metamorphic Geology, v. 29, p. 333–383, https://doi.org/10.1111/j.1525-1314.2010.00923.

Ilani, S., Harlavan, Y., Tarawneh, K., Rabba, I., Weinberger, R., Ibrahim, K., Peltz, S., and Steinitz, G., 2001, New K-Ar ages of basalts from the Harrat Ash Shaam volcanic field in Jordan—Implications for the span and duration of the upper mantle upwelling beneath the western Arabian plate: Geology, v. 29, p. 171–174.

Irvine, T.N., and Baragar, W.R.A., 1971, A guide to the chemical classification of common volcanic rocks: Canadian Journal of Earth Sciences, v. 8, p. 523–548.

Jameson, B.G., and Clarke, D.B., 1970, Potassium and associated elements in tholeiitic basalts: Journal of Petrology, v. 11, p. 183–204.

Jennings, E.S., and Holland, T.J.B., 2015, A simple thermodynamic model for melting of peridotite in the system NCFMASOCr: Journal of Petrology, v. 56, p. 1–24.

Kawasaki, T., 1998, Thermodynamic formulations of $(Ca,Fe,Mg)_2SiO_4$ olivine: Mineralogical Journal, v. 20, p. 135–149.

Kelley, K.A., Kingsley, R., and Schilling, J.-G., 2013, Composition of plume-influenced mid-ocean ridge lavas and glasses from the Mid-Atlantic Ridge, East Pacific Rise, Galápagos Spreading Center, and Gulf of Aden: Geochemistry Geophysics Geosystems, v. 14, p. 223–242, https://doi.org/10.1002/ggge.20049.

Kress, V.C., and Carmichael, I.S.E., 1991, The compressibility of silicate liquids containing Fe_2O_3 and the effect of composition, temperature, oxygen fugacity and pressure on their redox states: Contributions to Mineralogy and Petrology, v. 108, p. 82–92.

Langenheim, V.E., Ritzinger, B.T., Zahran, H., Shareef, A., and Al-dahri, M., 2019, Crustal structure of the northern Harrat Rahat volcanic field (Saudi Arabia) from gravity and aeromagnetic data: Tectonophysics, v. 750, p. 9–21.

Langenheim, V.E., Ritzinger, B.T., Zahran, H.M., Shareef, A., and Al-Dhahry, M.K., 2023, Depth to basement and crustal structure of the northern Harrat Rahat volcanic field, Kingdom of Saudi Arabia, from gravity and aeromagnetic data, chap. K *of* Sisson, T.W., Calvert, A.T., and Mooney, W.D., eds., Active volcanism on the Arabian Shield—Geology, volcanology, and geophysics of northern Harrat Rahat and vicinity, Kingdom of Saudi Arabia: U.S. Geological Survey Professional Paper 1862 [also released as Saudi Geological Survey Special Report SGS–SP–2021–1], 18 p., https://doi.org/10.3133/pp1862K.

Le Bas, M.J., Le Maitre, R.W., Streckeisen, A., and Zanettin, B., 1986, A chemical classification of volcanic rocks based on the total alkali-silica diagram: Journal of Petrology, v. 27, p. 745–750.

Lee, C.-T.A., Luffi, P., Plank, T., Dalton, H., and Leeman, W.P., 2009, Constraints on the depths and temperatures of basaltic magma generation on Earth and other terrestrial planets using new thermobarometers for mafic magmas: Earth and Planetary Science Letters, v. 279, p. 20–33.

Lindsley, D.H., 1983, Pyroxene thermometry: American Mineralogist, v. 68, p. 477–493.

Lundstrom, C.C., 2003, Uranium-series disequilibria in mid-ocean ridge basalts—Observations and models of basalt genesis, *in* Bourdon, B., Henderson, G.M., Lundstrom, C.C., and Turner, S.P., eds., Uranium-series geochemistry: Reviews in Mineralogy, v. 52, p. 175–214.

Macdonald, G.A., and Katsura, T., 1964, Chemical composition of Hawaiian lavas: Journal of Petrology, v. 5, p. 82–133.

McGuire, A.V., and Stern, R.J., 1993, Granulite xenoliths from western Saudi Arabia—The lower crust of the Late Precambrian Arabian–Nubian Shield: Contributions to Mineralogy and Petrology, v. 114, p. 395–408.

McKenzie, D., and Bickle, M.J., 1988, The volume and composition of melt generated by extension of the lithosphere: Journal of Petrology, v. 29, p. 625–679.

Minster, J.F., and Allègre, C.J., 1978, Systematic use of trace elements in igneous processes—III. Inverse problem of melting in volcanic suites: Contributions to Mineralogy and Petrology, v. 68, p. 37–52.

Moufti, R.H., 1985, The geology of Harrat Al Madinah volcanic field Harrat Rahat, Saudi Arabia: Lancaster, United Kingdom, Lancaster University, Ph.D. dissertation, 476 p.

Moufti, M.R., Moghazi, A.M., and Ali, K.A., 2012, Geochemistry and Sr-Nd-Pb isotopic composition of the Harrat Al-Madinah volcanic field, Saudi Arabia: Gondwana Research, v. 21, p. 670–689.

Murcia, H., Lindsay, J.M., Németh, K., Smith, I.E.M., Cronin, S.J., Moufti, M.R.H., El-Masry, N.N., and Niedermann, S., 2016, Geology and geochemistry of late Quaternary volcanism in northern Harrat Rahat, Kingdom of Saudi Arabia—Implications for eruption dynamics, regional stratigraphy, and magma evolution, *in* Németh, K., Carrasco-Núñez, G., Aranda-Gómez, J.J., and Smith, I.E.M., eds., Monogenetic volcanism: Geological Society of London Special Publication 446, p. 173–204, https://doi.org/10.1144/SP446.2.

Nasir, S., 1995, Mafic lower crustal xenoliths from the northwestern part of the Arabian plate: European Journal of Mineralogy, v. 7, p. 217–230.

O'Neill, H.St.C., 2016, The smoothness and shapes of chondrite-normalized rare earth element patterns in basalts: Journal of Petrology, v. 57, p. 1463–1508.

Pearce, J.A., 1982, Trace element characteristics of lavas from destructive plate boundaries, *in* Thorpe, R.S., ed., Andesites: Hoboken, N.J., John Wiley & Sons, p. 525–548.

Philpotts, J.A., 1970, Redox estimation from a calculation of Eu^{2+} and Eu^{3+} concentrations in natural phases: Earth and Planetary Science Letters, v. 9, p. 257–268.

Priestly, K., and McKenzie, D., 2006, The thermal structure of the lithosphere from shear wave velocities: Earth and Planetary Science Letters, v. 244, p. 285–301.

Reilinger, R., McClusky, S., and ArRajehi, A., 2015, Geodetic constraints on the geodynamic evolution of the Red Sea, *in* Rasul, N.M.A., and Stewart, I.C.F., eds., The Red Sea: Berlin, Springer-Verlag, p. 135–149.

Robinson, J.E., and Downs, D.T., 2023, Overview of the Cenozoic geology of the northern Harrat Rahat volcanic field, Kingdom of Saudi Arabia, chap. R *of* Sisson, T.W., Calvert, A.T., and Mooney, W.D., eds., Active volcanism on the Arabian Shield—Geology, volcanology, and geophysics of northern Harrat Rahat and vicinity, Kingdom of Saudi Arabia: U.S. Geological Survey Professional Paper 1862 [also released as Saudi Geological Survey Special Report SGS–SP–2021–1], 20 p., scale 1:100,000, https://doi.org/10.3133/pp1862R.

Rodgers, N., Macdonald, R., Fitton, J.G., George, R., Smith, M., and Barreiro, B., 2000, Two mantle plumes beneath the East African rift system—Sr, Nd, and Pb isotopic evidence from Kenya Rift basalts: Earth and Planetary Science Letters, v. 176, p. 387–400.

Roeder, E., and Weiblen, P.W., 1970, Silicate liquid immiscibility in lunar magmas, evidenced by melt inclusions in lunar rocks: Science, v. 30, p. 641–644.

Rooney, T.O., 2017, The Cenozoic magmatism of East-Africa, Part I—Flood basalts and pulsed magmatism: Lithos, v. 286–287, p. 264–301.

Rooney, T.O., Hanan, B.B., Graham, D.W., Blichert-Toft, J., and Schilling, J.-G., 2012, Upper mantle pollution during Afar plume-continental rift interaction: Journal of Petrology, v. 53, p. 365–389.

Ryan, W.B.F., Carbotte, S.M., Coplan, J.O., O'Hara, S., Melkonian, A., Arko, R., Weissel, R.A., Ferrini, V., Goodwillie, A., Nitsche, F., Bonczkowski, J., and Zemsky, R., 2009, Global multi-resolution topography synthesis: Geochemistry, Geophysics, Geosystems, v. 10, Q03014, https://doi:10.1029/2008GC002332.

Salters, V.J.M., and Hart, S.R., 1989, The hafnium paradox and the role of garnet in the source of mid-ocean-ridge basalts: Nature, v. 342, p. 420–422.

Salters, V.J.M., Sachi-Kocher, A., Downs, D.T., Stelten, M.E., and Sisson, T.W., 2023, Isotopic and geochemical evidence for the source of volcanism at Harrat Rahat, Kingdom of Saudi Arabia, chap. J *of* Sisson, T.W., Calvert, A.T., and Mooney, W.D., eds., Active volcanism on the Arabian Shield—Geology, volcanology, and geophysics of northern Harrat Rahat and vicinity, Kingdom of Saudi Arabia: U.S. Geological Survey Professional Paper 1862 [also released as Saudi Geological Survey Special Report SGS–SP–2021–1], 30 p., https://doi.org/10.3133/pp1862J.

Salters, V.J.M., and Stracke, A., 2004, Composition of the depleted mantle: Geochemistry Geophysics Geosystems, v. 15, 27 p., https://doi.org/10.1029/2003GC000597.

Sarafian, E., Gaetani, G.A., Hauri, E.H., and Sarafian, A.R., 2017, Experimental constraints on the damp peridotite solidus and oceanic mantle potential temperature: Science, v. 355, p. 942–945.

Sembroni, A., Faccenna, C., Becker, T.W., Molin, P., and Abebe, B., 2016, Long-term, deep-mantle support of the Ethiopia–Yemen Plateau: Tectonics, v. 35, p. 469–488.

Shaw, D.M., 1970, Trace element fractionation during anatexis: Geochimica et Cosmochimica Acta, v. 34, p. 237–242.

Shaw, D.M., 1979, Trace element melting models: Physics and Chemistry of the Earth, v. 11, p. 577–586.

Sleep, N.H., 2002, Ridge-crossing mantle plumes and tracks: Geochemistry Geophysics Geosystems, v. 3, 33 p., https://doi.org/10.1029/2001GC000290.

Sleep, N.H., 2006, Mantle plumes from top to bottom: Earth-Science Reviews, v. 77, p. 231–271.

Stelten, M.E., Downs, D.T., Champion, D.E., Dietterich, H.R., Calvert, A.T., Sisson, T.W., Mahood, G.A., and Zahran, H., 2020, The timing and compositional evolution of volcanism within northern Harrat Rahat, Kingdom of Saudi Arabia: Geological Society of America Bulletin, v. 132, p. 1381–1403, https://doi.org/10.1130/B35337.1.

Stelten, M.E., Downs, D.T., Champion, D.E., Dietterich, H.R., Calvert, A.T., Sisson, T.W., Mahood, G.A., and Zahran, H.M., 2023, Eruptive history of northern Harrat Rahat—Volume, timing, and composition of volcanism over the past 1.2 million years, chap. D *of* Sisson, T.W., Calvert, A.T., and Mooney, W.D., eds., Active volcanism on the Arabian Shield—Geology, volcanology, and geophysics of northern Harrat Rahat and vicinity, Kingdom of Saudi Arabia: U.S. Geological Survey Professional Paper 1862 [also released as Saudi Geological Survey Special Report SGS–SP–2021–1], 46 p., https://doi.org/10.3133/pp1862D.

Stelten, M.E., Downs, D.T., Dietterich, H.R., Mahood, G.A., Calvert, A.T., Sisson, T.W., Zahran, H., and Shawali, J., 2018, Timescales of magmatic differentiation from alkali basalt to trachyte within the Harrat Rahat volcanic field, Kingdom of Saudi Arabia: Contributions to Mineralogy and Petrology, v. 173, 17 p.

Stern, R.J., and Johnson, P., 2010, Continental lithosphere of the Arabian plate—A geologic, petrologic, and geophysical synthesis: Earth-Science Reviews, v. 101, nos. 1–2, p. 29–67, https://doi.org/10.1016/j.earscirev.2010.01.002.

Streckeisen, A., 1976, To each plutonic rock its proper name: Earth-Science Reviews, v. 12, p. 1–33.

Sun, S.-S., and McDonough, W.F., 1989, Chemical and isotopic systematics of oceanic basalts—Implications for mantle composition and processes, *in* Saunders, A.D., and Norry, M.J. eds., Magmatism in the ocean basins: Geological Society of London Special Publication 42, p. 313–345.

Tang, M., McDonough, W.F., and Ash, R.D., 2017, Europium and strontium anomalies in the MORB source mantle: Geochimica et Cosmochimica Acta, v. 197, p. 132–141.

Thompson, R.N., 1974, Primary basalts and magma genesis—I. Skye, north-west Scotland: Contributions to Mineralogy and Petrology, v. 45, p. 317–341.

Thompson, R.N., 1975, Primary basalts and magma genesis—II. Snake River Plain, Idaho, U.S.A.: Contributions to Mineralogy and Petrology, v. 52, p. 213–232.

Thompson, R.N., Esson, J., and Dunham, A.C., 1972, Major element variation in the Eocene lavas of the Isle of Skye, Scotland: Journal of Petrology, v. 13, p. 219–253.

Thompson, R.N., and Gibson, S.A., 1991, Subcontinental mantle plumes, hotspots, and pre-existing thinspots: Journal of the Geological Society of London, v. 148, p. 973–977.

Till, C.B., Grove, T.L., and Krawczynski, M.J., 2012, A melting model for variably depleted and enriched lherzolite in the plagioclase and spinel stability fields: Journal of Geophysical Research, v. 117, 23 p., https://doi.org/10.1029/2011JB009944.

Turcotte, D.L., and Schubert, G., 2002, Geodynamics (2d ed.): Cambridge, United Kingdom, Cambridge University Press, 848 p.

U.S. Geological Survey–Arabian American Oil Company, 1963, Geologic Map of the Arabian Peninsula: U.S. Geological Survey Miscellaneous Geological Investigations Map I–270 A., 1:2,000,000 scale, https://doi.org/10.3133/i270A.

Washington, H.S., 1917, Chemical analyses of igneous rocks published from 1884 to 1913, inclusive, with a critical discussion of the character and use of analyses: U.S. Geological Survey Professional Paper 99, 1,201 p.

Watson, E.B., and Green, T.H., 1981, Apatite/liquid partition coefficients for the rare earth elements and strontium: Earth and Planetary Science Letters, v. 56, p. 405–421.

White, R.W., Powell, R., and Clarke, G.L., 2002. The interpretation of reaction textures in Fe-rich metapelitic granulites of the Musgrave Block central Australia—Constraints from mineral equilibria calculations in the system K_2O–FeO–MgO–Al_2O_3–SiO_2–H_2O–TiO_2–Fe_2O_3: Journal of Metamorphic Geology, v. 20, p. 41–55.

White, R.W., Powell, R., Holland, T.J.B., Johnson, T.E., and Green, E.C.R., 2014, New mineral activity-composition relations for thermodynamic calculations in metapelitic systems: Journal of Metamorphic Geology, v. 32, p. 261–286.

Wilshire, H.G., Meyer, C.E., Nakata, J.K., Calk, L.C., Shervais, J.W., Nielson, J.E., and Schwarzman, E.C., 1988, Mafic and ultramafic xenoliths from volcanic rocks of the western United States: U.S. Geological Survey Professional Paper 1443, 179 p.

Workman, R.K., Hart, and S.R., 2005, Major and trace element composition of the depleted MORB mantle (DMM): Earth and Planetary Science Letters, v. 231, p. 53–72.

Yao, Z., Mooney, W.D., Zahran, H.M., and Youssef, S.E.-H., 2017, Upper mantle velocity structure beneath the Arabian shield from Rayleigh surface wave tomography: Journal of Geophysical Research, v. 122, p. 6552–6568.

Yoder, H.S., and Tilley, C.E., 1962, Origin of basaltic magmas—An experimental study of natural and synthetic rock systems: Journal of Petrology, v. 3, p. 342–532.

York, D., 1969, Least-squares fitting of a straight line with correlated errors: Earth and Planetary Science Letters, v. 5, p. 320–324.

Moffett Field Publishing Service Center, California
Manuscript approved April 29, 2021
Edited by Taryn A. Lindquist
Layout and design by Kimber Petersen
Illustration support by JoJo Mangano

Sisson and others—**Mantle Origin and Crustal Differentiation, Basalts and Hawaiites, Northern Harrat Rahat**—Professional Paper 1862–I

ISSN 1044-9612 (print)
ISSN 2330-7102 (online)
https://doi.org/10.3133/pp1862I